ULB

Université Libre de Bruxelles

Faculty of Applied Sciences

Finite Element Modelling of Piezoelectric Active Structures

Vincent Piefort

Thesis submitted in candidature for the degree of Doctor in Applied Sciences

Academic Year 2000-2001

Active Structures Laboratory
Department of Mechanical Engineering and Robotics

To my son *Makhno*

Acknowledgements

I would like first to express my gratitude to my supervisor Prof. André Preumont, head of the *Active Structures Laboratory* for revealing me as a researcher ten years ago and for his guidance and encouragements throughout this work.

I would also like to thank Philippe Jetteur from *Samtech s.a.* without the kind assistance of whom the achievements of this work would not have been possible.

My gratitude also goes to my colleagues for their moral support and specially to Nicolas, who was the first member of the team to be faced to piezoelectric shells modelling during the *CFIE* project, and to Arnaud and Pierre who brought to my attention some other problems in vibroacoustics control systems modelling.

Many thanks also to Kris Henrioulle (KUL-PMA) for submitting to my attention the *ASAC* panel modelling problem.

I am also most grateful to my parents, to Valérie and to all my friends for helping me not to be too much of an engineer.

This thesis finalizes a five year research in the *Active Structures Laboratory* of *Université Libre de Bruxelles*. This work was funded by *Région Wallonne - Division Générale des Techniques, de la Recherche et de l'Energie* (Conventions 95/2792 and 97/13549). The support of the IUAP-4/24 on *Intelligent Mechatronic Systems* (Belgian programme on InterUniversity Attraction Poles initiated by the Belgian State, Prime Minister's Office, Science Policy Programming) is also acknowledged.

Foreword: motivation of this work

In 1993, at the request of *ESA*, *ULB* developed a laboratory demonstration model of a very flexible active plate (35 cm×60 cm) controlled by *PZT* piezoceramics; it was later transformed into a flight model (to be flown in a canister) by our industrial partner in this project *Spacebel Instrumentation* and the experiment (named *CFIE*: Control-Flexibility Interaction Experiment), was successfully flown by *NASA* in the space shuttle *ENDEAVOUR* in September 1995 (Loix, 1998). According to the specifications, the experiment had to fit into a *GAS* (Get Away Special)

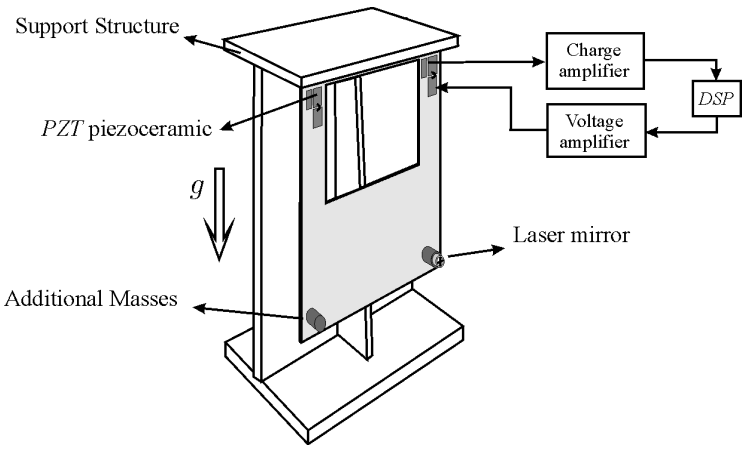

Figure 1: Laboratory demonstration model of the *CFIE* experiment.

canister (cylinder of 50 cm diameter and 80 cm high), demonstrate significant gravity effects, and use the piezoelectric technology. We settled on a very flexible steel plate of 0.5 mm thickness hanging from a support as shown on Fig.1; two additional masses were mounted, as indicated in the figure, to lower the natural frequencies of the system. The first mode was in bending and the second one was in torsion. Because of the additional masses, the structure had a significant geometric stiffness due to the gravity loads (responsible for a rise of the first natural frequency from 0.5 Hz in zero gravity to 0.9 Hz with gravity). The finite element model of the structure in the gravity field could be updated to match the experimental results on the ground, but the in-orbit natural frequencies could only be predicted numerically and were therefore subject to uncertainties. At the time, the model used by Loix (1998) was based on the simplified approach using the equivalent piezoelectric loads. The *CFIE* experiment motivated the research work on the finite element modelling of piezoelectric shells and, as a consequence, initiated the present thesis.

The need for an accurate modelling of local effects in nearly colocated control systems can be illustrated by the experiment of Fig.2 (Loix & Preumont, 1995). In this experiment, a cantilever beam is fitted with four piezoelectric patches, indicated as p_1 to p_4 on the figure. p_1 is taken as actuator and the frequency response functions are compared when the sensor is taken successively as p_2, p_3 and p_4. Although the three situations are equivalent if a beam model is considered in conjunction with equivalent piezoelectric loads, we observe substantial differences in the location of the zeros which in turn, produces substantial differences in the performance of the closed-loop control system. The objective of this work was to develop a general tool able to predict accurately these situations.

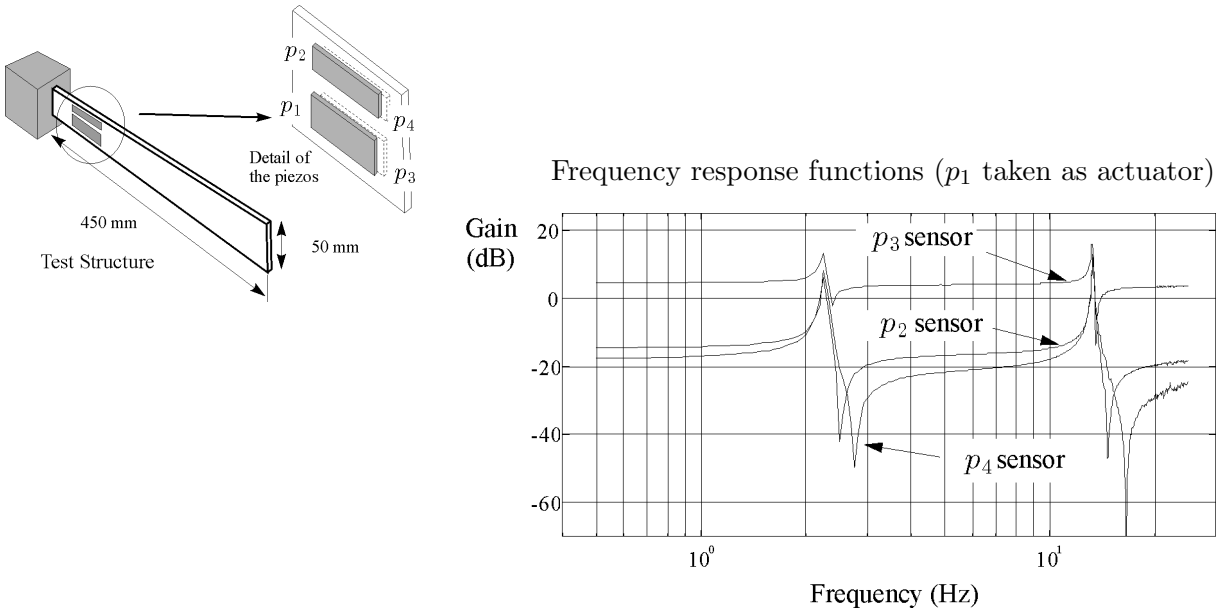

Figure 2: Cantilever plate with nearly colocated actuator/sensor piezoceramics: experiment

In order to resolve the technological issues related to the practical realisation of a nearly colocated actuator/sensor system using bonded piezoceramics, a simple cantilever plate was used (Loix, 1998). Important differences in the experimental frequency response functions for similar actuator/sensor positions appeared (Fig.2) that can not be explained by a classical beam model. More specifically, the experiment of Fig.2 pointed out the importance of local membrane effects that can only be predicted by a rigorous shell finite elements model; tis was the third motivation of this research work.

Summary

This thesis is organized in five chapters.

Chapter 1 (Introduction) is an introduction to piezoelectric materials. It contains an historical overview of piezoelectricity, some general considerations for a better understanding of piezoelectric materials, and a brief overview of other *smart* materials.

Chapter 2 (Constitutive Equations) is dedicated to the constitutive equations of piezoelectricity. It contains a unidimensional presentation of piezoelectric constitutive equations using a electromagnetic approach. The general thermopiezoelectric constitutive equations are established starting from thermodynamics principles, and simplified for a *Kirchhoff* laminate embedding piezoelectric layers.

Chapter 3 (Actuation and Sensing) introduces the various designs used in piezoelectric actuation and sensing devices. It contains a review of the different piezoelectric modes of actuation/sensing. Simplified *laminar design* modelling approaches are presented and their limitations stressed. Some examples of electrode shaping to achieve targeted control devices are analyzed.

Chapter 4 (Finite Element Approach) presents an electromechanically coupled finite element formulation. It contains a review of finite element modelling of piezoelectric structures and a general electromechanically coupled finite element formulation starting from the constitutive equations and the *Hamilton* variational principle. A *Kirchhoff* piezoelectric multilayered element formulation is developed and its extension to a *Mindlin* formulation is described. Its actual implementation into the commercial finite element package *Samcef* (*Samtech s.a.*) is presented together with the volume elements implementation. Some particular electrical boundary conditions are illustrated, and a method to extract a state space model of a piezoelectric input/output system from the modal finite element analysis is presented.

Chapter 5 (Applications) contains the description of some applications of the developed tools: actuation, sensing, vibroacoustics, control. The importance of the in-plane components in the open-loop frequency response functions of nearly colocated control systems is illustrated.

Contents

List of Figures

List of Tables

List of Symbols

$[\,]$	matrix
$[\,]^T$	matrix transposed
$\{\,\}$	vector
$\{\,\}^T$	vector transposed
$\dot{\psi}, \ddot{\psi}$	first and second time derivatives of ψ
ψ', ψ''	first and second spatial derivatives of ψ
∇	gradient operator
∂_x	spatial derivation operator
$\partial\psi/\partial x$	spatial derivative of ψ with respect to x
$\psi_{,x}$	short notation for the spatial derivative of ψ with respect to x
α	specific heat
α_i	weights of the adaptive linear combiner
β	dielectric constant (ε^{-1}) (IEEE std)
$\{\beta\}$	fibre rotation angles
δ_{ij}	*Kronecker* index
δ	variation operator
Δ	variation (of length), distance, stroke

γ	shear strain (standard engineering notation)
ε	permittivity (IEEE std)
ε_0	permittivity of vacuum ($\simeq 8.854\ 10^{-12}$ F/m)
ε_r	relative permittivity ($\varepsilon/\varepsilon_0$)
ϵ	strain (standard engineering notation)
ϕ, Φ	voltage, electrical potential
$\{\phi_i\}$	nodal voltages, electrical potentials
Ψ	Power Spectral Density
κ	curvature
λ	thermal expansion coefficient
μ_k	modal mass of mode k
ν	*Poisson* ratio
ω_k	natural frequency of mode k
ω	frequency
$[\Omega]$	eigen frequencies matrix
Ω	surface, area
θ_k	orientation angle between material axes of layer k and the global axes
Θ, Θ_0	temperature, reference temperature
θ	small temperature change
ρ	mass density
ϱ	surfacic charge density
σ	stress (standard engineering notation)
ς	entropy

τ	shear stress (standard engineering notation)
ξ_k	modal classical damping ratio of mode k
χ	piezoelectric anisotropy ratio
$\mathbf{a}$	arbitrary vector
a, b	lengths, distances, dimensions
$[A]$	extension stiffness matrix
A_s	*austenite start* temperature (shape memory effect)
A_f	*austenite finish* temperature (shape memory effect)
$[B]$	extension/bending coupling stiffness matrix
$[\mathcal{B}]$	shape functions derivatives
c	mechanical stiffness (IEEE std)
C_0, C	= electrical capacitances
C^{st}	constant term
$[C]$	structural damping matrix
$\mathcal{C}$	contour
d	piezoelectric coupling (electrical field / strain) (IEEE std)
d^*	electrostrictive coupling (electrical field / stress)
$[D]$	bending stiffness matrix
D	electric displacement field (IEEE std)
$[\mathcal{D}]$	derivation operator
$[D_{HF}]$	residual mode: static contribution of the unmodelled high frequency modes to the frequency response function
e	piezoelectric coupling (electrical field / stress) (IEEE std)

e^*	electrostrictive coupling (electrical field / stress)
E	electrical field (IEEE std)
$\{\mathcal{E}\}_k$	membrane, bending piezoelectric coupling written in global axes
$\{f_i\}$	element nodal (mechanical) applied resultant forces
$\{F\}$	assembled nodal (mechanical) applied resultant forces
F_P	point force
F_V	body force
F_Ω	surface force
F_0	uniform load
g	piezoelectric coupling (electrical displacement / strain) (IEEE std)
$\{g_i\}$	element nodal (electrical) applied resultant charges
g_i	*Gauss* weights
$\{G\}$	assembled nodal (electrical) applied resultant charges
G	thermoelectric *Gibbs* state function
G, G_{12}	shear modulus
$[\mathcal{G}(\omega)]$	frequency response function
H	electrical enthalpy density
$\mathcal{H}$	magnetic field
$[K]$	transverse shear stiffness matrix
h, h_k	thickness, thickness of layer k
h	piezoelectric coupling (electrical displacement / stress) (IEEE std)
I	electrical current
I_n	identity matrix of order n

J	kinetic energy
k_1, k_2	ideal spring stiffness
$[K_{uu}]$	element mechanical stiffness matrix
$[K_{u\phi}] = [K_{\phi u}]^T$	element piezoelectric coupling matrix
$[K_{\phi\phi}]$	element capacitance matrix
$[K_{UU}]$	assembled mechanical stiffness matrix
$[K_{U\Phi}] = [K_{\Phi U}]^T$	assembled piezoelectric coupling matrix
$[K_{\Phi\Phi}]$	assembled capacitance matrix
$[K_{elt}]$	complemented element stiffness matrix
L	length
$[L]$	localisation matrix
$\mathcal{L}$	Lagrangian
m	lineic mass
M_s	*martensite start* temperature (shape memory effect)
M_f	*martensite finish* temperature (shape memory effect)
M	resultant bending effort
$[\mathcal{M}]$	element mass matrix, assembled mass matrix
$\mathbf{n}$	vector normal to a contour
N	resultant membrane effort
$[\mathcal{N}]$	interpolation (shape) functions
p	pyroelectric coefficient
P_0, P	free polarization, polarization
q	elementary electrical charge

Q	total electrical charge
$\left[\overline{Q}\right]_k$	stiffness matrix of layer k written in the global axes
R	electrical resistance
$[R_T]$	rotation matrix relating the stress written in the orthotropy axes of the piezo to the stress written in the global axes
$[R_S]$	rotation matrix relating the strain written in the orthotropy axes of the piezo to the strain written in the global axes
s	mechanical compliance (IEEE std)
S	strain (IEEE std)
T	stress (IEEE std)
$\mathcal{T}$	resultant transverse shear effort
$\mathbf{u^0}$	mid-plane membrane displacement vector
u, v, w	displacements relatives to x, y, z respectively
$\{u\}$	displacement field vector
$\{u_i\},\ \{U\}$	nodal displacements
U	stored energy density
V	volume
V_{vol}	volume velocity
$\mathcal{W}$	virtual work of external electrical and mechanical forces
x, y, z	spatial coordinates
x_k	modal amplitude of mode k
$\{\mathcal{X}\}_k$	transverse shear piezoelectric coupling written in global axes
Y	*Young*'s modulus
z_k	coordinate of layer k relative to the mid-plane

Z	impedance
$\mathcal{Z}_k$	modal shape of mode k

Chapter 1

Introduction

This chapter is divided is three parts. In a first section, a short history of piezoelectricity is presented. The second section presents the piezoelectric, pyroelectric and ferroelectric materials. The third section is a brief overview of different types of smart materials.

1.1 History of piezoelectricity

Centuries ago, natives from Ceylan and India already noticed a peculiar property of tourmaline crystals. Thrown in hot ashes, these crystals first attract them to reject them a few moments afterwards. This experiment came into Europe with the import of tourmaline by dutch tradesmen at the beginning of the $XVIII^{th}$ century. The tourmaline was called the *Ceylan magnet*.

In 1756, the electrical origin of that behaviour was demonstrated by the german physicist Aepinus (electrical capacitance inventor)[1]. That behaviour was named *pyroelectricity* by the scottish physicist D.Brewster in 1824. The pyroelectric effect can be defined as the induction of polarization by thermal energy absorption; the induced polarization is proportional to the resulting temperature variation. The inverse property, of much less amplitude, is called the electrocaloric effect.

The piezoelectric effect was first mentioned in 1817 by the french mineralogist René Just Haüy[2]. It was first demonstrated by Pierre and Jacques Curie in 1880. Their experiments led them to elaborate the early theory of piezoelectricity. This theory was complemented by the further work of G.Lippman[3], W.G.Hankel[4], Lord Kelvin and W.Voigt (beginning of *XXth* century).

Until the beginning of the century, the piezoelectricity did not leave the laboratories. The first applications appeared during the first world war with the *sonar* in which piezoelectric quartz are used to produce ultrasonic waves (P.Langevin) and as sensors. In the twenties, the use of quartz to control the resonance frequency of oscillators was proposed by an american physicist: W. G. Cady. It is during the period following the first world war that most of the piezoelectric

[1] First observation of the electrical polarization of the *tourmaline* crystal when its temperature changes
[2] First observation of the presence of electric charges on the surface of a stressed *tourmaline* crystal
[3] Mathematical deduction of the inverse piezoelectric effect, confirmed experimentally by P. & J. Curie: 1881
[4] W.G.Hankel introduced the term *piezoelectricity*

applications we are now familiar with (microphones, accelerometers, ultrasonic transducers, benders, ...) were conceived. However, the materials available at the time often limited device performance. The development of electronics, specially during the second world war, and the discovery of ferroelectric ceramics increased the use of piezoelectric materials.

The *direct* piezoelectric effect consists of the ability of certain crystalline materials (i.e. ceramics) to generate an electrical charge in proportion of an externally applied force. The direct piezoelectric effect has been widely used in transducers design (accelerometers, force and pressure transducers, ...). According to the *inverse* piezoelectric effect, an electric field induces a deformation of the piezoelectric material. The inverse piezoelectric effect has been applied in actuators design.

The use of piezoelectric materials as actuators and sensors for noise and vibration control has been demonstrated extensively over the past few years (e.g. Forward, 1981; Crawley & de Luis, 1987). There are two classes of piezoelectric materials used in vibration control: ceramics and polymers. The best known piezoceramic is the Lead Zirconate Titanate (PZT); it has a recoverable strain of 0.1% and is widely used as actuator and sensor for a wide range of frequencies, including ultrasonic applications; it is well suited for high precision as well. Piezopolymers are mainly used as sensors; the best known is the Polyvinylidene Fluoride ($PVDF$). The $PVDF$ were first studied by Kawai (end of the 60's) and were made commercially available in the early 80's.

1.2 Piezoelectric materials

The piezoelectric effects can be seen as transfers between electrical and mechanical energy. Such transfers can only occur if the material is composed of charged particles and can be polarized. For a material to exhibit an anisotropic property such as piezoelectricity, its crystal structure must have no centre of symmetry (See e.g. van Randeraat & Setterington, 1974). 21 crystal structures out of 32 are non-centrosymmetric. A crystal having no center of symmetry possesses one or more crystallographically unique directional axes. All 21 non-centrosymmetric crystal classes, except 1, show piezoelectric effect along the directional axes. Out of the 20 piezoelectric classes, 10 have only one unique direction axis. Such crystals are called polar crystals as they show spontaneous polarization. The value of the spontaneous polarization depends on the temperature. This is called the pyroelectric effect. The pyroelectric crystals for which the magnitude and direction of the spontaneous polarization can be reversed by an external electric field are said to show ferroelectric behavior.

Most of the piezoelectric materials are crystalline solids. They can be single crystals, either formed naturally or by synthetic processes, or polycrystalline materials like ferroelectric ceramics which can be rendered piezoelectric and given, on a macroscopic scale, a single crystal symmetry by the process of poling (by subjecting to a high electric field not far below the Curie temperature - see §1.2.3). The piezoelectric effect can also appear in crystals composed of only one type of element (in this case, the polarization is due to a distortion in the electronic distribution). Certain polymers can also be made piezoelectric by stretching under an electrical field.

The origins of electric polarization are first presented. The molecular nature of piezoelectricity and the main coupling coefficients are introduced next using a simple example: the bi-ionic monocrystal $Cd\ S$ (Brissaud, 1986). The more complex mechanisms involved in ferroelectric

ceramics are described last.

1.2.1 Origins of electric polarization

A material that can be polarized under an electrical field is called a dielectric. Three origins for the macroscopic polarization of a dielectric material can be distinguished (Fig.1.1).

- **electronic polarization:** When an electric field is applied, the electronic clouds deform creating a macroscopic dipole.
- **ionic polarization:** When an electrical field is applied, anions are attracted by the anode and cations by the cathode, creating dipoles
- **dipole reorientation:** A macroscopically non polarized material can be composed of many polarized domains. An applied electric field will cause the domains to reorient, inducing a global polarization

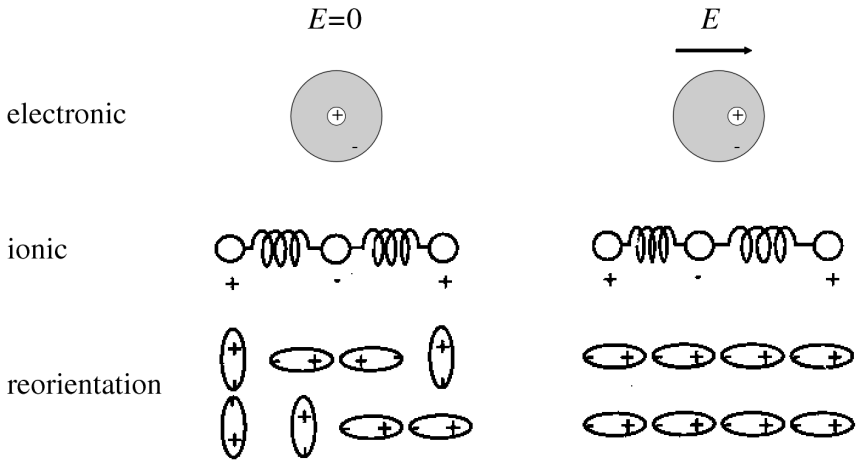

Figure 1.1: Origins of polarization

1.2.2 Bi-ionic crystal

An intuitive explanation of the piezoelectricity can be given by a simple unidimensional example. Let us consider a simple bi-ionic crystal.

The $Cd\ S$ crystal structure can be seen as an array of identical rows composed of sub-structures such as described in Fig.1.2 where cations Cd (charge $+q$) and anions S (charge $-q$) alternate. The interatomic cohesion forces are modelled by ideal springs of different stiffness k_1 and k_2, the distance between consecutive pairs of atoms being different.

If the crystal is composed of n basic elements of length a, as shown on Fig.1.2, including 2 electrical dipoles $\frac{q}{2}(a-b)$ and $-\frac{q}{2}b$, the global free polarization will be given by

$$P_0 = n\frac{q}{2}(a-2b) \tag{1.1}$$

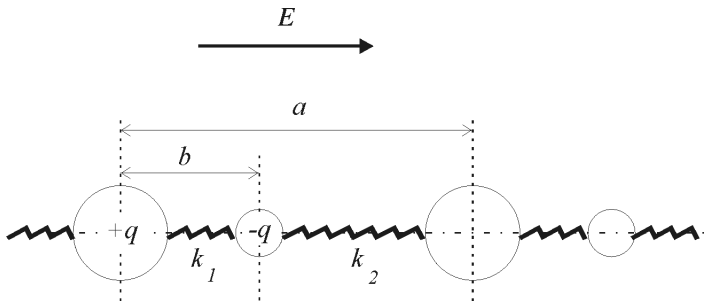

Figure 1.2: Structure of the $Cd\ S$ crystal

For a constrained crystal (along the axis of alignement), the interatomic distances change and a polarization P is induced; *this is the direct piezoelectric effect*:

$$P = \Delta P_0 = n\frac{q}{2}(\Delta a - 2\Delta b) \tag{1.2}$$

Conversely, when an electric field E is applied along the same axis, the ions move and a global deformation is induced; *this is the inverse piezoelectric effect*. The static equilibrium relation for each ion can be written:

$$qE + k_1\Delta b - k_2\Delta(a - b) = 0 \tag{1.3}$$

The induced polarization is related to the electrical field and to the atomic displacement by:

$$P = n\frac{q}{2}\left(\frac{2q}{k_1 + k_2}E + \frac{k_1 - k_2}{k_1 + k_2}\Delta a\right) \tag{1.4}$$

which can be written

$$P = \chi_{ion}E + eS \tag{1.5}$$

where

$$\chi_{ion} = n\frac{q}{2}\frac{2q}{k_1 + k_2} \tag{1.6}$$

is called the ionic polarizability of the crystal,

$$S = \frac{\Delta a}{a} \tag{1.7}$$

is the strain, and

$$e = na\frac{q}{2}\frac{k_1 - k_2}{k_1 + k_2} \tag{1.8}$$

is the piezoelectric constant.

The electric displacement (induced polarization) can be written

$$\boxed{D = eS + \varepsilon^S E} \tag{1.9}$$

where the permittivity at constant strain ε^S is given by

$$\varepsilon^S = \varepsilon_0 + \chi_{ion} \tag{1.10}$$

with ε_0 is the permittivity of the vacuum

The stress induced in a unitary section perpendicular to the considered axis, assuming a total of N rows on a unitary section and assuming an equal number of springs of each type k_1 and k_2 in such a section, is given by:

$$T = \frac{N}{2} k_1 \Delta b + k_2 \frac{N}{2} \Delta (a - b) \tag{1.11}$$

Considering that we have $N = na$ and using Equ.(1.3) and (1.7), one gets:

$$T = na^2 k_2 \frac{k_1 k_2}{k_1 + k_2} S - na \frac{q}{2} \frac{k_1 - k_2}{k_1 + k_2} E \tag{1.12}$$

which can be written

$$\boxed{T = c^E S - eE} \tag{1.13}$$

where

$$c^E = na^2 k_2 \frac{k_1 k_2}{k_1 + k_2} \tag{1.14}$$

is the mechanical stiffness at a constant electric field, and e is the piezoelectric constant given by Equ.(1.8). It is worth noticing that c^E is related to the stiffness of the two springs k_1 and k_2 in series and that the piezoelectric constant e is zero if the springs are of equal stiffness. Equations (1.9) and (1.13) are the piezoelectric constitutive equations.

However, ions are never connected by ideal springs. In most cases, these springs are anharmonic ($F \cong k\Delta + k'\Delta^2$). A fraction of the stress induced is independent of the direction of the applied field.

$$T = c^E S - eE - e^* E^2 \tag{1.15}$$

This effect is called the *electrostrictive* effect, e^* is the electrostrictive coefficient. (See §1.3.2)

1.2.3 Ferroelectric ceramics

Domains reorientation - hysteresis

To gain an understanding of the piezoelectric effect in ferroelectric materials (See e.g. van Randeraat & Setterington, 1974; Uchino, 2000), we must first consider the behaviour of the material on a microscopic scale. Above a certain temperature, called the Curie temperature (θ_c), the crystal structure of a ferroelectric material does have a centre of symmetry and has therefore no electric dipole moment. Below this temperature, it undergoes a phase change to a more

complex structure which is non-centrosymmetric. In this phase, the crystal presents a natural electric dipole (*pyroelectricity*) which may be reversed (*ferroelectricity*) and also switched in certain allowed directions by the application of a sufficiently high electric field.

Ferroelectric crystals possess regions with uniform polarization called ferroelectric domains. Within a domain, all the electric dipoles are aligned in the same direction. There may be many domains in a crystal separated by interfaces called domain walls. A ferroelectric single crystal, when grown, has multiple ferroelectric domains in each of which the electric dipole is aligned in a specific allowed direction. As each of the allowed direction has the same probability to appear, the net electric dipole summed over the whole crystal is zero.

Nevertheless, when the crystal is cooled down in the presence of an electric field, the domains tend to align in the allowed direction nearest to the electric field. The crystal as a whole presents an electric dipole.

If this crystal is subjected to stress, the lattice will be distorted and the stress will also cause some domains to grow at the expense of others. This results in a change in the total dipole moment of the crystal. Within a certain range of stress, this variation of dipole moment with the stress is approximately linear and reversible.

Ferroelectric components may be made piezoelectric in any chosen polar direction by the poling treatment which involves exposing the material to a high electric field at a temperature not far below the Curie point.

Because of the random orientation of the domains and the fact that only certain dipole directions are allowed within the crystal, it is not possible to get the perfect dipole alignment with the field. However, there are several allowed directions within every domain and so a reasonable degree of alignment with the field is possible. After cooling of the product and removal of the poling field, the dipoles cannot easily return to their original positions, and we have now what is known as

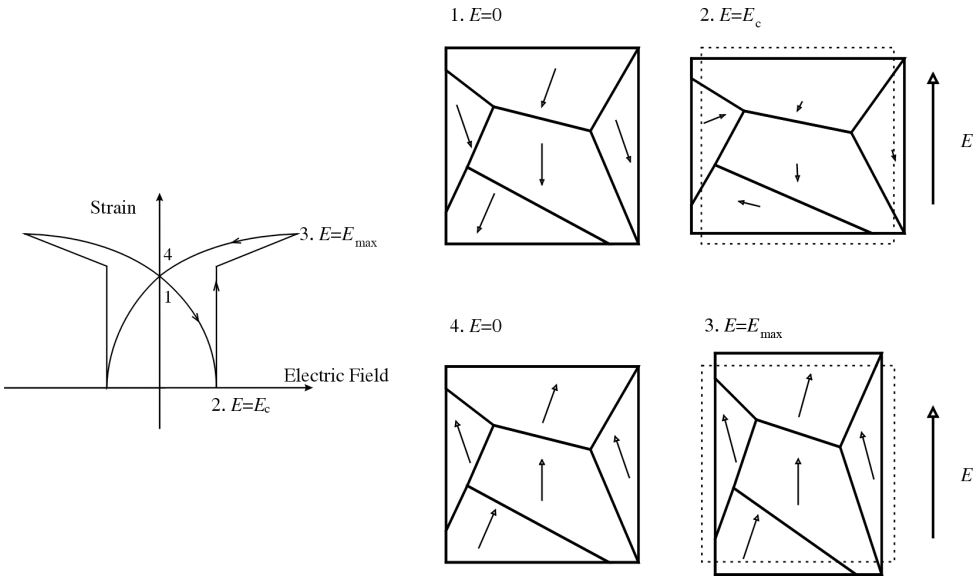

Figure 1.3: Strain change associated with the polarization reorientation

remanent polarization of the material. The body has become permanently piezoelectric and can convert mechanical energy into electrical energy, and vice versa.

Fig.1.3 shows schematically the domain reorientation in a multidomain ferroelectric piezoceramic. The material is initially poled along the negative direction (1) and an electric field is applied along the positive direction. The crystal will first shrink with the increase of the field as the field is opposite in direction to the polarization. The strain reaches a minimum at a certain field (*coercive field* E_c), where the polarization starts to reverse in each grain (2). Above E_c, the crystal expands until E_{max} (3) as the field has now the same direction as the polarization. Near E_{max}, all the reversible polarization have been reversed. As the field is reduced, the strain decreases monotonically as no polarization reversal occurs. The situation for a zero electric field (4) is similar to the starting situation except that the polarization is reversed; the material is now poled along the positive direction.

Fig.1.4 shows a typical electric field / strain curves (directions x_3 and x_1, parallel and perpendicular to the field) for a PZT based ferroelectric piezoceramic. In a cycle with a small maximum electric field, the field-induced strain curve is almost linear (a). The curve becomes distorted as the electrical field increases and shows a larger hysteresis (b, c, d) and finally transforms into a symmetric butterfly shape when the electric field exceeds the *coercive field*; this is caused by the polarization due to dipole reorientation.

Many piezoelectric (including ferroelectric) ceramics such as Barium Titanate ($Ba\,Ti\,O_3$), Lead Titanate ($Pb\,Ti\,O_3$), Lead Zirconate Titanate (PZT) and Lead Lanthanum Zirconate Titanate

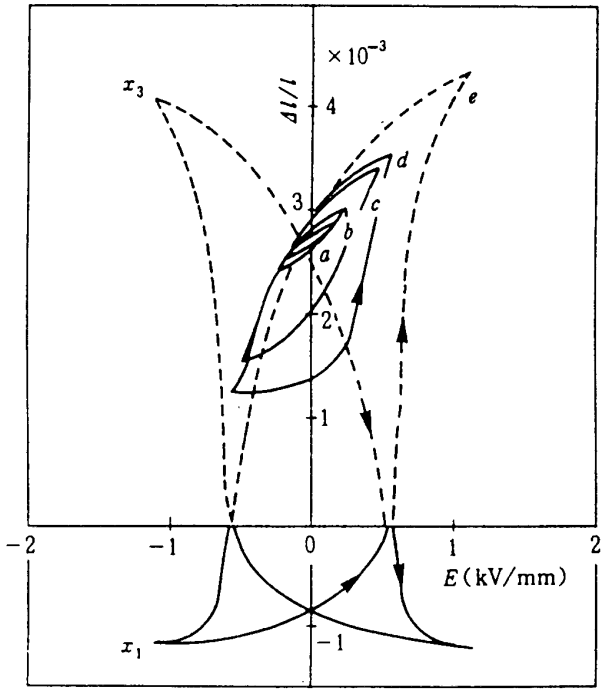

Figure 1.4: PZT: electric field / strains

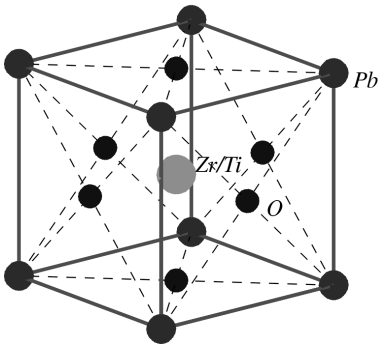

Figure 1.5: Perovskite structure in *PZT*

(*PLZT*) have a *perovskite* type structure (Fig.1.5). Perovskite is the family name of a group of materials having the same structure as the calcium titanate ($Ca\ Ti\ O_3$)[5].

Doping effect in *PZT*

The Lead Zirconate Titanate (*PZT*) is a binary solid solution of $Pb\ Zr\ O_3$ and $Pb\ Ti\ O_3$. The *PZT* ($Pb(Zr_y\ Ti_{1-y})O_3$) is composed of a lattice of basic cells having the *perovskite* structure (Fig.1.5). The electrical properties of ferroelectric ceramics can be modified by substituting ions of different valence in the lattice.

By doping the crystal with impurities (replacing some Zr^{4+} or Ti^{4+} ions), a local deficiency is introduced (Fig.1.6).

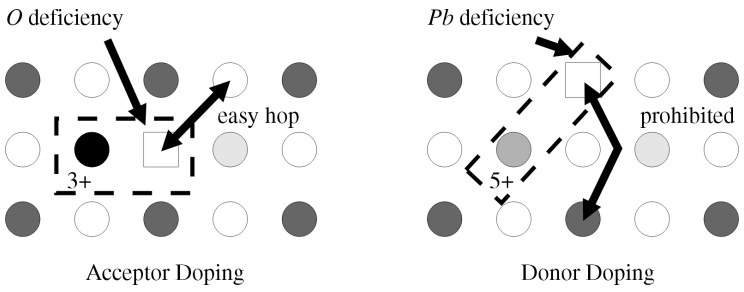

Figure 1.6: Effect of doping

Acceptor ions (i.e. Fe^{3+}) introduce oxygen deficiencies ($\circ$).

$$Pb(Zr_y\ Ti_{1-y-x}\ Fe_x)(O_{3-x/2}\ \circ_{x/2})$$

Acceptor doping induces a higher mobility of the oxygen ions; They can easily jump to fill in the adjacent deficiency. This implies an easy reorientation of the deficiency related dipoles. The hysteresis becomes more important while the strain/electric field ratio is lowered. Such a piezoeceramics is called *hard* piezoceramic. Hard *PZT*'s usually have lower permittivities,

[5] *Perovskite* is the mineral name of calcium titanate

smaller electrical losses and lower piezoelectric coefficients. These are more difficult to pole and depole, thus making them ideal for rugged applications such as ultrasonic motors.

Donor ions (i.e. Nb^{5+}) introduce Pb deficiencies ($\bullet$).

$$(Pb_{1-x/2}\ \bullet_{x/2})(Zr_y\ Ti_{1-y-x}\ Nb_x)O_3$$

Pb ions cannot easily hop to the nearest deficiencies due to the oxygen surroundings. Dipoles cannot easily reorient; The hysteresis is lowered and the strain/electric field ratio is increased. We obtain a so called *soft* piezoceramic. The soft PZT's have a higher permittivity, larger losses, higher piezoelectric coefficient and are easy to pole and depole. They can be used for applications requiring very high piezoelectric properties such as actuation and sensing applications.

$PLZT$ is a transparent ferroelectric ceramic formed by replacing Pb^{2+} ions by La^{3+} ions in PZT. The transparent nature of $PLZT$ has led to its use in electro-optic applications.

1.2.4 Polymers

Piezoelectricity can be obtained by orientating the molecular dipoles of polar polymers such as Polyvinylidene Fluoride ($PVDF$ or PVF_2) in the same direction. The $PVDF$ can be made piezoelectric because fluorine is much more electronegative than carbon. The fluorine atoms will attract electrons from the carbon atoms to which they are attached. The $-CF_2-$ groups in the chain will be very polar so when they are placed in an electrical field, they will align. Conversely, when the piezopolymer deforms, a macroscopic dipole appears.

This can be obtained by submitting the film of polymer to a sufficiently high electric field after a mechanical stretching. The obtained polarization is mainly due to the spatial rearrangement of polar segments of the macromolecular chains.

By machining the material in one or two perpendicular directions prior to the polarization process, different piezoelectric behaviours can be obtained (Fig.1.7). A uni-axial stretching will induce nearly unidirectional piezoelectric properties. A bi-axial stretching will induce piezoelectric properties that are isotropic in the plane.

Table 1.1 presents typical $PVDF$ characteristics (Piezotech Documentation, 1997) compared to PZT ones.

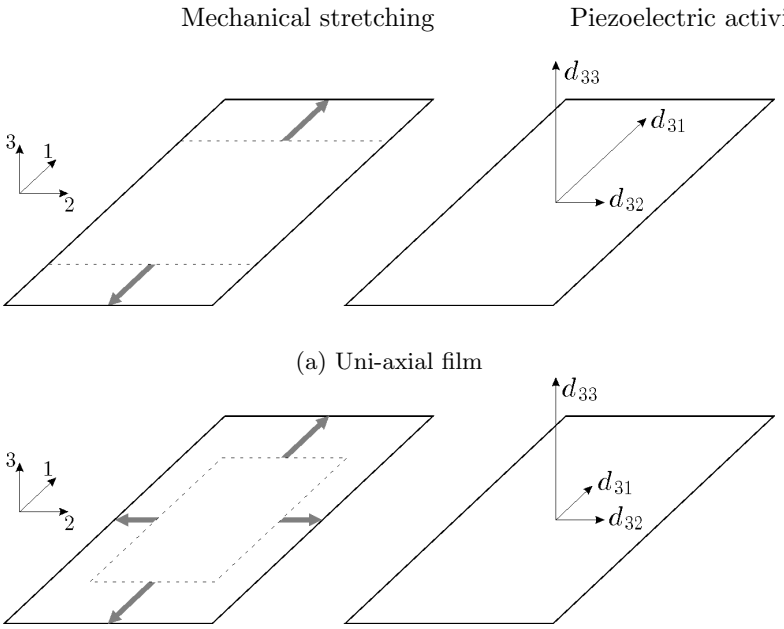

(a) Uni-axial film

(b) Bi-axial film

Figure 1.7: Unidirectional and bidirectional *PVDF*

Material properties	*PZT*	*PVDF*	
		uni-axial	bi-axial
Piezoelectric constants			
d_{33} (10^{-12} Cb/N or m/V)	300	-25	-25
d_{31} (10^{-12} Cb/N or m/V)	-150	15	3
d_{32} (10^{-12} Cb/N or m/V)	-150	3	3
Relative permittivity $\varepsilon/\varepsilon_0$	1800	12	12
($\varepsilon_0 = 8.854\ 10^{-12}$ F/m)			
Young's modulus (GPa)			
Y_1	50	3	3
Y_2	50	1	3
Y_3	50	10	10
Maximum stress in traction (MPa)			
direction 1	80	200	200
direction 2	80	40	200
Max. operating Temp. ($^\circ$C)	140	90	90
Max. Electric field (V/m)	$1\,10^6$	$500\,10^6$	$500\,10^6$
Density (kg/m^3)	7600	1800	1800

Table 1.1: *PZT* and *PVDF* typical properties

1.3 Other Smart materials

The best known among the *smart materials* are certainly the piezoelectric materials and more precisely the piezoceramics. However, several others are available. Table 1.2 summarizes the different effects and couplings existing in materials considering the different conjugated physical fields classically involved.

What characterize a *smart* or *active* material ? Couplings that are *off-diagonal* in Table 1.2 are typically responsible for the so called *smart* behaviour of materials. A material can be said *smart* if one of its *smart* coupling is (or can be made) sufficiently important to be used in *active* devices. The few next paragraphs presents two types of *smart* materials (shape memory alloys and magneto/electro-strictive materials) and a *semi-smart* one (magneto/electro-rheological fluids).

1.3.1 Shape memory alloys

The *Shape Memory Effect* is the effect by which a material, apparently plastically deformed, recovers its original undeformed shape after heating. It initiates in the solid phase change occuring in metals and, more precisely, in the *martensitic transformation*. Two types of alloy exhibit a strong shape memory effect: Copper Alloys (*Cu-Zn-Al* and *Cu-Al-Ni*) and *Nitinols* (*Ni-Ti*). Their main typical characteristics are listed in Table 1.3. The main advantage of *Shape Memory Alloys* is the possibility to achieve complex movements with very few elements, and this, with a small temperature change despite the hysteresis (See e.g. Perkins, 1975; Liang, 1990; Piefort, 1991).

Thermally induced martensitic transformation

Some alloys have interesting properties after quenching. Let us consider an unstressed binary alloy. At high temperature, this alloy exhibit a structure β. After a rapid cooling (*quenching* process), it will keep its structure β in a metastable equilibrium with a structure β'. Let us call, by analogy with iron, β and β', respectively austenitic and martensitic structures.

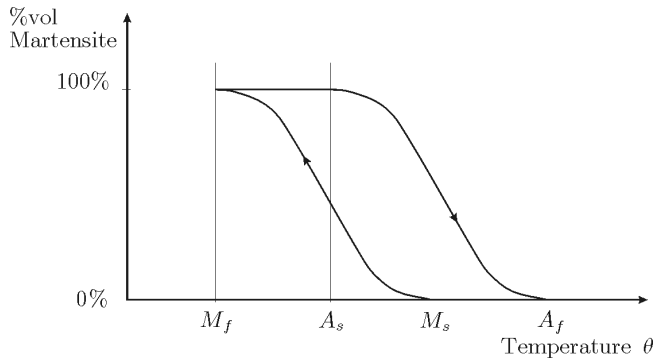

Figure 1.8: The martensitic transformation

The martensitic transformation between austenitic and martensitic structures in shape memory alloys occurs without atomic diffusion, by small successive displacements. This process

Output **Input field**	**Strain**	**Charge** **Current**	**Magnetic field**	**Temperature**	**Light**
Stress	*Elasticity*	Piezo-electricity	Inverse magnetostriction		Photo-elasticity
Electrical field	Inverse Piezo-electricity	*Permittivity* *Conductivity*	Electro-magnetic effect	Electro-caloric effect	Electro-optic effect
Induction	Magneto-striction	Magneto-electric effect	*Permeability*	Magneto-caloric effect	Magneto-optic effect
Heat	Thermal expansion Shape memory	Pyro-electricity		*Specific heat*	
Light	Photo-striction	Photovoltaic effect			*Refractive index*
	Actuation	*Sensing*			

Table 1.2: Some effects in materials (off-diagonal coupling → smart materials)

Properties	Units	Cu-Zn-Al	Cu-Al-Ni	Ni-Ti
Young modulus	GPa	70 to 100	80 to 100	80 to 90
Transformation temperature	$^\circ$C	-200 to 120	-200 to 170	-220 to 110
Hysteresis ($A_s - A_f$)	$^\circ$C	10 to 20	20 to 30	30 to 50
Recoverable strain	%			
Simple SME		5	6	8
Double SME				
for 10^2 cycles		1	1.2	6
for 10^5 cycles		0.8	0.8	4
Pseudo-elastic strain	%	10	10	10

Table 1.3: Shape memory alloys typical properties

induces changes in the elementary crystal shape. Nevertheless, no macroscopic change is observed due to the existence of 24 variants of martensite (only 1 for austenite) so the shape changes compensate inside each *grain* of material. When a sample is cooled down, its crystals transform from β-austenitic structure into β'-martensitic structures without macroscopic deformation; this transformation is characterized by two temperatures: M_s (Martensite Start) at which the transformation begins, and M_f (Martensite Finish) at which all the austenite has been transformed into martensite. When reheated, all the β'-martensitic variants retransform into the same β-austenitic structure; this transformation is characterized by two temperatures: A_s (austenite Start) at which the transformation begins, and A_f (Austenite Finish) at which all the martensite has been transformed back into austenite. The four characteristic temperatures of the martensitic thermal transformation M_s, M_f, A_s, and A_f are represented on Fig.1.8.

Stress induced martensitic transformation

When a shape memory alloy at a temperature above M_s (pure austenite) is submitted to a stress field, the martensitic transformation occurs at higher temperature. This is the stress induced martensitic transformation. The most important characteristic of the stress induced martensite is that the different variants have no longer the same chance to appear. The variants giving the minimum stress state will be favoured: the stress induced martensite is *oriented*.

Associated effects

- **Rubber Effect:** When a shape memory alloy at a temperature below M_f (consisting in different variants of martensite) is submitted to a stress field, the best oriented variants will grow at the expense of the others ($\beta' \longrightarrow \beta'$ transformation). After removing the stress at a temperature below M_f, the stress induced martensite is stable. The material recovers its elastic deformation and a fraction of the martensite reorients, giving an extra strain recovery; this is the *rubber effect* ($1 \rightarrow 2\%$)

- **Memory effect:** After raising the temperature of a plastically deformed *SMA* above A_f, all the martensite transform back into austenite and the material recovers its *warm* shape. If cooled back below M_f, no more shape change is observed as all variants of martensite can

develop equivalently; this is the *simple memory effect* (Fig.1.9).

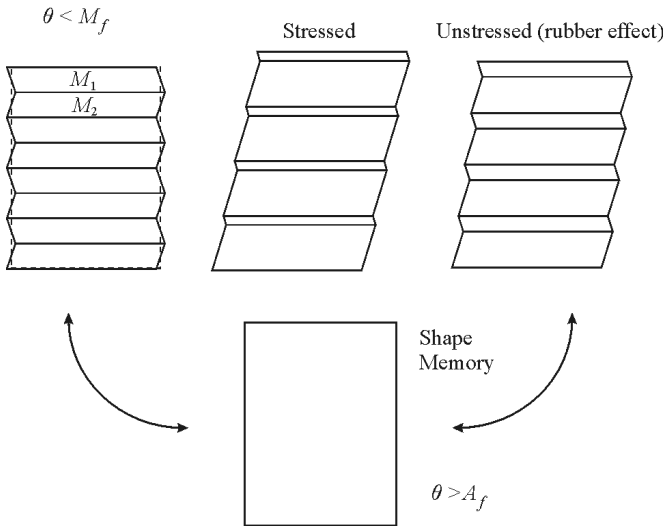

Figure 1.9: Shape memory effect

- **Education:** If, during the cooling phase, the material is forced into a *cold* shape, and the process is repeated a few times, dislocations and internal residual stress state appear, favouring the formation of certain variants of martensite: the material has gained the *double memory effect* and takes spontaneously its *cold* or *warm* shape depending on the temperature: the shape memory alloy is *educated*

- **Pseudoelasticity** The stress induced martensite at a temperature above A_f retransformS into austenite when unstressed, giving the superelastic behaviour to shape memory alloys (Fig.1.10). A number of products have been brought to market that use the pseudoelastic (or superelastic) property. (i.e. Eyeglass frames that use superelastic $Ni\ Ti$ alloy to absorb large deformations without damaging the frames are now marketed).

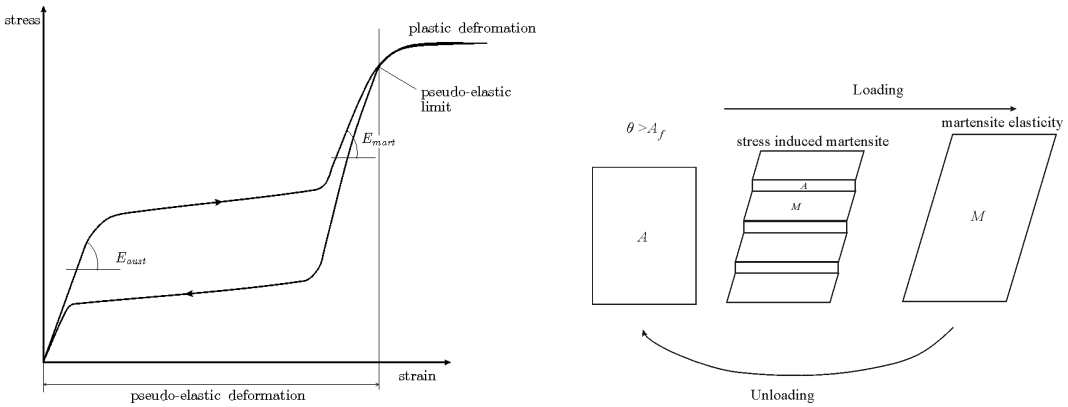

Figure 1.10: Pseudo-elasticity

1.3.2 Electro / magneto-strictive materials

Magnetostriction is the process by which a ferromagnetic material transforms from one shape to another in the presence of a magnetic field[6]. Most ferromagnetic materials exhibit some measurable magnetostriction. Conversely, if an external force produces a strain in a magnetostrictive material, the material's magnetic state will change[7]. This bi-directional magnetomechanical coupling of a magnetostrictive material provides a transduction capability that is used for both actuation and sensing devices.

This solid state phenomenon is a result of the rotation of small magnetic domains causing internal strains in the material inducing an expansion in the field direction. As the field is increased, more domains tend to align with the magnetic field until magnetic saturation is achieved. If the field is reversed, the direction of the domains is also reversed but the strains still result in an expansion. Since the magnetostriction has a molecular origin, the response is very fast (a few μs).

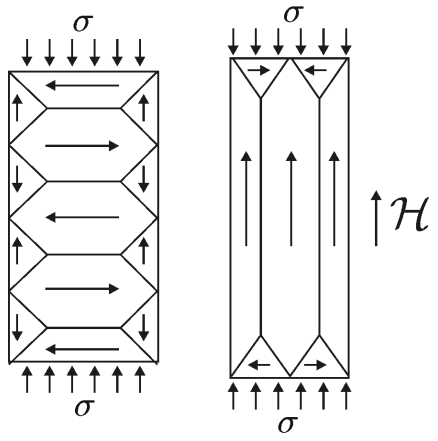

Figure 1.11: Preloaded magnetostrictive material

Magnetostrictive materials are typically mechanically biased in normal operation. A compressive load is applied to the material, which, due to the magneto-elastic coupling, forces the domain structure to orient perpendicular to the applied force. Then, as a magnetic field is introduced, the domain structure rotates producing the maximum possible strain in the material (Fig.1.11).

The highest room temperature magnetostriction of a pure element does not exceed 60 microstrain (Cobalt). By alloying elements, one can achieve *giant* magnetostriction under relatively small fields. Terfenol-D[8] (alloys of the form $Tb_xDy_{1-x}Fe_2$) exhibits the greatest magnetostrictive effects of any commercially available material. Operated under a mechanical-bias, it strains to about 2000 microstrain in a magnetic field of 2 kOe at room temperature (1 A-turn/m= $4\pi\ 10^{-3}$ Oe).

[6]The discovery of magnetostriction is attributed to J. Joule - XIXth century

[7]This reciprocal effect is known as the Villari effect

[8]The name Terfenol-D is derived from Terbium (Tb); Fe; the Naval Ordnance Laboratory (it was first discovered in the 70's by a research group led by Clark at the Naval Surface Warfare Center in Silver Spring, Md); and Dysprosium (Dy).

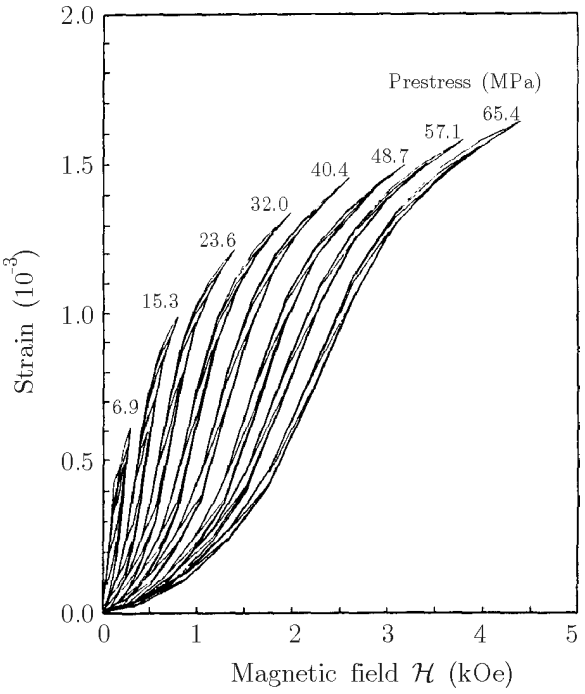

Figure 1.12: Strain / magnetic field curves for $Tb_{0.3}Dy_{0.7}Fe_{1.93}$ (Moffett et al., 1991)

The magnetostrictive properties of Terfenol-D are strongly dependent on the magnetic and mechanical bias conditions (Moffett et al., 1991). Figure 1.12 shows extension strain / magnetic field curves for different prestress conditions.

As the the compressive prestress is increased, larger values of field bias as well as larger drive field are required. The coupling factor decreases with increasing magnetic and mechanical bias. At high drive levels, saturation occurs and the coupling factor becomes independent of the bias conditions.

Electrostriction is the dependance of the state of strain of a ferroelectric material to the even powers of the applied electric field (mainly the second order)(Anderson et al., 1990). It is a universal property of all dielectrics but it can only be observed in materials with high dielectric coefficients such as *PMN* (Lead Magnesium Niobate) which exhibits an electrostrictive strain up to 0.1% (Fig.1.13).

$$\begin{aligned} D &= dT + \varepsilon^T E \\ S &= sT + dE + d^* E^2 \end{aligned} \tag{1.16}$$

where D is the electrical displacement, E the electric field, S the strains, T the stresses, d the piezoelectric coupling, s the compliance and d^* the electrostrictive coupling (the dE term is usually neglected in this case).

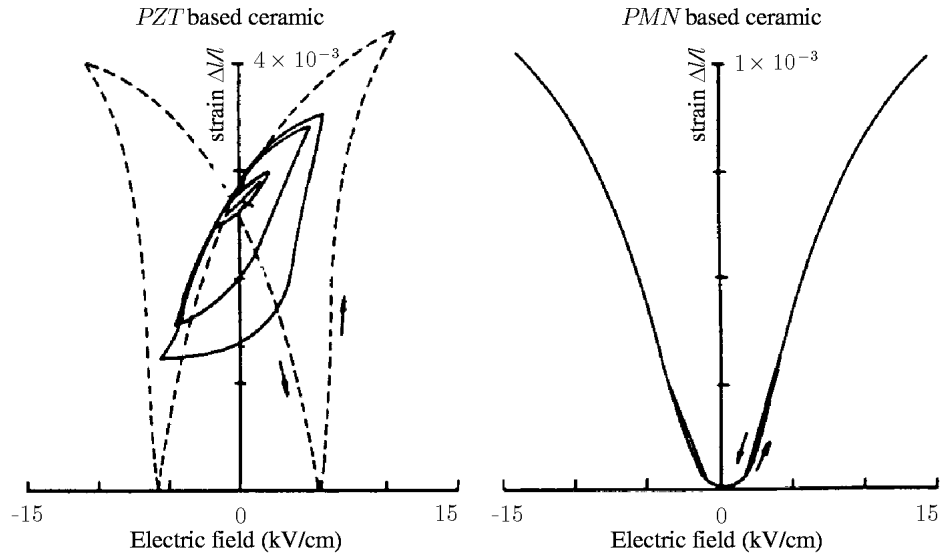

Figure 1.13: Piezoelectricity (*PZT* ceramics) - Electrostriction (*PMN* ceramics)

1.3.3 Electro / magneto-rheological fluids

Magnetorheological (MR) fluids and electro-rheological (ER) fluids are materials that respond to an applied magnetic or electric field with a important change in rheological behaviour. This is more a *semi-smart* behaviour in the sense that the application of a *third party* field (here electric or magnetic) will act on a *classical* coupling (viscosity) and that there is no reciprocal effect.

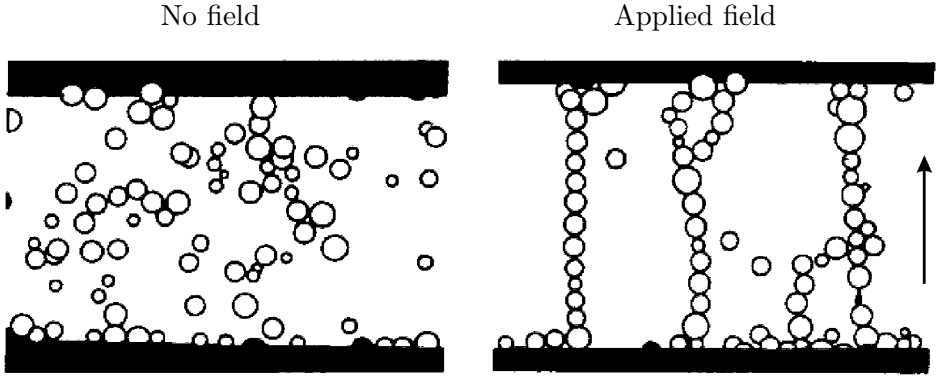

Figure 1.14: Particles alignment due to an applied field

These fluids are non-colloidal suspension of polarisable small particles (a few μm). Their essential characteristic is their ability to reversibly change from a free-flowing, linear viscous liquid to a semi-solid with a controllable yield strength in milliseconds when exposed to a magnetic or electric field. In the absence of an applied field, controllable fluids are reasonably well approxi-

mated as Newtonian liquids (Carlson & Sproston, 2000).

The magneto-rheological response results from the polarization induced in the suspended particles by application of an external field. The interaction between the resulting induced dipoles causes particles to align and form chain-like structures parallel to the applied field (Fig.1.14). These chain-like structures restrict the motion of the fluid, thereby increasing its apparent viscosity. The mechanical energy needed to break these chain-like structures increases with the applied field. For most engineering applications a simple *Bingham* (Eq.1.17) plastic model is sufficient for describing the essential, field-dependent fluid characteristics. In this model, the total yield stress τ is given by:

$$\tau = \tau(H)sign(\dot{\gamma}) + \eta_p\dot{\gamma} \tag{1.17}$$

where $\tau(H)$ is the yield stress caused by the applied magnetic or electric field H, $\dot{\gamma}$ is the shear rate and η_p is the field independent plastic viscosity defined as the slope of the measured shear stress versus shear strain rate relationship.

Interest in controllable fluids stems from their ability to provide simple, quiet, rapid-response interfaces between electronic controls and mechanical systems. The ability of controllable fluids to be directly used as fast-acting, fluid valves with no moving parts in semi-active vibration control systems has been one of the main motivating factors for the development of such fluids. Typical characteristics for magneto and electro - rheological fluids are listed in Table 1.4. It must be noted that the maximum shear stress obtainable using *MR* fluids is about 20 times bigger than the maximum shear stress obtainable using *ER* fluids.

Property	*ER* fluid	*MR* fluid
Yield Strenght τ (field)	$2-5$ kPa ($3-5$ kV/mm)	$50-100$ kPa ($150-250$ kA/m)
Viscosity η (no field)	$0.2-0.3$ Pa.s at 25 $^\circ$C	$0.2-0.3$ Pa.s at 25 $^\circ$C
Operating temperature	-25 to $+125$ $^\circ$C	-40 to $+150$ $^\circ$C
Response time	ms	ms
Density	$1-2$ g/cm^3	$3-4$ g/cm^3

Table 1.4: Comparison of properties of typical *ER* and *MR* fluids. (Carlson et al., 1995)

Chapter 2

Constitutive equations

In a first section, the unidimensional constitutive equations are established starting from the electrostatics point of view. The general thermopiezoelectric constitutive equations are derived from the laws of thermodynamics in the second section. Linear constitutive equations of piezoelectricity and further simplifications of the coupling matrices due to crystal symmetries are presented in the third section. The particular case of plane stress state is considered in the last section of this chapter.

2.1 Unidimensional

2.1.1 Polarization

The electric charge $\pm Q$ appearing on 2 parallel conductive plates separated by vacuum is related to the applied voltage ϕ_0 by the capacitance $C_0 = Q/\phi_0$ of the system. Substituting the vacuum by an insulating material and suppressing the electrical source at the same time, a voltage $\phi < \phi_0$ is observed (Faraday's experiment, 1837). The total electric charge on the plates being unchanged, this implies that the capacitance of the system has been increased: $C = Q/\phi > C_0 = Q/\phi_0$.

The capacitance is related to the surface Ω of the plates and to distance d between them by $C_0 = \varepsilon_0\ \Omega/d$ for the vacuum defining $\varepsilon_0 = (36\pi 10^9)^{-1}$ F/m, the permittivity of the vacuum. Similarily, we have $C = \varepsilon\ \Omega/d$ for an ideal dielectric, defining $\varepsilon = \varepsilon_r\varepsilon_0$, the absolute permittivity of the dielectric and ε_r, its relative one.

To explain Faraday's experiment, the following hypothesis has been made: *In an ideal dielectric material, the polarization is induced only by the applied electric field.*

Applying a voltage ϕ_0 induces a uniform electric field E, the charge appearing is $\pm Q = \pm\varrho\Omega$ (ϱ being the charge density on the surface).

When the dielectric is inserted, it gets polarized under the electrostatic field. Two kinds of charges can be distinguished (Fig.2.1): free charges Q_1 and bound charges Q_2. The bound charges Q_2 being locally compensated by the polarization charges inside the dielectric, only the

free charges Q_1 contributes to the voltage ϕ.

$$\phi = \frac{Q}{C} = \frac{Q}{\varepsilon_r C_0} = \frac{Q_1}{C_0} \tag{2.1}$$

The total charge is given by:

$$Q = Q_1 + Q_2 = \frac{Q}{\varepsilon_r} + Q\left(1 - \frac{1}{\varepsilon_r}\right) \tag{2.2}$$

and the charge density

$$\varrho = \frac{\varrho}{\varepsilon_r} + \varrho\left(1 - \frac{1}{\varepsilon_r}\right) \tag{2.3}$$

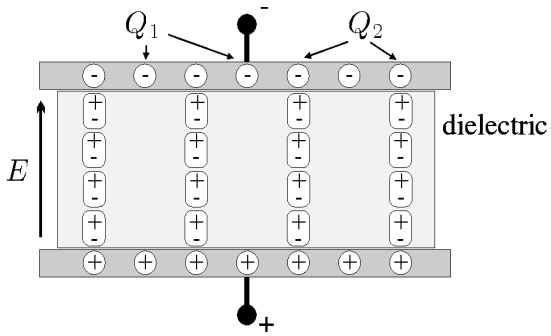

Figure 2.1: Charges in a dielectric-filled plane capacitor

Let us define:

$$D = \varrho \qquad \textbf{displacement field} \tag{2.4}$$

$$P = \varrho\left(1 - \frac{1}{\varepsilon_r}\right) \qquad \textbf{polarization} \tag{2.5}$$

$$E = \frac{\phi}{d} = \frac{Q}{\varepsilon_r C_0}\frac{1}{d} = \frac{\varrho}{\varepsilon_r \varepsilon_0} = \frac{\varrho}{\varepsilon} \qquad \textbf{electric field} \tag{2.6}$$

Which leads to

$$D = \varepsilon E = \varepsilon_0 E + P \tag{2.7}$$

and

$$P = (\varepsilon - \varepsilon_0)\, E \tag{2.8}$$

2.1.2 Piezoelectricity

In an unstressed one-dimensional dielectric medium, the dielectric displacement D (charge per unit area, expressed in $\mathrm{Cb/m^2}$) is related to the electric field E (V/m) and the polarization P ($\mathrm{Cb/m^2}$) by Equ.(2.7).

Similarly, in a one-dimensional elastic body placed in a zero electric field, the stress T (N/m^2) and the strain S are related by

$$T = cS \tag{2.9}$$

where c is the stiffness of the material (Young's modulus).

For a piezoelectric material, the electrical and mechanical constitutive equations are coupled. A strain S in the material induces a polarization eS by the direct piezoelectric effect. The total induced polarization is given by

$$P = (\varepsilon - \varepsilon_0)E + eS \tag{2.10}$$

Conversely, an applied electric field E tends to align the internal dipoles, inducing stresses $-e\,E$ in the material by the inverse piezoelectric effect. The coupled equations finally become:

$$\boxed{T = c^E S - e\ E} \tag{2.11}$$

$$\boxed{D = e\ S + \varepsilon^S E} \tag{2.12}$$

In equation (2.11), the piezoelectric constant e relates the stress to the electric field E in the absence of mechanical strain and c^E refers to the stiffness when the electric field is constant. In equation (2.12), e relates the electric charge per unit area D to the strain under a zero electric field (short-circuited electrodes); e is expressed in NV^{-1}m^{-1} or Cb/m^2. ε^S is the permittivity under constant strain.

Equation (2.11) is the starting point for the formulation of the equation of a piezoelectric actuator, while equation (2.12) is that for a sensor.

In the next section, the general constitutive equations for a thermopiezoelectric continuum are first established starting from the basic thermodynamic principles. The linear constitutive equations for a piezoelectric material are written next, introducing standard engineering tensorial notations.

2.2 General constitutive equations

2.2.1 Thermodynamics

The conservation of energy for the linear piezoelectric continuum results in the first law of thermodynamics considering three contributions to the variation of the stored internal energy: the work of external forces, the work of applied electric fields and the thermal energy brought to the system.

$$dU = T_{ij}dS_{ij} + E_i dD_i + \Theta d\varsigma \tag{2.13}$$

where T_{ij} and S_{ij} are respectively the stress and the strain tensors, E_i and D_i are respectively the electric field and the electric displacement vectors, $\Theta = \Theta_0 + \theta$, the temperature ($\Theta_0$,

the reference temperature and $\theta \ll \Theta_0$, a small temperature change), ς the entropy and U is the stored energy density for the piezoelectric continuum. The summation convention for all repeated indices is assumed.

Let us write the constitutive equations using $\{S\}, \{E\}$ and θ as independant variables. We have

$$dT_{ij} = \frac{\partial T_{ij}}{\partial S_{kl}} dS_{kl} + \frac{\partial T_{ij}}{\partial E_m} dE_m + \frac{\partial T_{ij}}{\partial \theta} d\theta \tag{2.14}$$

$$dD_i = \frac{\partial D_i}{\partial S_{kl}} dS_{kl} + \frac{\partial D_i}{\partial E_m} dE_m + \frac{\partial D_i}{\partial \theta} d\theta \tag{2.15}$$

$$d\varsigma = \frac{\partial \varsigma}{\partial S_{kl}} dS_{kl} + \frac{\partial \varsigma}{\partial E_m} dE_m + \frac{\partial \varsigma}{\partial \theta} d\theta \tag{2.16}$$

defining (See Fig.2.2)

$\frac{\partial T_{ij}}{\partial S_{kl}}$	elasticity	$\frac{\partial T_{ij}}{\partial E_m}$	inverse piezoelectricity	$\frac{\partial T_{ij}}{\partial \theta}$	thermal stress
$\frac{\partial D_i}{\partial S_{kl}}$	direct piezoelectricity	$\frac{\partial D_i}{\partial E_m}$	permittivity	$\frac{\partial D_i}{\partial \theta}$	pyroelectricity
$\frac{\partial \varsigma}{\partial S_{kl}}$	piezocaloric effect	$\frac{\partial \varsigma}{\partial E_m}$	electrocaloric effect	$\frac{\partial \varsigma}{\partial \theta}$	heat capacity

To describe the behaviour of the thermopiezoelectric continuum as a thermodynamic system, the thermoelectric *Gibbs* state function (free energy) G is introduced:

$$G = U - E_i D_i - \Theta \varsigma \tag{2.17}$$

from equations (2.13) and (2.17), there results

$$dG = T_{ij} dS_{ij} - D_i dE_i - \varsigma d\theta \tag{2.18}$$

and therefore,

$$T_{ij} = \frac{\partial G}{\partial S_{ij}} \tag{2.19}$$

$$D_i = -\frac{\partial G}{\partial E_i} \tag{2.20}$$

$$\varsigma = -\frac{\partial G}{\partial \theta} \tag{2.21}$$

by deriving a second time, one gets:

$$\frac{\partial T_{ij}}{\partial E_m} = \frac{\partial D_m}{\partial S_{ij}} \tag{2.22}$$

$$\frac{\partial T_{ij}}{\partial \theta} = \frac{\partial \varsigma}{\partial S_{ij}} \tag{2.23}$$

$$\frac{\partial D_i}{\partial \theta} = \frac{\partial \varsigma}{\partial E_i} \tag{2.24}$$

establishing that the coefficients relative to direct and inverse effects are equals. Let us define

$\frac{\partial T_{ij}}{\partial S_{kl}} = c_{ijkl}$	$\frac{\partial T_{ij}}{\partial E_m} = e_{ijm}$	$\frac{\partial T_{ij}}{\partial \theta} = \lambda_{ij}$
$\frac{\partial D_i}{\partial S_{kl}} = e_{kli}$	$\frac{\partial D_i}{\partial E_m} = \varepsilon_{im}$	$\frac{\partial D_i}{\partial \theta} = p_i$
$\frac{\partial \varsigma}{\partial S_{kl}} = \lambda_{kl}$	$\frac{\partial \varsigma}{\partial E_m} = p_m$	$\frac{\partial \varsigma}{\partial \theta} = \alpha$

Considering a linear behaviour, G can be written

$$G = \frac{1}{2} c^E_{ijkl} S_{ij} S_{kl} - e_{kij} E_k S_{ij} - \frac{1}{2} \varepsilon^S_{ij} E_i E_j - \frac{1}{2} \alpha \theta^2 - \lambda_{ij} S_{ij} \theta - p_i \theta E_i \tag{2.25}$$

c_{ijkl}, e_{kij}, λ_{ij}, ε_{ij}, p_i and α are respectively the elastic, the piezoelectric, the thermal expansion coefficient, the dielectric and pyroelectric constants and the specific heat. From Equ.(2.25), and Equ.(2.19) to Equ.(2.21), there results the thermopiezoelectric constitutive equations:

$$T_{ij} = c^E_{ijkl} S_{kl} - e_{kij} E_k - \lambda_{ij} \theta \tag{2.26}$$

$$D_m = e_{mkl} S_{kl} + \varepsilon^S_{mk} E_k + p_i \theta \tag{2.27}$$

$$\varsigma = \lambda_{kl} S_{kl} + p^S_k E_k + \alpha \theta \tag{2.28}$$

2.2.2 Linear piezoelectricity

An important characteristic of piezoeletric materials compared to other *smart materials* is its linear behavior within a certain range.

In this section, we use the same notations as in (IEEE std) and only the piezoelectric coupling is considered (the thermoelectric terms are neglected). In linear piezoelectricity, the equations of linear elasticity are coupled to the charge equation of electrostatics by the means of the piezoelectric constants. The quasielectrostatic approach is adequate because the phase velocities of acoustic waves are several order of magnitude less than the velocities of electromagnetic waves.

Taking advantage of the symmetries of the mechanical tensors, a compressed matrix notation is introduced in place of the tensor notation. This matrix notation consists of replacing indices ij or kl by p or q according to Table 2.1 (the non diagonal terms of the deformation tensor are

doubled). The following identifications are made:

$$c_{ijkl} \equiv c_{pq} \tag{2.29}$$
$$e_{ikl} \equiv e_{iq} \tag{2.30}$$
$$T_{ij} \equiv T_p \tag{2.31}$$
$$S_{ij} \equiv S_p \quad \text{when} \quad i = j \tag{2.32}$$
$$2S_{ij} \equiv S_p \quad \text{when} \quad i \neq j \tag{2.33}$$

ij or kl	p or q
11	1
22	2
33	3
23 or 32	4
13 or 31	5
12 or 21	6

Table 2.1: Matrix notation

The constitutive equations read

$$\begin{array}{rcrcl} \{T\} &=& [c^E]\{S\} &-& [e]^T\{E\} \\ \{D\} &=& [e]\{S\} &+& [\varepsilon^S]\{E\} \end{array} \tag{2.34}$$

or (alternate forms using alternative choices of independant variables)

$$\begin{array}{rcrcl} \{S\} &=& [s^E]\{T\} &+& [d]^T\{E\} \\ \{D\} &=& [d]\{T\} &+& [\varepsilon^T]\{E\} \end{array} \tag{2.35}$$

$$\begin{array}{rcrcl} \{S\} &=& [s^D]\{T\} &+& [g]^T\{D\} \\ \{E\} &=& -[g]\{T\} &+& [\beta^T]\{D\} \end{array} \tag{2.36}$$

$$\begin{array}{rcrcl} \{T\} &=& [c^D]\{S\} &-& [h]^T\{D\} \\ \{E\} &=& -[h]\{S\} &+& [\beta^S]\{D\} \end{array} \tag{2.37}$$

with

$\{T\} = \left\{ \begin{array}{cccccc} T_{11} & T_{22} & T_{33} & T_{23} & T_{13} & T_{12} \end{array} \right\}^T$ is the stress vector

$\{S\}$, the deformation vector

$\{E\}$, the electric field vector

$\{D\}$, the electric displacement vector

$[c]$ and $[s]$, the elasticity constants matrices

$[\varepsilon]$ and $[\beta]$, the dielectric constants matrix

$[d]$, $[e]$, $[g]$ and $[h]$, the piezoelectric constants matrix

and supercripts D, E, S and T indicate values at D, E, S and T constant respectively

The element d_{ij} of $[d]$ represents the coupling between the electric field in the direction i (if a poling occured, its direction is taken as direction 3) and the strain in the j direction. $S_j = d_{ij}E_i$. The following relations between dielectric, elastic, and piezoelectric constants are verified

$$\left[c^E\right]\left[s^E\right] = \left[c^D\right]\left[s^D\right] = I_6 \tag{2.38}$$
$$\left[\beta^S\right]\left[\varepsilon^S\right] = \left[\beta^T\right]\left[\epsilon^T\right] = I_3 \tag{2.39}$$
$$\left[c^D\right] = \left[c^E\right] + [e]^T[h] \tag{2.40}$$
$$\left[s^D\right] = \left[c^D\right] - [d]^T[g] \tag{2.41}$$
$$\left[\varepsilon^T\right] = \left[\varepsilon^S\right] + [d]^T[e] \tag{2.42}$$
$$\left[\beta^S\right] = \left[\beta^T\right] - [g]^T[h] \tag{2.43}$$
$$[e] = [d]\left[c^E\right] \tag{2.44}$$
$$[d] = \left[\varepsilon^T\right][g] \tag{2.45}$$
$$[g] = [h]\left[s^D\right] \tag{2.46}$$
$$[h] = \left[\beta^S\right][e] \tag{2.47}$$

Due to crystal symmetries, the piezoelectric coupling matrices $[d]$ and $[e]$ may have only few non zero elements (Cady, 1946; Nye, 1957). Symmetries in the piezoelectric coupling matrix for all crystal classes are described on Fig.2.3 and Fig.2.4.

Examples of piezoelectric coupling matrices:

Quartz $[d]_{\text{Quartz}} = \begin{bmatrix} -2.3 & -2.3 & 0 & -0.67 & 0 & 0 \\ 0 & 0 & 0 & 0 & 0.67 & 4.6 \\ 0 & 0 & 0 & 0 & 0 & 0 \end{bmatrix} 10^{-12}\,\text{m/V}$

PZT $[d]_{\text{PXE5}} = \begin{bmatrix} 0 & 0 & 0 & 0 & 515 & 0 \\ 0 & 0 & 0 & 515 & 0 & 0 \\ -175 & -175 & 362 & 0 & 0 & 0 \end{bmatrix} 10^{-12}\,\text{m/V}$

PVF$_2$ $[d]_{\text{Solef}} = \begin{bmatrix} 0 & 0 & 0 & 0 & 0 & 0 \\ 0 & 0 & 0 & 0 & 0 & 0 \\ 23 & 3 & -33 & 0 & 0 & 0 \end{bmatrix} 10^{-12}\,\text{m/V}$

(Solef Mono-oriented 130 μm)

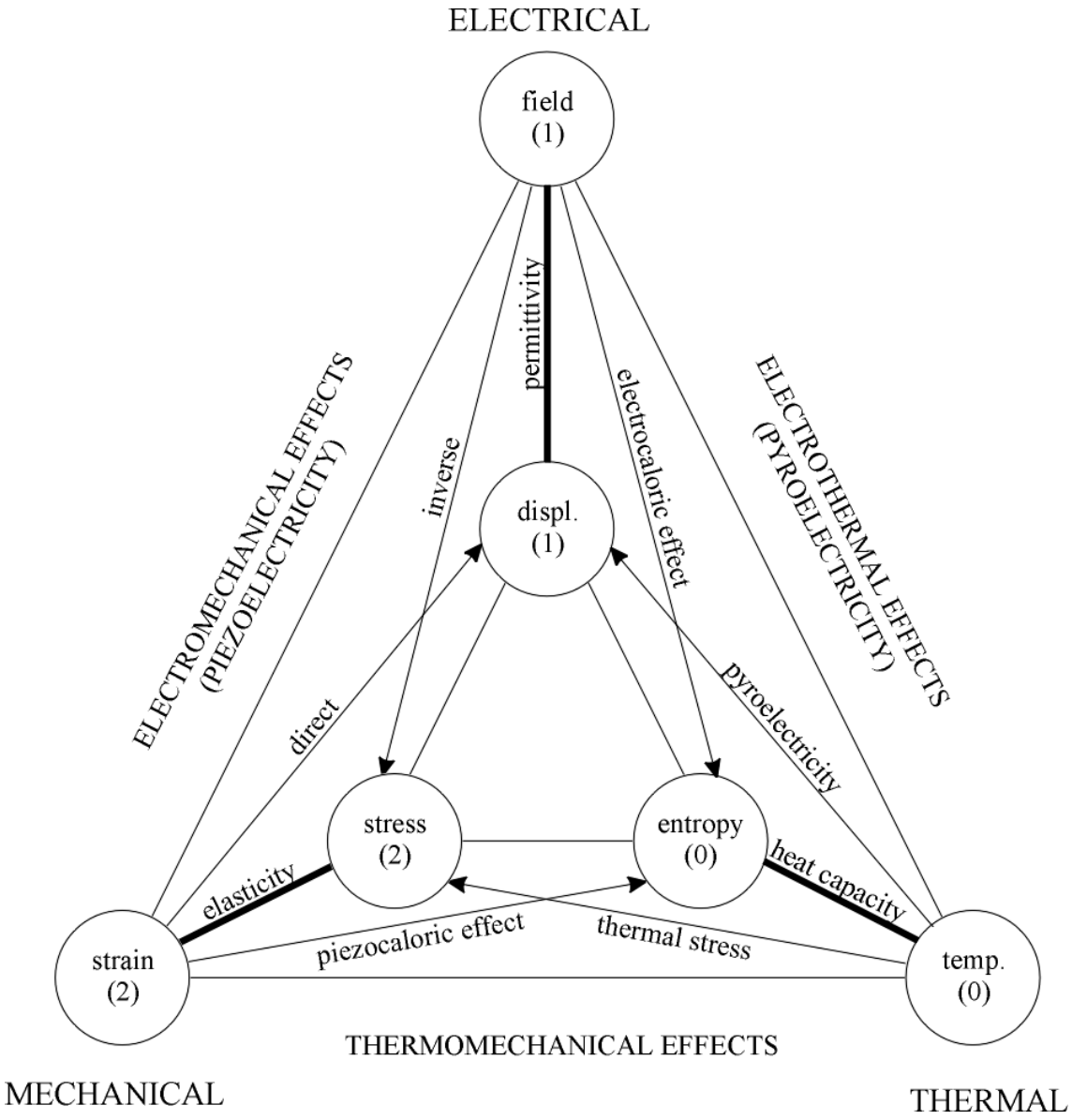

Figure 2.2: Thermodynamics

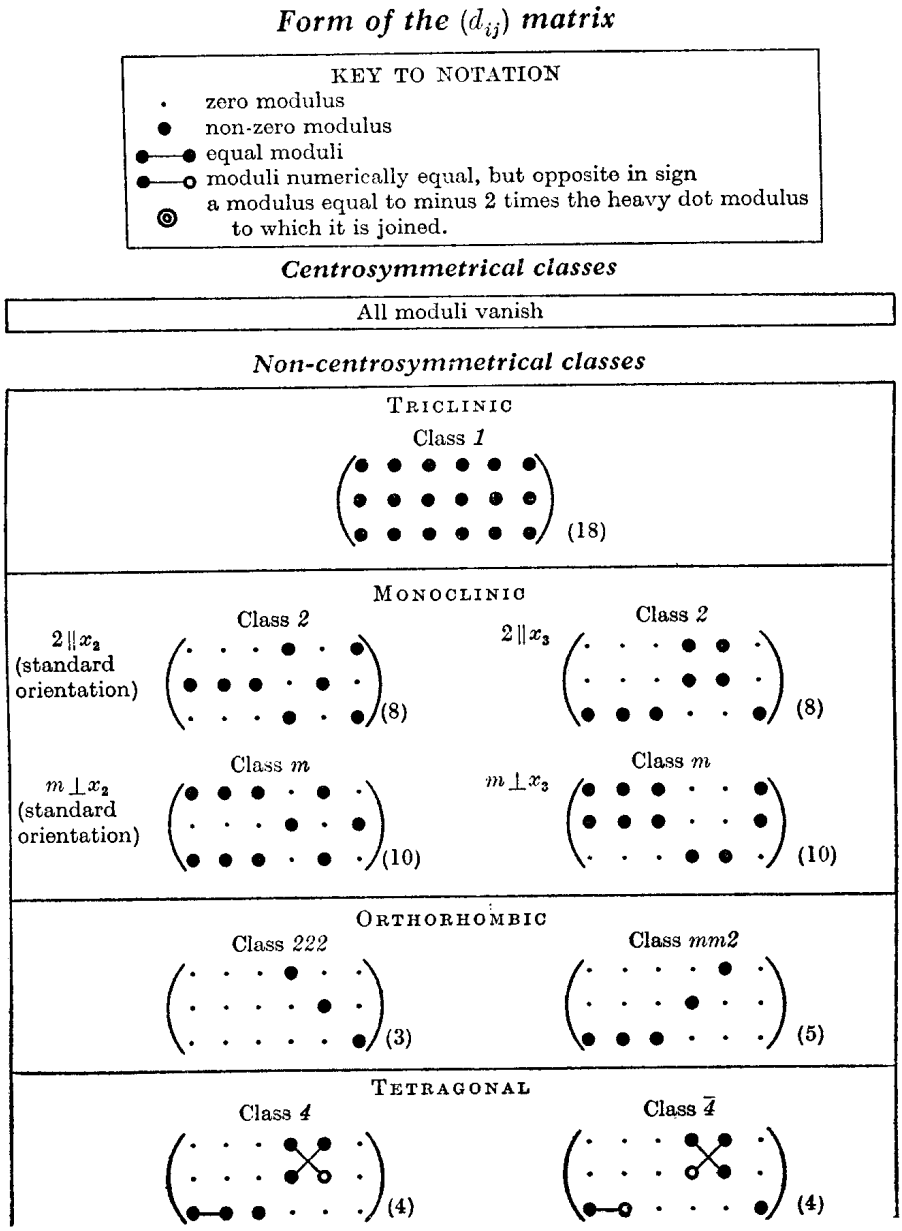

Figure 2.3: Symmetries in the piezoelectric coupling matrix for all crystal classes - Part I (Nye, 1957, chap. 7)

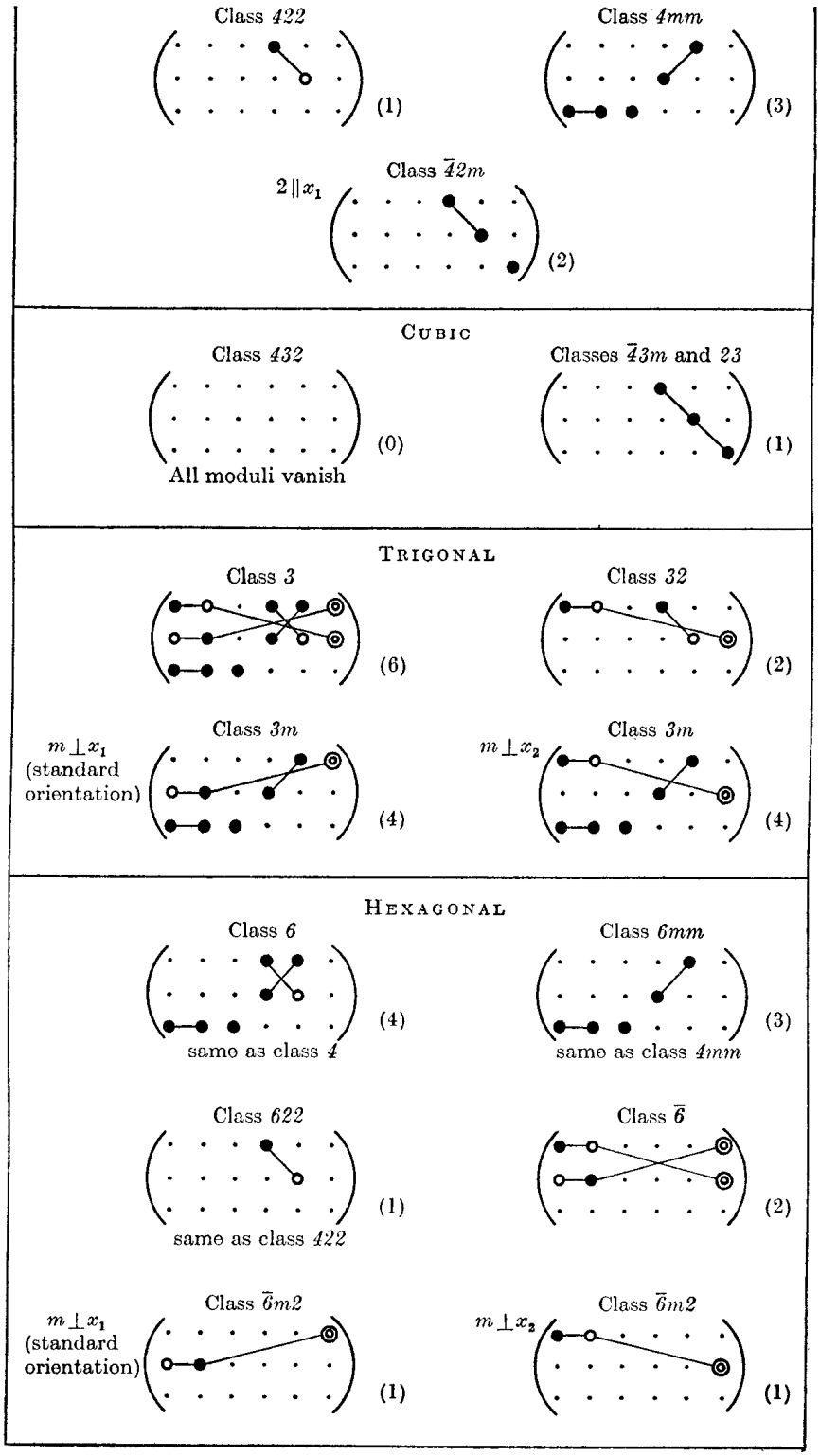

Figure 2.4: Symmetries in the piezoelectric coupling matrix for all crystal classes - Part II (Nye, 1957, chap. 7)

2.3 Piezoelectric laminate

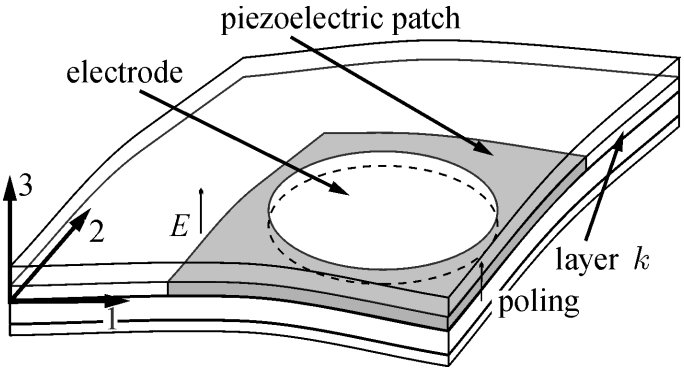

Figure 2.5: Composite shell with embedded piezoelectric patch

We consider a shell structure with embedded piezoelectric patches covered with electrodes. The poling direction and the electric and displacement fields direction are parallel, normal to the patches (Fig.2.5). The piezoelectric patches are parallel to the mid-plane and orthotropic in their plane.

The following hypothesis are made:

- **One dimension is significantly less than the others**
- **Plane stress hypothesis:** $\sigma_{zz} = 0$, using classical engineering notations
- ***Kirchhoff* assumption:** A fiber normal to the mid plane remains normal to the mid plane after deformation

$$\{S\} = \{S_0\} + z\,\{\kappa\} \tag{2.48}$$

  where $\{S_0\}$ is the mid plane strain and $\{\kappa\}$, the mid plane curvature. The strain and stress vectors written in axes (xy) are given in classical engineering notation respectively by $\{S\} = \{\epsilon_x \ \epsilon_y \ \gamma_{xy}\}^T$ and $\{T\} = \{\sigma_x \ \sigma_y \ \tau_{xy}\}^T$. The *Kirchhoff* hypothesis does not account for any transverse shear ($\gamma_{yz} = \gamma_{xz} = 0$).

- **Uniform electric field and displacement** across the thickness and aligned on the normal to the mid-plane (direction 3).

$$\{E\} = \left\{ \begin{array}{c} 0 \\ 0 \\ E \end{array} \right\} \tag{2.49}$$

$$\{D\} = \left\{ \begin{array}{c} 0 \\ 0 \\ D \end{array} \right\} \tag{2.50}$$

- **Linear piezoelectricity** for each piezoelectric layer k, (we assume that the piezoelectric principal axes are parallel the structural orthotropy axes and that the poling direction is

direction 3). The constitutive equations for the k^{th} layer become (e_{36} is assumed to be zero, which is the case for most commonly used piezomaterials in laminar design: *PZT* and *PVDF* - see §2.2.2)

$$\{T\} = [c]_k \{S\} - \left\{ \begin{array}{c} e_{31} \\ e_{32} \\ 0 \end{array} \right\}_k E_k \tag{2.51}$$

$$D_k = \left\{ \begin{array}{ccc} e_{31} & e_{32} & 0 \end{array} \right\}_k \{S\} + \varepsilon_k E_k \tag{2.52}$$

where $[c]_k$ is the elastic coefficients matrix of the k^{th} layer (stiffness matrix in the principal material axes).

2.3.1 Single layer in plane stress

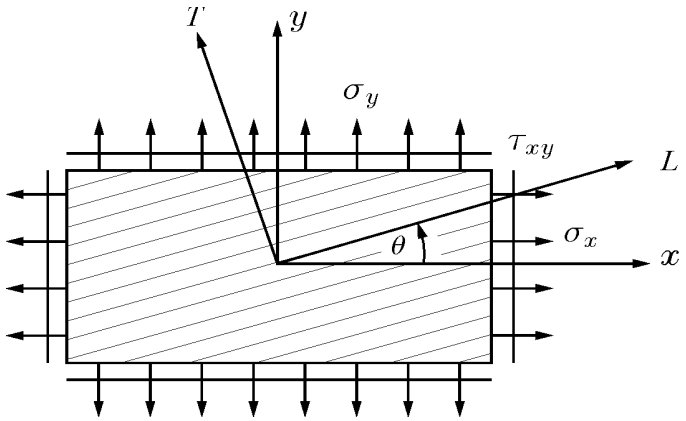

Figure 2.6: Lamina and laminate coordinate systems

Let us first consider a single layer at the purely mechanical point of vue (stress/strain relationship). An orientation angle θ_k between the material axes LT of layer k and the structural axes xy is assumed (Fig.2.6). θ_k is taken positive from x to L. The transformation matrices $[R_T]_k$ and $[R_S]_k$ relate the stresses and strains written in the material axes (LT) to the stresses and strains written in the composite axes (xy). We have:

$$\left\{ \begin{array}{c} \sigma_L \\ \sigma_T \\ \tau_{LT} \end{array} \right\} = [R_T]_k \left\{ \begin{array}{c} \sigma_x \\ \sigma_y \\ \tau_{xy} \end{array} \right\} \tag{2.53}$$

$$\left\{ \begin{array}{c} \epsilon_L \\ \epsilon_T \\ \frac{1}{2}\gamma_{LT} \end{array} \right\} = [R_T]_k \left\{ \begin{array}{c} \epsilon_x \\ \epsilon_y \\ \frac{1}{2}\gamma_{xy} \end{array} \right\} \tag{2.54}$$

$$\left\{ \begin{array}{c} \epsilon_L \\ \epsilon_T \\ \gamma_{LT} \end{array} \right\} = [R_S]_k \left\{ \begin{array}{c} \epsilon_x \\ \epsilon_y \\ \gamma_{xy} \end{array} \right\} \tag{2.55}$$

with the transformation matrices

$$[R_T]_k = \begin{bmatrix} \cos^2\theta_k & \sin^2\theta_k & 2\sin\theta_k\cos\theta_k \\ \sin^2\theta_k & \cos^2\theta_k & -2\sin\theta_k\cos\theta_k \\ -\sin\theta_k\cos\theta_k & \sin\theta_k\cos\theta_k & \cos^2\theta_k - \sin^2\theta_k \end{bmatrix} \tag{2.56}$$

$$[R_S]_k = \begin{bmatrix} \cos^2\theta_k & \sin^2\theta_k & \sin\theta_k\cos\theta_k \\ \sin^2\theta_k & \cos^2\theta_k & -\sin\theta_k\cos\theta_k \\ -2\sin\theta_k\cos\theta_k & 2\sin\theta_k\cos\theta_k & \cos^2\theta_k - \sin^2\theta_k \end{bmatrix} \tag{2.57}$$

As we can write

$$\begin{Bmatrix} \epsilon_x \\ \epsilon_y \\ \gamma_{xy} \end{Bmatrix} = [R_S]_k^{-1} \begin{Bmatrix} \epsilon_L \\ \epsilon_T \\ \gamma_{LT} \end{Bmatrix} \tag{2.58}$$

It follows that $[R(\theta_k)]^{-1} = [R(-\theta_k)]$

The stiffness matrix $\left[\overline{Q}\right]_k$ of the k^{th} layer in the composite axes is defined by

$$\begin{Bmatrix} \sigma_x \\ \sigma_y \\ \tau_{xy} \end{Bmatrix} = \left[\overline{Q}\right]_k \begin{Bmatrix} \epsilon_x \\ \epsilon_y \\ \gamma_{xy} \end{Bmatrix} \tag{2.59}$$

Since

$$\begin{Bmatrix} \sigma_x \\ \sigma_y \\ \tau_{xy} \end{Bmatrix} = [R_T]_k^{-1} \begin{Bmatrix} \sigma_L \\ \sigma_T \\ \tau_{LT} \end{Bmatrix} = [R_T]_k^{-1} [c]_k \begin{Bmatrix} \epsilon_L \\ \epsilon_T \\ \gamma_{LT} \end{Bmatrix} = [R_T]_k^{-1} [c]_k [R_S]_k \begin{Bmatrix} \epsilon_x \\ \epsilon_y \\ \gamma_{xy} \end{Bmatrix} \tag{2.60}$$

It is related to the elastic coefficients matrix $[c]_k$ by:

$$\left[\overline{Q}\right]_k = [R_T]_k^{-1} [c]_k [R_S]_k \tag{2.61}$$

As we have $[R_T]_k^{-1} = [R_S]_k^T$ and $[c]_k$ symmetric, $\left[\overline{Q}\right]_k$ is also symmetric.

Let us now introduce the piezoelectric coupling terms. The electric field is related to the voltage ϕ_k across the thickness h_k of the layer k:

$$E_k = -\phi_k / h_k \tag{2.62}$$

Starting from the constitutive equation (2.51) for the piezoelectric layer k in the material principal axes (LT), we get, in composite axes (xy):

$$\begin{aligned} \{T\}^{(xy)} = [R_T]_k^{-1} \{T\}^{(LT)} &= [R_T]_k^{-1} [c]_k [R_S]_k \{S\}^{(xy)} - [R_T]_k^{-1} \begin{Bmatrix} e_{31} \\ e_{32} \\ 0 \end{Bmatrix}_k E_k \\ &= \left[\overline{Q}\right]_k \{S\}^{(xy)} + [R_T]_k^{-1} \begin{Bmatrix} e_{31} \\ e_{32} \\ 0 \end{Bmatrix}_k \frac{\phi_k}{h_k} \end{aligned} \tag{2.63}$$

2.3.2 Multilayer

A laminate is formed from two or more layers bonded together to act as a single layer material. The bond between two layers is assumed to be perfect, so that the displacements remain continuous across the bond. The classical theory for multilayered materials is followed and complemented with electromechanical coupling terms.

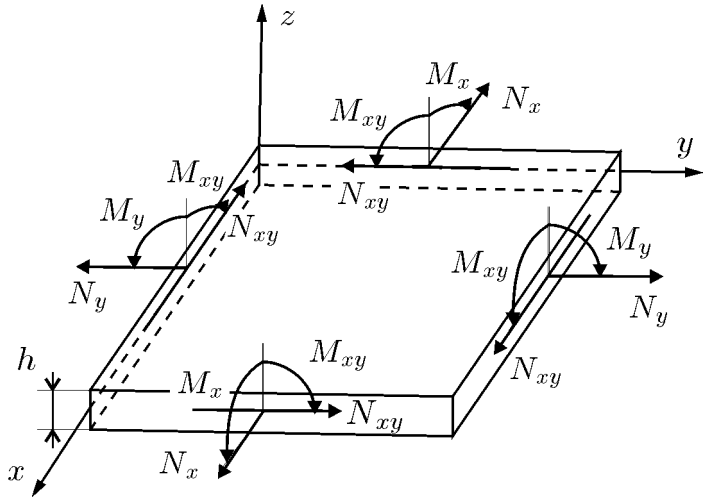

Figure 2.7: Resultant efforts (*Kirchhoff*)

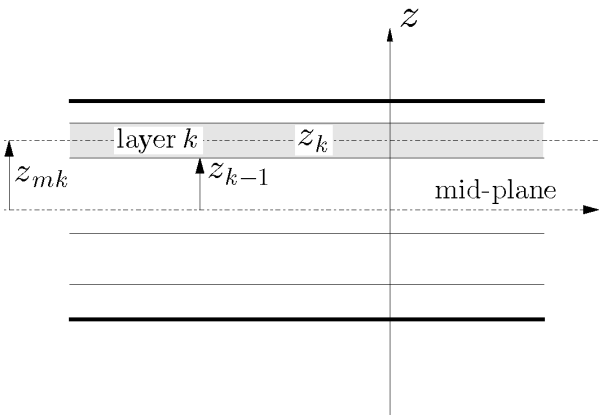

Figure 2.8: Multilayered material

In-plane efforts $\{N\}$ and bending moments $\{M\}$ (Fig.2.7) can be determined by integrating the stresses over the thickness of the multilayered material (Agarwal & Broutman, 1990, Chap.6).

$$\{N\} = \int_{-\frac{h}{2}}^{+\frac{h}{2}} \{T\}\, dz$$

$$\{M\} = \int_{-\frac{h}{2}}^{+\frac{h}{2}} \{T\} z\, dz$$

Integrating equation (2.63) over the thickness, one gets the resultant normal effort and bending moment:

$$\left\{ \begin{array}{c} N \\ M \end{array} \right\} = \left[\begin{array}{cc} A & B \\ B & D \end{array} \right] \left\{ \begin{array}{c} S_0 \\ \kappa \end{array} \right\} + \sum_{k=1}^{n} \int_{z_{k-1}}^{z_k} \left[\begin{array}{c} I_3 \\ z\, I_3 \end{array} \right] [R_T]_k^{-1} \left\{ \begin{array}{c} e_{31} \\ e_{32} \\ 0 \end{array} \right\}_k \frac{\phi_k}{h_k} dz \tag{2.64}$$

where n is the number of piezoelectric layers and z_k the coordinate of layer k relative to the mid-plane as defined on Fig.2.8.

The extension, bending and coupling matrices A, B, and D are given by the classical relationships for multilayered materials:

$$[A] = \sum_{k=1}^{n} \left[\overline{Q}\right]_k (z_k - z_{k-1}) \quad \textbf{extension} \tag{2.65}$$

$$[B] = \frac{1}{2} \sum_{k=1}^{n} \left[\overline{Q}\right]_k (z_k^2 - z_{k-1}^2) \quad \textbf{coupling} \tag{2.66}$$

$$[D] = \frac{1}{3} \sum_{k=1}^{n} \left[\overline{Q}\right]_k (z_k^3 - z_{k-1}^3) \quad \textbf{bending} \tag{2.67}$$

Putting all the constant terms out of the integral sign, the second term of Equ.(2.64) becomes:

$$\begin{aligned} & \ldots + \sum_{k=1}^{n} \frac{1}{h_k} \left(\int_{z_{k-1}}^{z_k} \left[\begin{array}{c} I_3 \\ z\, I_3 \end{array} \right] dz \right) [R_T]_k^{-1} \left\{ \begin{array}{c} e_{31} \\ e_{32} \\ 0 \end{array} \right\}_k \phi_k \\ = \quad & \ldots + \sum_{k=1}^{n} \left[\begin{array}{c} I_3 \\ z_{mk}\, I_3 \end{array} \right] [R_T]_k^{-1} \left\{ \begin{array}{c} e_{31} \\ e_{32} \\ 0 \end{array} \right\}_k \phi_k \end{aligned} \tag{2.68}$$

where

$$z_{mk} = \frac{z_{k-1} + z_k}{2} \tag{2.69}$$

is the distance from the mid-plane of layer k to the mid-plane of the composite (Fig.2.8).

The second constitutive equation (2.52), giving the electric displacement for the k^{th} layer, reads in the composite axes (xy)

$$\begin{aligned} D_k &= \left\{ \begin{array}{ccc} e_{31} & e_{32} & 0 \end{array} \right\}_k [R_S]_k \{S\}^{(xy)} - \varepsilon_k \frac{\phi_k}{h_k} \\ &= \left\{ \begin{array}{ccc} e_{31} & e_{32} & 0 \end{array} \right\}_k [R_S]_k \left[\begin{array}{cc} I_3 & z\, I_3 \end{array} \right] \left\{ \begin{array}{c} S_0 \\ \kappa \end{array} \right\} - \varepsilon_k \frac{\phi_k}{h_k} \end{aligned} \tag{2.70}$$

By integrating Equ.(2.70) over the thickness, one gets

$$\int_{z_{k-1}}^{z_k} D_k dz = \int_{z_{k-1}}^{z_k} \left\{ \begin{array}{ccc} e_{31} & e_{32} & 0 \end{array} \right\}_k [R_S]_k \left[\begin{array}{cc} I_3 & z\, I_3 \end{array} \right] \left\{ \begin{array}{c} S_0 \\ \kappa \end{array} \right\} dz - \int_{z_{k-1}}^{z_k} \varepsilon_k \frac{\phi_k}{h_k} dz \tag{2.71}$$

As we assumed D uniform across the thickness, it can be averaged.

$$D_k = \left\{ \begin{array}{ccc} e_{31} & e_{32} & 0 \end{array} \right\}_k [R_S]_k \left[\begin{array}{cc} I_3 & z_{mk}\, I_3 \end{array} \right] \left\{ \begin{array}{c} S_0 \\ \kappa \end{array} \right\} - \frac{\varepsilon_k}{h_k} \phi_k \tag{2.72}$$

In summary, the constitutive equations integrated over the thickness of a multilayered piezoelectric shell (*Kirchhoff* assumption) read:

$$\left\{ \begin{array}{c} N \\ M \end{array} \right\} = \left[\begin{array}{cc} A & B \\ B & D \end{array} \right] \left\{ \begin{array}{c} S_0 \\ \kappa \end{array} \right\} + \sum_{k=1}^{n} \left[\begin{array}{c} I_3 \\ z_{mk}\, I_3 \end{array} \right] [R_T]_k^{-1} \left\{ \begin{array}{c} e_{31} \\ e_{32} \\ 0 \end{array} \right\}_k \phi_k \tag{2.73}$$

$$D_k = \left\{ \begin{array}{ccc} e_{31} & e_{32} & 0 \end{array} \right\}_k [R_S]_k \left[\begin{array}{cc} I_3 & z_{mk}\, I_3 \end{array} \right] \left\{ \begin{array}{c} S_0 \\ \kappa \end{array} \right\} - \frac{\varepsilon_k}{h_k} \phi_k \tag{2.74}$$

In the next chapter, the use of piezoelectric materials for actuation and sensing (mainly laminar design) is discussed. Equation (2.73) is the starting point for the formulation of the equation of a laminar piezoelectric actuator, while Equ.(2.74) is that for a laminar sensor. It is worth noticing that, as we have $[R_T]_k^{-1} = [R_S]_k^T$, the system of equations above is symmetric.

Chapter 3

Actuation and sensing

The use of piezoelectric materials for actuation and sensing has been demonstrated extensively over the years. In a first section, different piezoelectric modes of actuation available are presented. Models neglecting the electromechanical coupling for the particular case of the laminar design are presented in the second section; the duality between actuation and sensing is stressed. Examples of the use of distributed actuation/sensing piezoelectric layers to realize targeted control devices are presented in the last section.

3.1 Piezoelectric modes of actuation

Due to crystal symmetries, piezoelectric coupling matrices have few non-zero elements (See Chap.2). The design of actuation and sensing devices is dictated by the available coupling modes (non-zero elements in the piezoelectric coupling matrix - See typical constitutive equations, of form (2.35), below).

actuation:

$$\left\{\begin{array}{c} S_{11} \\ S_{22} \\ S_{33} \\ 2S_{23} \\ 2S_{13} \\ 2S_{12} \end{array}\right\} = \underbrace{\left[\begin{array}{cccccc} s_{11} & s_{12} & s_{13} & 0 & 0 & 0 \\ s_{12} & s_{22} & s_{23} & 0 & 0 & 0 \\ s_{13} & s_{23} & s_{33} & 0 & 0 & 0 \\ 0 & 0 & 0 & s_{44} & 0 & 0 \\ 0 & 0 & 0 & 0 & s_{55} & 0 \\ 0 & 0 & 0 & 0 & 0 & s_{66} \end{array}\right]}_{\text{compliance}} \left\{\begin{array}{c} T_{11} \\ T_{22} \\ T_{33} \\ T_{23} \\ T_{13} \\ T_{12} \end{array}\right\} + \underbrace{\left[\begin{array}{ccc} 0 & 0 & d_{31} \\ 0 & 0 & d_{32} \\ 0 & 0 & d_{33} \\ 0 & d_{24} & 0 \\ d_{15} & 0 & 0 \\ 0 & 0 & 0 \end{array}\right]}_{\text{coupling}} \left\{\begin{array}{c} E_1 \\ E_2 \\ E_3 \end{array}\right\}$$

sensing:

$$\left\{\begin{array}{c} D_1 \\ D_2 \\ D_3 \end{array}\right\} = \underbrace{\left[\begin{array}{cccccc} 0 & 0 & 0 & 0 & d_{15} & 0 \\ 0 & 0 & 0 & d_{24} & 0 & 0 \\ d_{31} & d_{32} & d_{33} & 0 & 0 & 0 \end{array}\right]}_{\text{coupling}} \left\{\begin{array}{c} T_{11} \\ T_{22} \\ T_{33} \\ T_{23} \\ T_{13} \\ T_{12} \end{array}\right\} + \underbrace{\left[\begin{array}{ccc} \varepsilon_{11} & 0 & 0 \\ 0 & \varepsilon_{22} & 0 \\ 0 & 0 & \varepsilon_{33} \end{array}\right]}_{\text{permittivity}} \left\{\begin{array}{c} E_1 \\ E_2 \\ E_3 \end{array}\right\}$$

The most commonly used piezo materials for actuation and sensing are the piezoceramics (PZT) and the piezopolymers ($PVDF$). The available modes of actuation for a piezoelectric material are determined by its coupling matrix. The coupling matrices of PZT and $PVDF$ look like:

$$[d]_{PZT} = \begin{bmatrix} 0 & 0 & 0 & 0 & d_{15} & 0 \\ 0 & 0 & 0 & d_{15} & 0 & 0 \\ d_{31} & d_{31} & d_{33} & 0 & 0 & 0 \end{bmatrix} \qquad (d_{32} = d_{31},\ d_{24} = d_{15})$$

$$[d]_{PVDF} = \begin{bmatrix} 0 & 0 & 0 & 0 & 0 & 0 \\ 0 & 0 & 0 & 0 & 0 & 0 \\ d_{31} & d_{32} & d_{33} & 0 & 0 & 0 \end{bmatrix}$$

We can therefore anticipate that three main modes of actuation/sensing are available: the in-plane mode (d_{31}, d_{32}), the thickness mode (d_{33}) and the shear mode (d_{15}, d_{24}).

The first two configurations mentioned above are the most commonly used (Fig.3.1). A linear

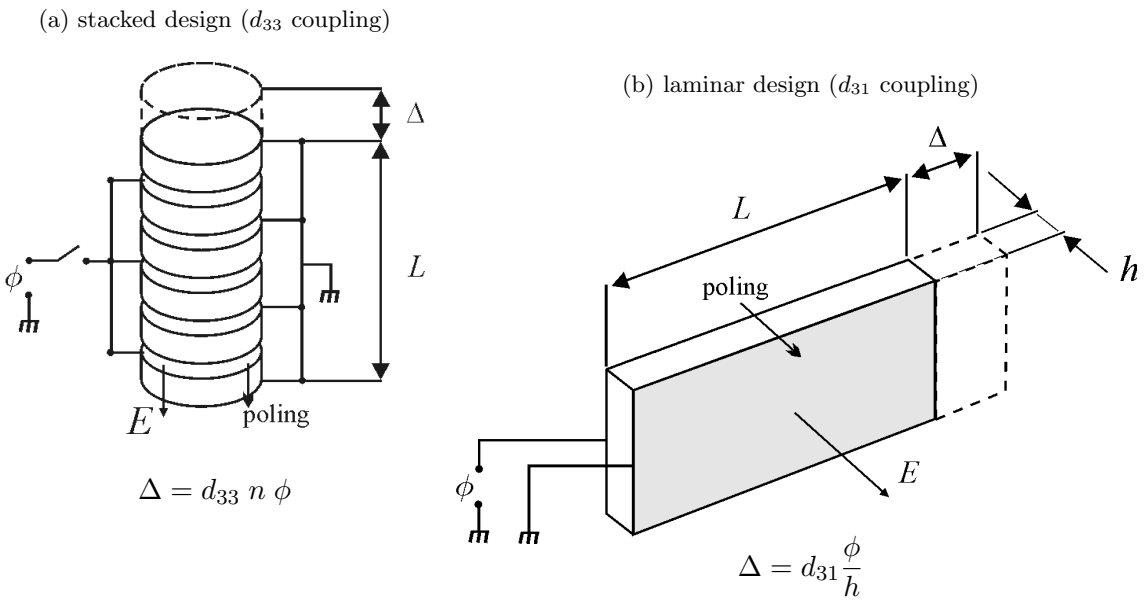

Figure 3.1: Common piezoelectric actuator designs

actuator consists of a stack of thin ceramic disks separated by electrodes. The material is such that the coefficient d_{33} dominates the other piezoelectric constants in the constitutive equations. As a result, the direction of expansion coincides with that of the electric field. The stacked design is often referred to as d_{33} design. When no external load is applied, the change of length is related to the voltage applied by the approximate relationship $\Delta = d_{33}\ n\ \phi$ where n is the number of disks in the stack and ϕ is the applied voltage. This design is mainly used for precision position control.

In the laminar design, centre of interest of this thesis, thin piezoelectric films are bonded on the structure to obtain a bending action. The geometrical arrangement is such that d_{31} (d_{32}) dominates the design and the useful direction of expansion is normal to that of the electric field. The piezoelectric constant d_{31} (d_{32}), however, is only about one half of d_{33} in the stacked design. In the laminar design, the piezoelectric material may consist of ceramics like *lead-zirconate titanate* (*PZT*), generally covered with silver electrodes, or polymers like *polyvinylidene fluoride* (*PVDF* or PVF_2). As mentioned earlier, *PZT* materials are piezo-isotropic in the plane normal to the poling direction ($d_{32} = d_{31}$) while *PVDF* can be strongly anisotropic (See Table 1.1, §1.2.4). As it will be stressed throughout this chapter, it is the shape of the electrodes which determines the effective part of the material. This property is widely used for distributed actuation and sensing.

A third actuator concept is proposed by Benjeddou et al. (1997, 1998): the shear actuation. The proposed configuration is such that, this time, the d_{15} (d_{24}) coupling coefficient dictates the design. The electric field is applied perpendicularly to the poling direction, inducing a transverse shear strain. A shear actuated piezo layer can be included in the core of a sandwich plate as in Fig.3.2. The core should be softer than the faces and thick enough to produce shear stresses.

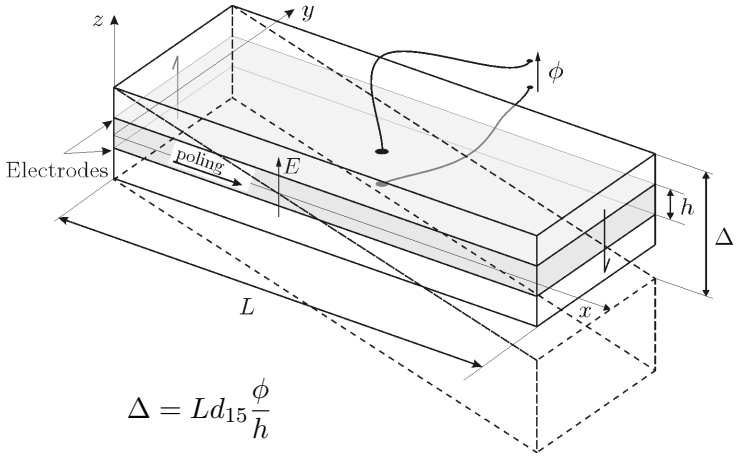

Figure 3.2: Shear actuation

Table 3.1 compares the three types of actuation considering *PZT* piezoceramics and similar dimensions (2 mm thick, 1 cm long) and electrical field (50 kV/m). Two laminar design are considered: standard (Fig.3.1(b)) and bimorph (Fig.3.3). This latter consists in two piezoelectric plates with opposite polarisation stacked together to obtain a bending actuator. A stroke Δ from 1 to 65 μm can be obtained, depending on the chosen design.

Design		Coupling coefficient (*PZT*)			Displacement	Δ
stacked		d_{33}	362	10^{-12} Cb/N	1.81	μm
laminar	standard	d_{31}	-175	10^{-12} Cb/N	0.9	μm
	bimorph				65.63	μm
shear		d_{15}	515	10^{-12} Cb/N	2.58	μm

Table 3.1: Comparison between actuation designs

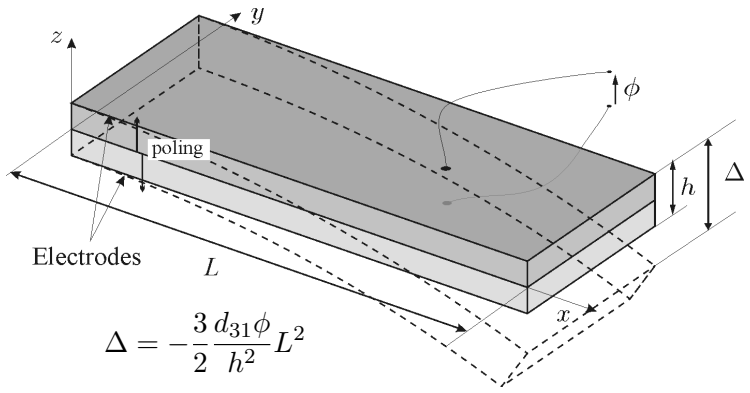

Figure 3.3: Bimorph actuation

3.2 Laminar design modelling

3.2.1 Historical overview

The modelling of piezoelectric material used as laminar actuator or sensor has been addressed by many authors.

Crawley & de Luis (1987) and Crawley & Anderson (1989) proposed an analytical model for segmented piezoelectric actuators. The model consists in a *Bernoulli-Euler* beam with piezoelectric actuators bonded to the surface or embedded in a laminate. A piezoelectric actuator can be replaced by an equivalent localized tensile force and bending moment. The equivalent piezoelectric force and moment equations, so called *equivalent actuator equations*, are developed. An experimental validation with a cantilever beam actuated with a given voltage across the piezoactuator is presented.

Crawley & Lazarus (1991) extended that model to the induced strain actuation of both isotropic and anisotropic plates. Equivalent normal forces and bending moments for piezoactuation of plates are derived using the *Kirchhoff-Love* plate assumptions. A *Ritz* formulation for approximate solutions is developed and applied to sandwich experimental models; aluminium and composite cantilever plates are presented.

Dimitriadis et al. (1991) did a similar work to model bidimensional patches bonded to the surface of a structure, deriving the *equivalent actuator equations* and applied them to the vibration of a rectangular plate for various actuator configurations.

Similarly to the equivalent actuator equations, an equivalent sensor equation can be written taking into account the contributions from extension and curvature of the sensor to the electrical charge appearing on the piezoelectric media. Lee (1990) established the general formulation for an anisotropic piezoelectric laminate using the *Kirchhoff-love* hypothesis. Sensor and actuator equivalent equations are derived, boundary conditions are discussed and the reciprocity between actuation and sensing is pointed out.

Park & Chopra (1996) modelled the piezoactuation of beams in torsion. A one-dimensional beam model is used to determine the coupled extension/bending/torsion response to an applied

voltage across the piezoactuator. It uses the principle of virtual work and takes into account the cross sectional warping. Detailed results are derived for a thin isotropic beam (Bernoulli-Euler) with a surface bonded piezoceramic actuator and compared to experiments.

A simplified approach neglecting the coupling between the equations of electrostatics and elastodynamics is described in the next paragraphs. This theory aims to approximate the behaviour of *active* structures with only a small fraction of laminar piezoelectric material embedded. A pure bending beam model for surface bonded piezoelectric actuator/sensor is first presented; it demonstrates the effect of the shape of the electrodes, which is illustrated in the last section with some examples. Next, a shell model of embedded piezo actuation/sensing taking the membrane strains into account is derived; the importance of membrane coupling is stressed. The duality between actuation and sensing is pointed out throughout the rest of this chapter.

3.2.2 Pure bending beam model

Actuator

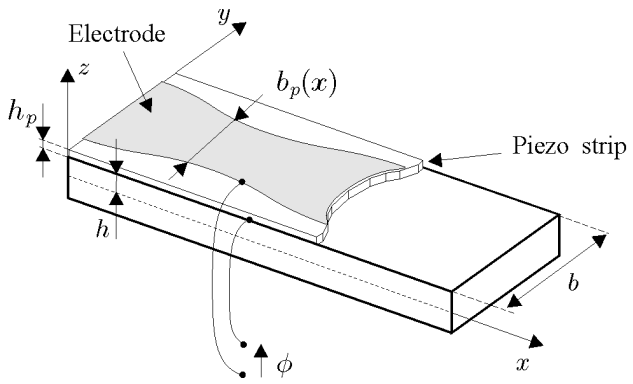

Figure 3.4: Piezoelectric film actuator bonded on a beam structure.

Consider the beam of Fig.3.4 with a thin layer of piezoelectric material bonded on the surface. It is assumed that the thickness of the piezoelectric strip h_p is small compared to that of the beam h. The piezoelectric strip is used as actuator by controlling the voltage ϕ applied to the electrodes, creating a constant electric field $E = \phi/h_p$. It is also assumed that the electrodes have a variable width $b_p(x)$ (this can be achieved either by etching the original surface electrode, or by cutting the piezoelectric layer). Using structural engineering notations, the constitutive equation (2.11) reads, within the piezoelectric layer,

$$\sigma_x = Y_p \epsilon_x - e_{31} \frac{\phi}{h_p} \tag{3.1}$$

Where Y_p is the Young's modulus of the piezoelectric material, e_{31} its piezoelectric constant and h_p, its thickness, over which the voltage ϕ is applied. The following usual relation applies to the beam

$$\sigma_x = Y_b \epsilon_x \tag{3.2}$$

The equation of motion for the beam reads

$$m\ddot{w} = -\frac{\partial^2 M}{\partial x^2} = -M'' \tag{3.3}$$

where M is the bending moment, m the lineic mass density and $w(x)$ is the displacement of the beam in direction z. According to the *Euler-Bernoulli* assumption (*plane sections normal to the neutral axis remain plane and normal to the neutral axis*), the axial deformation and the curvature are related by

$$\epsilon_x = -z\, w'' \tag{3.4}$$

where z is the distance to the neutral axis. Introducing this into Equ.(3.1) and (3.2) and integrating over the cross-section, one gets

$$M = -\int_A \sigma_x z\, dA = YI\, w'' + e_{31}\frac{\phi}{h_p}\, h_p\, b_p(x)\, h \tag{3.5}$$

or

$$M = YI\, w'' + e_{31}\phi\, b_p(x)\, h \tag{3.6}$$

where a constant moment arm h across the thickness of the piezo is assumed. The bending stiffness YI refers to the supporting structure and the piezoelectric film together. Substituting into Equ.(3.3), one gets

$$m\ddot{w} + (YI\, w'')'' = -e_{31}\phi\, b_p''(x)\, h \tag{3.7}$$

It can be seen that when the width of the electrodes varies along the beam, the piezoelectric actuator produces a distributed load proportional to the second derivative of $b_p(x)$. Similarly, for an electrode of constant width, the distributed actuator is equivalent to adding concentrated moments M_p at the boundaries of the actuator (Fig.3.5(a)) while a sudden change in the first derivative $b_p'(x)$ at some location x_0 produces a point force P at the discontinuity (Fig.3.5(b))

From Equ.(3.6), the equivalent piezoelectric moment is given by

$$M_p = -e_{31}\phi\, b_p\, h \tag{3.8}$$

And, by integrating the right hand side of Equ.(3.7) over a small interval about x_0 and taking the limit when the size of the interval goes to zero, the equivalent piezoelectric point force is given by

$$F = -e_{31}\phi\, \left[b_p'(x_0^+) - b_p'(x_0^-)\right] h \tag{3.9}$$

Sensor

The piezoelectric strip is used as sensor by measuring the electric charge appearing on the electrodes. The electrodes are short-circuited so that a zero electric field is enforced ($E = 0$).

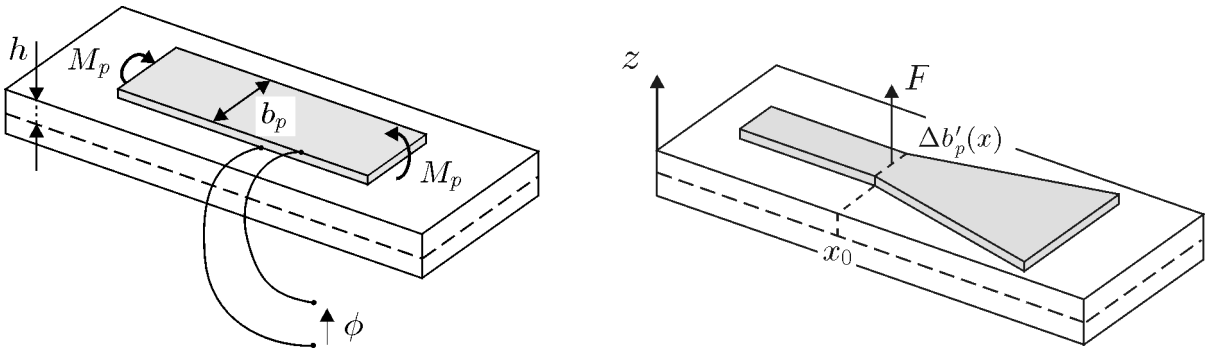

(a) Constant width b_p

(b) Sudden change of the derivative $b'_p(x)$ at x_0

Figure 3.5: Piezoelectric film actuator

According to Equ.(2.12), the amount of charge per unit area is related to the strain by $D = eS$ or, with structural engineering notations,

$$D = e_{31}\epsilon_x \tag{3.10}$$

Combining with Equ.(3.4) and assuming a constant strain over the thickness of the strip, Equ.(3.10) reads

$$D = -e_{31} h\, w'' \tag{3.11}$$

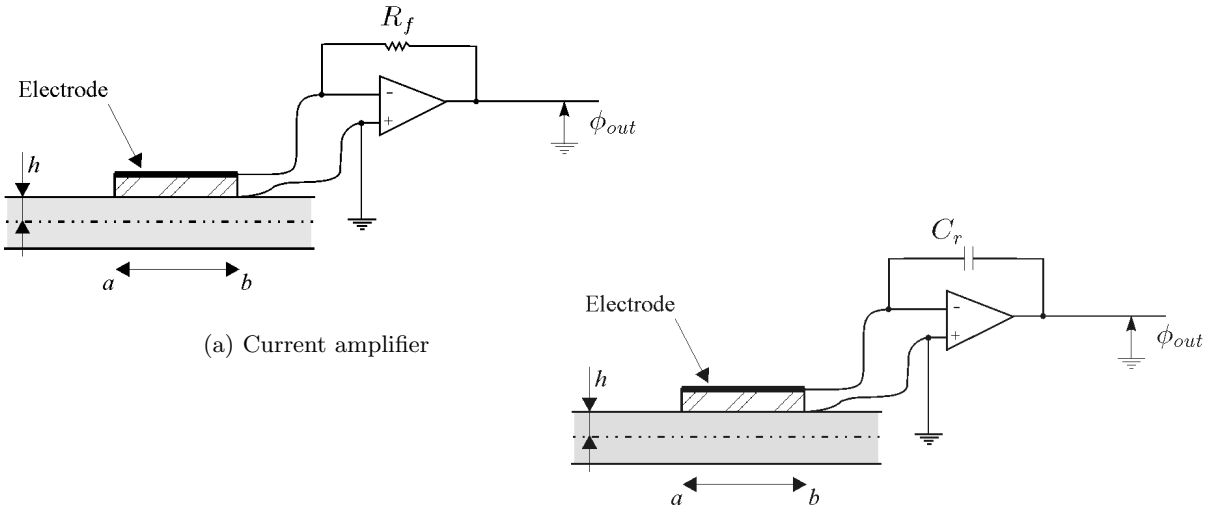

(a) Current amplifier

(b) Charge amplifier

Figure 3.6: Piezoelectric film sensor connections

The corresponding electric charge is equal to the integral of the electric displacement over the

electrode area,

$$Q = \int_a^b D\, b_p(x)\, dx = -h \int_a^b e_{31} w'' b_p(x)\, dx \tag{3.12}$$

The electrodes can be connected either to a charge amplifier or a current amplifier (Fig.3.6). Assuming a uniform polarization profile (e_{31} constant), the output voltage of a current amplifier (Fig.3.6(a)) is given

$$\phi_{out}(t) = -R_f i_s(t) = -R_f \dot{Q} = R_f e_{31} h \int_a^b b_p(x)\, \dot{w}''\, dx \tag{3.13}$$

R_f is the constant of the amplifier. Thus, the output signal is proportional to the integral of the time derivative of the curvature weighted by the width $b_p(x)$ of the electrode.

If a charge amplifier is used instead (Fig.3.6(b)), the output voltage is proportional to the electric charge in the electrode; it is given by

$$\phi_{out}(t) = -\frac{Q}{C_r} = \frac{e_{31} h}{C_r} \int_a^b b_p(x)\, w''\, dx \tag{3.14}$$

C_r is the capacitance of the charge amplifier. If the width of the electrode, b_p, is constant, the output voltage becomes:

$$\phi_{out}(t) = \frac{e_{31} h b_p}{C_r} \big(w'(b) - w'(a)\big) \tag{3.15}$$

The perfect duality between Equ.(3.8) for actuation and (3.15) for sensing should be noted; it is illustrated on Fig.3.7. The reciprocity between actuation and sensing can be summarized as: *a piezoelectric bending actuator can also be used as slope sensor.*

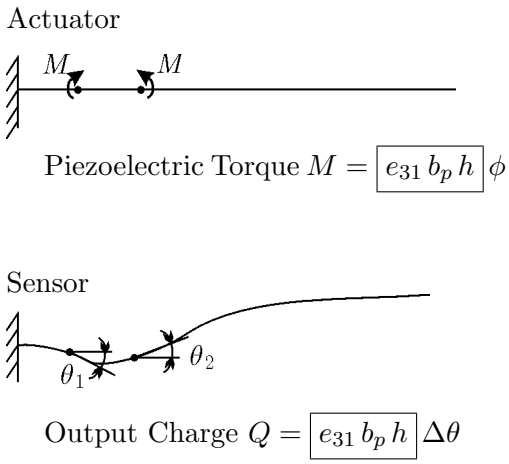

Figure 3.7: Pure bending beam model: actuation/sensing duality

3.2.3 Isotropic shell model

In the previous section, the effect of a piezoelectric strip bonded to a beam when it is used as actuator or sensor has been considered. If the assumptions of the pure bending beam theory become questionable, more elaborate modelling techniques may be required. In general, when the actuator and sensor are close to each other (nearly colocated), the frequency response function becomes more sensitive to the detailed modelling of the coupled system (structure-actuator-sensor) and the transmission path from the actuator to the sensor includes in-plane (membrane) deformations as well as bending ones; the in-plane deformations become relatively more important when the thickness of the structure becomes comparable to that of the strips. For nearly colocated systems, a theory which accounts for the in-plane deformations should be used. (Preumont, 1997; Loix et al., 1998)

Actuation

Assuming the *Kirchhoff* hypothesis for the strain distribution across the thickness, uniform electric field and displacement and a linear piezoelectric behaviour, Equ.(2.73) shows that a voltage ϕ applied between the electrodes of a piezoelectric patch produces equivalent loads and moments:

$$\left\{ \begin{array}{c} N \\ M \end{array} \right\} = - \left[\begin{array}{c} I_3 \\ z_m\, I_3 \end{array} \right] [R_T]^{-1} \left\{ \begin{array}{c} e_{31} \\ e_{32} \\ 0 \end{array} \right\} \phi \tag{3.16}$$

If the piezoelectric properties are isotropic in the plane ($e_{31} = e_{32}$), we have

$$e_{31}\, [R_T]^{-1} \left\{ \begin{array}{c} 1 \\ 1 \\ 0 \end{array} \right\} = e_{31} \left\{ \begin{array}{c} 1 \\ 1 \\ 0 \end{array} \right\} \tag{3.17}$$

Where $[R_T]$ is the transformation matrix given by Equ.(2.56). It follows that

$$\{N\} = \left\{ \begin{array}{c} N_x \\ N_y \\ N_{xy} \end{array} \right\} = -e_{31}\phi \left\{ \begin{array}{c} 1 \\ 1 \\ 0 \end{array} \right\} \tag{3.18}$$

$$\{M\} = \left\{ \begin{array}{c} M_x \\ M_y \\ M_{xy} \end{array} \right\} = -e_{31} z_m \phi \left\{ \begin{array}{c} 1 \\ 1 \\ 0 \end{array} \right\} \tag{3.19}$$

It can be seen that the in-plane forces and the bending moments are both *hydrostatic*; they are independant of the orientation of the facet. It can therefore be concluded that the piezoelectric loads result in a uniform in-plane load N_p and bending moment M_p acting normally to the contour of the electrode as indicated on Fig.3.8.

$$\boxed{N_p = -e_{31}\phi,\ M_p = -e_{31} z_m \phi} \tag{3.20}$$

where z_m is the distance from the mid-plane of the piezoelectric patch to the mid-plane of the plate.

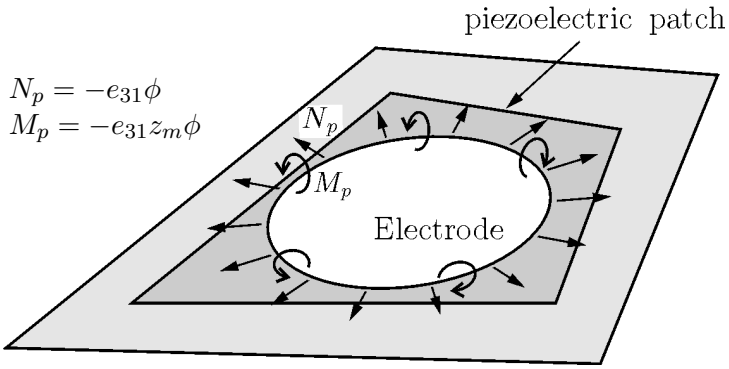

Figure 3.8: Piezoelectric load

Sensing

Consider a piezoelectric patch connected to a charge amplifier as in Fig.3.9. The charge amplifier imposes a zero voltage between the electrodes; the output voltage is proportional to the electric charge, obtained by integrating the electric displacement D over the surface Ω of the electrode.

$$\phi_{out} = -\frac{Q}{C_r} = -\frac{1}{C_r}\int_{\Omega} D\, d\Omega \tag{3.21}$$

Where C_r is the capacitance of the charge amplifier and D is given by Equ.(2.74) in which the voltage is set to zero.

$$D = \left\{ \begin{array}{ccc} e_{31} & e_{32} & 0 \end{array} \right\} [R_S] \left[\begin{array}{cc} I_3 & z_m\, I_3 \end{array} \right] \left\{ \begin{array}{c} S_0 \\ \kappa \end{array} \right\} \tag{3.22}$$

In this equation, $[R_S]$ is the rotation matrix relating the orthotropy axes of the piezo to the global axes (Equ.(2.57)).

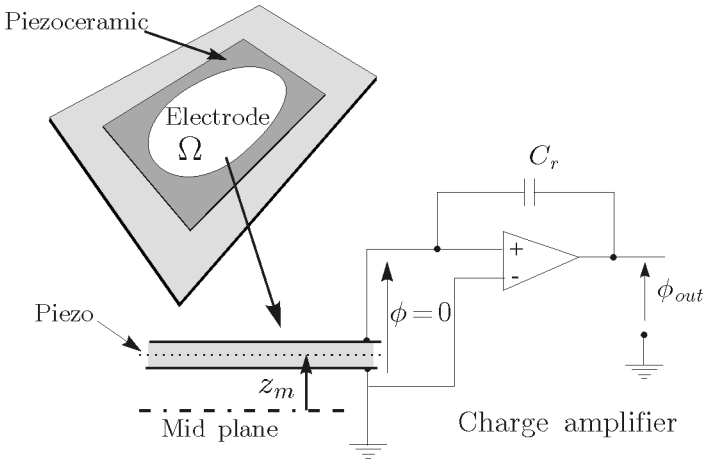

Figure 3.9: Sensor configuration.

If the piezoelectric properties are isotropic in the plane ($e_{31} = e_{32}$), we have

$$e_{31} \left\{ \begin{array}{ccc} 1 & 1 & 0 \end{array} \right\} [R_S] = e_{31} \left\{ \begin{array}{ccc} 1 & 1 & 0 \end{array} \right\} \tag{3.23}$$

Equ.(3.22) becomes

$$D = e_{31} \left(\epsilon_x^0 + \epsilon_y^0 \right) + e_{31} z_m \left(\kappa_x + \kappa_y \right) \tag{3.24}$$

and Equ.(3.21) reads

$$\boxed{\phi_{out} = -\frac{e_{31}}{C_r} \left[\int_\Omega \left(\epsilon_x^0 + \epsilon_y^0 \right) \, d\Omega + z_m \int_\Omega \left(\kappa_x + \kappa_y \right) \, d\Omega \right]} \tag{3.25}$$

The first integral represents the contribution of the average membrane strains over the electrode and the second, the contribution of the average curvature. The integrals extend only over the electrode (the part of the piezo not covered by the electrode does not contribute to the signal). Recalling that (*Kirchhoff* hypothesis)

$$\epsilon_x^0 = \frac{\partial u}{\partial x}, \quad \epsilon_y^0 = \frac{\partial v}{\partial y} \tag{3.26}$$

$$\kappa_x = \frac{\partial^2 w}{\partial x^2}, \quad \kappa_y = \frac{\partial^2 w}{\partial y^2} \tag{3.27}$$

where u, v and w are the mid-plane displacements in direction x, y and z respectively, Equ.(3.25) can be written

$$\phi_{out} = -\frac{e_{31}}{C_r} \left[\int_\Omega \nabla . \mathbf{u^0} \, d\Omega + z_m \int_\Omega \nabla . \nabla (w) \, d\Omega \right] \tag{3.28}$$

where ∇ is the gradient operator and $\mathbf{u^0} \equiv \{u \;\; v\}^T$ is the mid-plane *membrane* displacement vector.

By using the *Green* integral

$$\int_\Omega \nabla . \mathbf{a} \, d\Omega = \int_\mathcal{C} \mathbf{a} . \mathbf{n} \, dl \tag{3.29}$$

the foregoing result can be transformed into

$$\boxed{\phi_{out} = -\frac{e_{31}}{C_r} \left[\int_\mathcal{C} \mathbf{u^0} . \mathbf{n} \, dl + z_m \int_\mathcal{C} \frac{\partial w}{\partial n} \, dl \right]} \tag{3.30}$$

where the integrals extend to the contour of the electrode. The first term is the mid-plane displacement normal to the contour while the second is the slope of the mid-plane normal to the contour (Fig.3.10).

It is worth insisting that for both the actuator and the sensor, it is not the shape of the piezoelectric patch that matters, but rather the shape of the electrodes. The strong reciprocity existing between actuation and sensing relationships (Equ.(3.20) and (3.30)) has been first demonstrated by Lee (1990): *if certain layers of the piezoelectric laminae serve as a particular type of actuator, the laminae can also be used as a sensor of the corresponding type and vice versa*. More precisely, the resulting equivalent load produced by a piezoelectric device used as actuator is conjugated to the dimension measured by the same piezoelectric device used as sensor (e.g. if a bending actuator is used as sensor, the slope or the bending angular velocity can be measured).

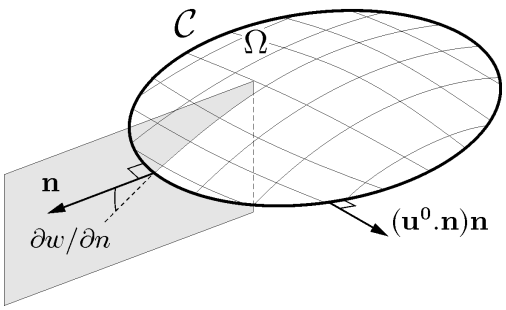

Figure 3.10: Contribution to the output of the piezoelectric isotropic sensor ($e_{31} = e_{32}$)

3.2.4 Why is the beam theory not enough to model colocated systems ?

Comparing the equivalent loads (Equ.(3.20)) of the shell theory with the equivalent bending moment (Equ.(3.8)) of the beam theory, we see that the beam theory accounts only for the component of the bending moment normal to the beam axis and neglects totally the in-plane force (Fig.3.11). Conversely, the sensor signal given by the beam theory accounts only for the component of the rotation along the contour normal to the beam axis.

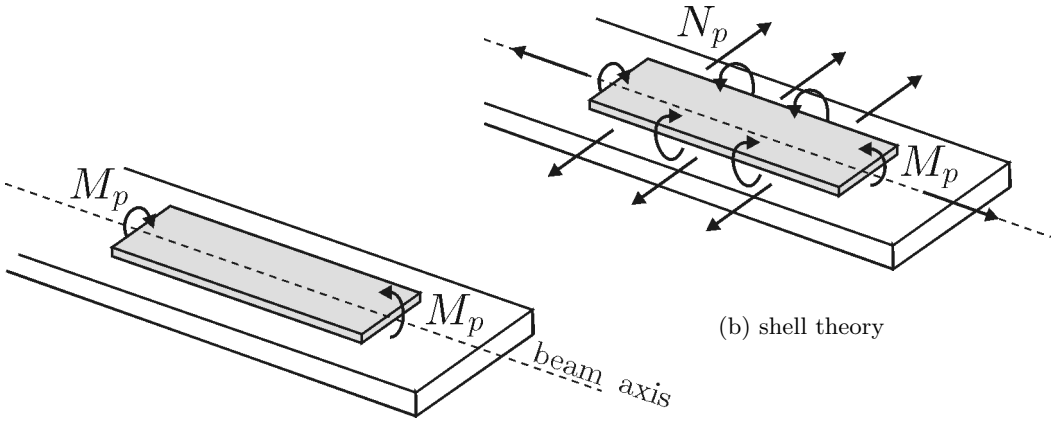

(b) shell theory

(a) beam theory

Figure 3.11: Equivalent piezoelectric loads for a rectangular piezoelectric patch on a beam

Taking the example of an active cantilever beam (Fig.3.12), it turns out that, when the thickness of the beam is small and the actuator and sensor are located on opposite sides of the beam (colocated), the membrane strains contribute significantly to the frequency response function. The discrepancy between the pure bending beam theory and the shell theory becomes large, particularly near the zeros of the frequency response function which are strongly affected by the feedthrough from the strain actuator to the strain sensor (Preumont, 1997, Chap.3).

The simplified approach developed above is well suited for a *classical* finite element implementation (Loix, 1998). The structure (including the piezoelectric components) is modelled with classical finite elements and the piezoelectric loads are regarded as external loads (Equ.(3.20))

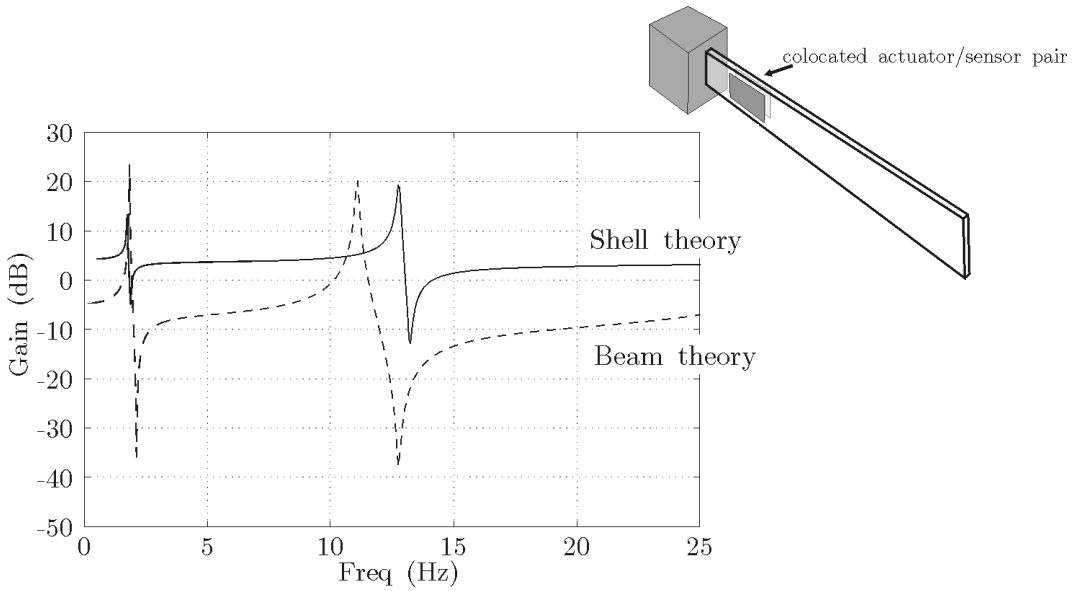

Figure 3.12: Frequency response function of an active cantilever beam with colocated actuator and sensor. Comparison between the beam theory and the shell theory.

and the sensor signal is computed from Equ.(3.25).

However, this approach neglects the coupling between the equations of electrostatics and elastodynamics; it is sufficient if the piezoelectric material represents only a small fraction of the entire structure.

A finite element approach accounting for the piezomechanical coupling is presented in Chap.4 and its implementation into the commercial finite element package *Samcef* is discussed. Some applications are presented in Chap.5.

Next section illustrates the realization of dedicated sensor devices by using distributed piezoelectric elements with shaped electrodes; two examples are considered: modal filtering and acoustic radiation sensing.

3.3 Spatial filters

3.3.1 Modal filters

Discrete point sensors/actuators to control vibrations of flexible structures often suffer from *spillover* (destabilization of flexible modes outside the bandwidth of the controller) leading to instabilities (Preumont, 1997; Loix, 1998). The solution of modal filtering requires heavy real time computation (integration in the space domain). The main idea leading to the concept of inherent modal filtering is that, by simply suitably shaping the distributed actuator/sensor, the spatial integration is embedded into the sensor itself and consequent real time computation can be saved.

Burke & Hubbard Jr (1987) developed a formulation for the control of thin beams subject to most combination of free, clamped, or pinned boundary conditions in which the active elements were spatially varying piezoelectric transducer layers.

Lee et al. (1989, 1991) and Lee & Moon (1990) proposed the use of distributed actuators/sensors to reduce the computational load by taking advantage from the directional properties of piezoelectric materials. By suitably shaping the actuators/sensors, the inherent modal filtering is realized; sensors for mode 1 & 2 of a one-dimensional cantilever plate were constructed by shaping the electrodes to achieve the desired characteristics and tested.

Callahan & Baruh (1996) presented a control law for modal control. Miller et al. (1996a,b, 1998) proposed a selective modal control design methodology by introducing the concept of Selective Modal Transducer (*SMT*). *SMTs* are capable of sensing and exciting any set of vibrational modes in a selectively weighted fashion. The transduction of selected modal subset is accomplished through combining the effects of multiple piezolaminae whose piezoelectric field distribution vary spatially. Simulation results are presented. Some experimental validation (anisotropic *PVDF* layers with different orientations) can be found in (Miller et al., 1997).

Ryou et al. (1998) presented a design method of the electrode shape based on genetic algorithms. The optimization of the electrode pattern to realize the concept of modal transducer for a two-dimensional structure is sought. The electrode pattern is determined by deciding *on* or *off* each electrode tile. The optimization criteria chosen for the actuator design is to minimize the energy in the control mode. The one chosen for the sensor design is the minimization of the *spillover*. The performance of the design is demonstrated by experiments.

The theory lying behind modal filtering by electrode shaping can be illustrated with the pure bending beam model above (*Euler-Bernoulli* assumption) (Lee & Moon, 1990; Loix, 1998).

A beam of length L, covered with piezoelectric material such as depicted on Fig.3.4 is considered; its dynamics follows Equ.(3.7). The transverse displacement w can be decomposed into a weighted sum of its mode shapes (e.g. Preumont, 1997, Chap. 2).

$$w(x,t) = \sum_{k=1}^{\infty} x_k(t)\mathcal{Z}_k(x) \tag{3.31}$$

where $\mathcal{Z}_k(x)$ is the mode shape and $x_k(t)$, the modal amplitude for mode k.

Substituting this expression into Equ.(3.7), assuming there is no rigid body modes and using the following orthogonality properties of the mode shapes

$$\int_0^L m\mathcal{Z}_i(x)\mathcal{Z}_j(x)dx = \mu_i\delta_{ij} \tag{3.32}$$

$$\int_0^L YI\mathcal{Z}_i''(x)\mathcal{Z}_j''(x)dx = \mu_i\omega_i^2\delta_{ij} \tag{3.33}$$

where ω_i are the eigen frequencies, μ_i the modal masses and δ_{ij} is the *Kronecker* index ($\delta_{ij} = 1$ for $i = j$, 0 otherwise), we get the equation for the amplitude of mode k

$$\mu_k(\ddot{x}_k + \omega_k^2 x_k) = -e_{31}\phi \int_0^L \mathcal{Z}_k b_p''(x)dx \tag{3.34}$$

This equation shows that, by shaping the electrode in such a way that

$$b_p''(x) = \mathrm{C}^{\mathrm{st}} m \mathcal{Z}_k(x) \tag{3.35}$$

the authority of the actuator can be limited to the single mode k.

Conversely, the output voltage of a charge amplifier connected to the electrodes (Equ.(3.14)) can be decomposed in the sum of the contribution of each mode.

$$\phi_{out}(t) = -\frac{Q}{C_r} = \frac{e_{31} h}{C_r} \sum_{k=1}^{\infty} \left[\int_0^L b_p(x)\, \mathcal{Z}_k''(x)\, dx \right] x_k(t) \tag{3.36}$$

and, again, by shaping the electrode in such a way that

$$b_p(x) = \mathrm{C}^{\mathrm{st}} Y I \mathcal{Z}_k''(x) \tag{3.37}$$

the sensitivity of the sensor can be limited to the single mode k.

3.3.2 Volume velocity sensor

In recent years, various possibilities have been explored to measure the sound power radiation by structure borne sensors. These are preferable to microphones in vibroacoustic control because they do not introduce time delays in the control loop. It can be shown that, at low frequency, there is a strong correlation between the sound power radiated by a baffled plate and its volume velocity.

$$V_{vol} = \int_\Omega \dot{w} d\Omega \tag{3.38}$$

This allows to replace the sound power sensor by a volume velocity (or displacement) sensor directly mounted on the structure. For a supported plate, the volume sensor can be based on an array of strain sensors.

The QWSIS (Quadratically Weighted Strain Integrating Sensor- Rex & Elliott, 1992) consists of an array of narrow $PVDF$ strips with parabolic shape layed on the surface of the plate (Fig.3.13). It is based on the discretization of the plate sensor into narrow *bands* of width Δ; each strip being considered as a beam covered with piezoelectric material with quadratically shaped electrodes. The parabolic shape performs an inherent spatial integration, reconstructing the volume velocity; the charge signals from all strips are summed to obtain the volume velocity of the entire plate. The piezoelectric material used for the sensor is a highly anisotropic $PVDF$ ($e_{32} \ll e_{31}$).

For a beam, the output signal of a current amplifier (Fig.3.6(a)) connected to an electrode of variable width $b_p(x)$ is proportional to the integral of the time derivative of the curvature weighted by the width (See Equ.(3.13)).

$$\phi_{out}(t) = e_{31} h R_f \int_0^L b_p(x)\, \dot{w}''(x)\, dx \tag{3.39}$$

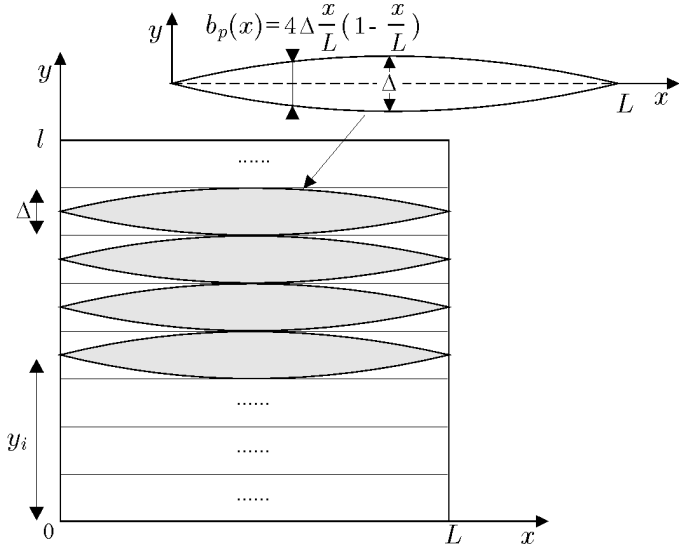

Figure 3.13: QWSIS sensor (Rex & Elliott, 1992)

Considering an electrode of parabolic shape

$$b_p(x) = 4\Delta\frac{x}{L}\left(1-\frac{x}{L}\right) \tag{3.40}$$

and integrating Equ.(3.39) twice, by parts, one gets

$$\phi_{out}(t) = e_{31}hR_f\left[\left[b_p(x)\dot{w}'(x)\right]_0^L + \left[b_p'(x)\dot{w}(x)\right]_0^L + \int_0^L b_p''(x)\,\dot{w}(x)\,dx\right] \tag{3.41}$$

of which the first term vanishes, $b_p(x)$ being zero for $x = 0$ and $x = L$, and the second, the plate being supported ($\dot{w}(x) = 0$ for $x = 0$ and $x = L$).

The second derivative of b_p being the constant $-8\Delta/L^2$, the output signal is directly related to the volume velocity of the beam.

$$\phi_{out}(t) = -8e_{31}R_f\frac{h}{L^2}\Delta\int_0^L \dot{w}(x)\,dx \div V_{vol} \tag{3.42}$$

For the plate, it can be shown that the output signal generated by the sensor is proportional to (Preumont et al., 1999)

$$D = e_{31}\sum_{i=1}^{n}\int_0^L dx\int_{y_i-\frac{\Delta}{2}}^{y_i+\frac{\Delta}{2}}(\frac{\partial^2 w}{\partial x^2}+\chi\frac{\partial^2 w}{\partial y^2})dy \tag{3.43}$$

where n is the number of strips and χ is the piezoelectric anisotropy ratio of the PVDF ($e_{32} = \alpha e_{31}$). It contains an additional term due to the coupling e_{32} in the transverse direction.

Chapter 4

Finite element approach

The study of physical systems frequently results in partial differential equations which either cannot be solved analytically or lack an exact analytic solution due to the complexity of the boundary conditions or domain. For a realistic and detailed study, a numerical method must be used to solve the problem. The finite element method is often found the most adequate.

Over the years, with the development of modern computers, the finite element method has become one of the most important analysis tool in engineering. It has penetrated successfully many areas such as heat transfer, fluid mechanics, electromagnetism, acoustics and fracture mechanics. Finite element packages are now widely available on personal workstations.

Basically, the finite element method (Zienkiewicz, 1971; Reddy, 1984; Hughes, 1987) consists in a piecewise application of classical variational methods to smaller and simpler subdomains called *finite elements* connected to each other in a finite number of points called *nodes*.

The fundamental principles of the finite element method (displacement) are:

The continuum is divided in a finite number of elements of geometrically simple shape

These elements are connected in a finite number of nodes

The unknowns are the displacements of these nodes

Polynomial interpolation functions are chosen to describe the unknown displacement field at each point of the elements related to the corresponding field values at the nodes.

The forces applied to the structure are replaced by an equivalent system of forces applied to the nodes.

As mentioned in Chap.3, the frequency response functions between the inputs and the outputs of a control system involving embedded distributed piezoelectric actuators and sensors in a shell structure are not easy to determine numerically. The situation where they are nearly colocated is particularly critical, because the zeros of the frequency response function are dominated by local effects (See Preumont (1997); Loix et al. (1998) and §3.2.4). These can easily be accounted for by finite elements (Piefort & Henrioulle, 2000).

A finite element formulation accounting for the coupling between the equations of electrostatics and elastodynamics becomes necessary when the piezoelectric material represents a non negligible fraction of the entire structure.

The present chapter is divided in six sections. The first one is an historical overview of the finite element modelling of structures embedding piezoelectric material and, more precisely, laminar piezoelectric designs. In the second section, a variational principle is built starting from the linear piezoelectric constitutive equations presented in Chap.2 and the *Hamilton* principle (generalized *virtual work* principle). A finite element formulation is derived in the third section and the particular case of piezoelectric shells is presented in the next section. The actual implementation in the commercial finite element package *Samcef* is described in the fifth section. The sixth section is devoted to particular electric boundary conditions and how they can be considered in the finite element model. Finally, a method to extract a *state space* model describing the dynamics of a structure embedding piezoelectric actuators and sensors from a finite element analysis is described in the last section.

4.1 History

Following the early work of Eer Nisse (1967) and Tiersten (1967) who have established variational principles for piezoelectric media, the finite element modelling of structures with embedded piezoelectrics has known important developements in recent years. Allik & Hughes (1970) proposed a tetrahedral volumic element accounting for the piezoelectricity. Starting from *Hamilton*'s principle, and the constitutive equations for piezoelectric media, a simple volumic element (tetrahedron) taking into account the piezoelectric coupling is presented. The element has 4 nodes and 4 degrees of freedom per node (3 translations and the electric potential); it uses linear shape functions for both displacement and electrical fields.

Lerch (1990) developed a general formulation accounting for the piezoelectric coupling for two- and three- dimensional finite element modelling of piezoelectric devices. Comparisons between numerical simulation and experiment are presented for the vibration of piezoceramic parallelipipedic bars.

A higher order tetrahedral element is proposed by Moetakef et al. (1995). Interpolation functions of higher order are used; tetrahedron of 10 (linear strain element) and 20 nodes (quadratic strain element) are presented; brick elements are obtained by assembling tetrahedrons using a *Guyan* condensation of the resulting internal nodes to reduce the number of degrees of freedom; these elements are used to model a bimorph pointer (actuation), for which the results are compared to an analytical solution, and a cube under uniform pressure (sensing). An experiment consisting in generating an elastic wave in a cantilever beam is described in Moetakef et al. (1996); results from the model are compared to experimental ones and shown good qualitative agreement.

With the increasing number of shell structures, the need for a finite element modelling tool for plates and shells with embedded distributed piezoelectric actuators and sensors has become more and more evident. Different approach for modelling thin and thick shells have been proposed.

Tzou & Tseng (1990, 1991) derived a thin brick element for distributed dynamic measurement and active vibration control of a rectangular plate; the element consists in a thin solid piezo-

electric brick having 8 structural nodes with 4 degrees of freedom per node (3 translations and the electric potential) and 3 internal nodes (condensed using a *Guyan*'s reduction) to dissipate the excessive shear energy due to the small dimension in the thickness direction. A classic configuration for an *intelligent* structure is composed of a master structure sandwiched between 2 piezoelectric thin layers acting as the distibuted sensor and actuator. Both bonded and embedded piezoelectric sensors and actuators result in a laminate; the multilayer structure is modelled by *stacking* the thin brick elements together and connecting the corresponding nodes. The model is applied to the vibration control of a simply supported square plate. Mode shape and modal voltage distribution are obtained thanks to the model.

Ha et al. (1992) used a similar brick element where the multilayer structure is taken into account; the element matrices are integrated over the thickness of each layer and summed. That element is used to model the cantilever plate described in (Crawley & Lazarus, 1991) (static case), to determine the step-response of a cantilever beam and to design the active damping of the first mode of sensor/actuator composite cantilever plate. The results are compared to the results found in (Crawley & Lazarus, 1991) and shown good agreement with experiments.

Rao & Sunar (1993) established a finite element formulation of thermopiezoelectric problems starting from the linear thermopiezoelectric constitutive equations established by Mindlin (1974) and the *Hamilton*'s principle. In (Sunar & Rao, 1996, 1997), they used the quasistatic equations of thermopiezoelectricity to develop heat, sensor and actuator equations; a finite element formulation is presented. A distributed control system consisting in a cantilever beam sandwiched between a piezoelectric sensor/actuator pair is used to evaluate the proposed finite element approach on the static and dynamic behaviour.

Tzou & Ye (1996) derived a 12-nodes triangular thin solid plane element with 4 degrees of freedom per node; it uses shape functions quadratic in the two in-plane directions and linear in the transverse direction with the assumption of a layerwise constant shear angle (*Mindlin* hypothesis). A laminate is composed of laminae which could be either elastic material or piezoelectric material; the laminated structure is obtained by stacking elements together and connecting the corresponding nodes; this element is validated by modelling the actuation of a bimorph pointer. To stress the influence of the piezoelectric coupling on the vibration characteristics, a semi-circular ring shell has been modelled using 60 triangular shell elements (20 for each layer and 10 element meshes along the length); the evolution of its eigenfrequencies with a growing number of short-circuited electrodes is examined. The number of short-circuited electrodes varies from 1 to 10 (fully short-circuited). This element has been extended later by Köppe et al. (1998) to isoparametric curved triangular and quadrangular elements with shape functions of different polynomial degree for each layer; the model is applied to a rectangular plate of composite material with surface bonded piezo patches under static voltage load, simply supported on two edges.

The modelling of shells using solid elements results in an excessive shear strain energy in the thickness direction. By reducing one dimension compared to the others, the transverse shear stiffness term becomes excessively important (linked to the linear interpolation of the strain) leading to what is usually called the shear locking phenomenon. A commonly used solution to overcome this difficulty consists in adding internal degrees of freedom resulting in large problem size requiring techniques such as the *Guyan*'s reduction (also known as *static condensation*) to reduce the number of degrees of freedom.

Lee & Saravanos (1996) derived a thermopiezoelectric multilayer beam element; it uses shape functions linear along the beam and linear through the thickness of each layer (layerwise linear). A reduced integration scheme for the transverse shear stiffness is used; the element takes into account the effect of constant thermal load (constant gradient of temperature); A cantilever beam under thermal load is modelled. Heyliger et al. (1996) extended the layerwise linear formulation to a piezoelectric shell element and applied it to static and dynamic modelling of a simply supported plate and a cylindrical shell. Later, Saravanos (1997) presented a multilayer piezoelectric thin plate using the *Kirchhoff-Love* assumption (linear displacement field through the thickness) and bilinear shape functions; it has 1 electrical degree of freedom per piezoelectric layer per node, assuming a constant electric field through the thickness for each layer (layerwise linear transverse shape function for the electric potential). That shell element has been applied to the modelling of a simply supported plate and shown good agreement with exact solutions for moderately thin plates ($a/h \approx 50$), an actuated cylindrical panel to study the effect of the actuator placement through the thickness which exactly matches a *Ritz* solution and a cantilever cylindrical shell to show the effect on actuation and sensing of the difference between continuous and discontinuous transducers (4 across the length) and the effect of the curvature on the tip displacement and sensing. It was later used to evaluate the passive damping of piezoelectric shells with integrated electrical network and compared with experiments (Saravanos, 2000).

A pure bending (*Kirchhoff* assumption) plane rectangular plate element is proposed in (Hwang & Park, 1993); the main idea is the use of a multilayered plate element with a single electrical degree of freedom per piezoelectric layer, the voltage across the thickness of the layer, uniform on the element surface. This multilayer element has 4 nodes with 3 degrees of freedom per node (1 translation and 2 rotations) and 1 electrical degree of freedom for each piezoelectric layer (voltage across the layer). This element neglects the transverse shear and is therefore not suitable to model thick shells; it does not account for the extension, modelling only the bending behaviour. The bimorph pointer is modelled numerically and the results were compared to an analytical solution and shown a good agreement. Chen et al. (1997) used an isoparametric pure bending element to model a bimorph beam and for vibration control design.

Samanta et al. (1996) used a cubic displacement field with a 8 node quadratic rectangular multilayer plate with 2 electrical degrees of freedom (constant voltage over the element across the only two piezoelectric outer layer) and 11 mechanical degrees of freedom per node (3 translations, 3 slopes and 5 higher order rotations). A simply supported plate is modelled; the fundamental natural frequencies and forced response were computed and shown good agreement with *exact* solutions.

Suleman & Venkayya (1995a) and Suleman & Gonçalvès (1995) proposed a 4 node plate element using bilinear shape functions and the *Mindlin* assumption (constant shear angle) to accomodate thick as well as thin shells; each node has 5 degrees of freedom (3 translations and 2 rotations), the element has one additional electrical degree of freedom per piezoelectric layer (voltage across the thickness). It uses a reduced integration scheme for the transverse shear stiffness to avoid the transverse shear locking phenomenon. This element is demonstrated using the plate described by Crawley & Lazarus (1991), a bimorph pointer and panel flutter control; comparison with the work of Ha et al. (1992) is made.

Chattopadhyay et al. (1999) developed a quasi-static coupled thermopiezoelectric model for a smart composite plate structure with surface bonded piezoelectric materials using a variational

approach; linear piezoelectricity is assumed, a higher order transverse shear strain distribution is used (third order). A simply supported unidirectional graphite/epoxy laminate plate is modelled; the influence of transverse shear and couplings are discussed. A shell finite element formulation was derived (Zhou et al., 2000) with the same transverse shear strain distribution and a higher order thermal field. A rectangular fiber-reinforced laminated plate with surface bonded *piezoelectric* patches is modelled; the influence of the couplings on the dynamics of piezo- and thermo- actuated structures is discussed.

When the thickness becomes small, the behaviour of the elements accounting for the transverse shear strain (e.g. *Mindlin* elements) is driven by transverse shear stiffness while the transverse shear strain should be negligible. This also leads to the shear locking phenomenon. Solutions to overcome this problem can be to use a reduced integration scheme for the transverse shear stiffness (Suleman & Venkayya, 1995b; Hong & Chopra, 1999) or to use different interpolation functions for the transverse shear strain. The latter is the solution adopted by the element used in the present study: *Mindlin* shell element from the commercial finite element package *Samcef* (*Samtech s.a.*).

4.2 Variational principle

The piezoelectric constitutive equations can be written under the form (2.34)

$$\{T\} = [c^E]\{S\} - [e]^T\{E\} \tag{4.1}$$
$$\{D\} = [e]\{S\} + [\varepsilon^S]\{E\} \tag{4.2}$$

where $\{T\}$ represents the stress vector, $\{S\}$, the strain vector, $\{E\}$, the electric field, $\{D\}$, the electric displacement, $[c^E]$, the elastic coefficients at constant $\{E\}$, $[\varepsilon^S]$, the dielectric coefficients at constant $\{S\}$, and $[e]$, the piezoelectric coupling coefficients

The dynamic equations of a piezoelectric continuum can be derived from the *Hamilton* principle, in which the Lagrangian and the virtual work are properly adapted to include the electrical contributions as well as the mechanical ones (Allik & Hughes, 1970; Lerch, 1990; Tzou & Tseng, 1990). The potential energy density of a piezoelectric material includes contributions from the strain energy and from the electrostatic energy (Tiersten, 1967).

The dynamic equations of a piezoelectric continuum can be derived using *Hamilton*'s principle:

$$\delta \int_{t_1}^{t_2} (\mathcal{L} + \mathcal{W}) dt = 0 \tag{4.3}$$

where t_1 and t_2 define the time interval (all variations must vanish at $t = t_1$ and $t = t_2$), $\mathcal{L}$ is the Lagrangian and $\mathcal{W}$ is the virtual work of external mechanical and electrical forces.

The Lagrangian $\mathcal{L}$ is defined by the sum of kinetic energy J and electrical enthalpy H (linear piezoelectricity) (The *Gibbs* free energy $G = H - \Theta\varsigma$ -Equ.(2.17)- would have been used to also take into account the pyroelectric coupling - see §2.2.2). The electrical enthalpy density H is defined by

$$H = U - E_i D_i \tag{4.4}$$

The conservation of energy for the linear piezoelectric continuum results in the first law of thermodynamics (Equ.(2.13)):

$$dU = T_{ij}dS_{ij} + E_i dD_i \tag{4.5}$$

from equations (4.5) and (4.4), there results

$$dH = T_{ij}dS_{ij} - D_i dE_i \tag{4.6}$$

and thus

$$T_{ij} = \frac{\partial H}{\partial S_{ij}} \tag{4.7}$$

$$D_i = -\frac{\partial H}{\partial E_i} \tag{4.8}$$

In linear piezoelectric theory, the form taken by H is (IEEE std)

$$H = \frac{1}{2}c^E_{ijkl}S_{ij}S_{kl} - e_{kij}E_k S_{ij} - \frac{1}{2}\varepsilon^S_{ij}E_i E_j \tag{4.9}$$

where c_{ijkl}, e_{kij} and ε_{ij} are respectively the elastic, the piezoelectric and the dielectric constants.

$$J = \frac{1}{2}\rho\{\dot{u}\}^T\{\dot{u}\} \tag{4.10}$$

$$H = \frac{1}{2}\left[\{S\}^T\{T\} - \{E\}^T\{D\}\right] \tag{4.11}$$

$$\mathcal{L} = \int_V (J - H)dV = \int_V \left[\frac{1}{2}\rho\{\dot{u}\}^T\{\dot{u}\} - \frac{1}{2}\left[\{S\}^T\{T\} - \{E\}^T\{D\}\right]\right] dV \tag{4.12}$$

where $\{\dot{u}\}$ is the velocity field.

The *essential* boundary conditions are: prescribed displacement field on Ω_3 ($\{u\} = \{\underline{u}\}$) and electric potential on Ω_4 ($\phi = \underline{\phi}$).

The virtual work done by the external mechanical forces and the applied electric charges for an arbitrary variation of the displacement field $\{\delta u\}$ and of the electrical potential $\delta\phi$ both compatible with the *essential* boundary conditions (i.e. $\{\delta u\} = \{0\}$ on Ω_3 and $\delta\phi = 0$ on Ω_4) is

$$\delta\mathcal{W} = \int_V \{\delta u\}^T\{F_V\}dV + \int_{\Omega_1} \{\delta u\}^T\{F_\Omega\}d\Omega + \{\delta u\}^T\{F_P\} - \int_{\Omega_2} \delta\phi\ \varrho\ d\Omega - \delta\phi\ Q \tag{4.13}$$

where $\{F_V\}$, are the body applied forces, $\{F_\Omega\}$, the surface applied forces (defined on Ω_1), $\{F_P\}$, the point loads, ϕ, the electric potential, ϱ, the surface charge brought on Ω_2, Q, the applied concentrated electric charges, and ρ, the mass density.

From Equ.(4.11) and (4.13), the analogy between electrical and mechanical variables can be deduced (Table 4.1). The electrical tensors are one degree lower than the corresponding mechanical ones.

Mechanical		Electrical	
Force	$\{F\}$	ϱ	Charge
Displacement	$\{u\}$	ϕ	Voltage
Stress	$[T]$	$\{D\}$	Electric Displacement
Strain	$[S]$	$\{E\}$	Electric Field

Table 4.1: Electromechanical analogy

Integrating the variation of kinetic energy term $\rho\{\dot{\delta u}\}^T\{\dot{u}\}$ by part over the time interval, one gets

$$\int_{t_1}^{t_2} \rho\{\dot{\delta u}\}^T\{\dot{u}\}dt = \left[\rho\{\delta u\}^T\{\dot{u}\}\right]_{t_1}^{t_2} - \int_{t_1}^{t_2} \rho\{\delta u\}^T\{\ddot{u}\}dt \tag{4.14}$$

of which the first term vanishes, $\{\delta u\}$ being equal to zero in $t = t_1$ and $t = t_2$.

Taking into account the constitutive equations (4.1) and (4.2) and substituting the Lagrangian and virtual work into Hamilton's principle (4.3) yields

$$\begin{aligned} 0 \;=\; & -\int_V \left[\rho\{\delta u\}^T\{\ddot{u}\} - \{\delta S\}^T[c^E]\{S\} + \{\delta S\}^T[e]^T\{E\} + \{\delta E\}^T[e]\{S\}\right. \\ & \left. + \{\delta E\}^T[\varepsilon^S]\{E\} + \{\delta u\}^T\{F_V\}\right] dV + \int_{\Omega_1} \{\delta u\}^T\{F_\Omega\}d\Omega \\ & + \{\delta u\}^T\{F_P\} - \int_{\Omega_2} \delta\phi\ \varrho\ d\Omega - \delta\phi\ Q \end{aligned} \tag{4.15}$$

4.3 Finite element formulation

The displacement field $\{u\}$ and the electric potential ϕ over an element are related to the corresponding node values $\{u_i\}$ and $\{\phi_i\}$ by the mean of the shape functions $[\mathcal{N}_u]$, $[\mathcal{N}_\phi]$

$$\{u\} = [\mathcal{N}_u]\{u_i\} \tag{4.16}$$
$$\phi = [\mathcal{N}_\phi]\{\phi_i\} \tag{4.17}$$

And therefore, the strain field $\{S\}$ and the electric field $\{E\}$ are related to the nodal displacements and potential by the shape functions derivatives $[\mathcal{B}_u]$ and $[\mathcal{B}_\phi]$ defined by

$$\{S\} = [\mathcal{D}][\mathcal{N}_u]\{u_i\} = [\mathcal{B}_u]\{u_i\} \tag{4.18}$$
$$\{E\} = -\nabla[\mathcal{N}_\phi]\{\phi_i\} = -[\mathcal{B}_\phi]\{\phi_i\} \tag{4.19}$$

where ∇ is the gradient operator and $[\mathcal{D}]$ is the derivation operator defined such as $\{S\} = [\mathcal{D}]\{u\}$

$$[\mathcal{D}] = \begin{bmatrix} \partial_x & 0 & 0 \\ 0 & \partial_y & 0 \\ 0 & 0 & \partial_z \\ 0 & \partial_z & \partial_y \\ \partial_z & 0 & \partial_x \\ \partial_y & \partial_x & 0 \end{bmatrix} \tag{4.20}$$

Substituting expressions (4.16) to (4.20) into the variational principle (4.15) yields

$$\begin{aligned}
0 = &- \{\delta u_i\}^T \int_V \rho[\mathcal{N}_u]^T[\mathcal{N}_u]dV\{\ddot{u}_i\} &- \{\delta u_i\}^T \int_V [\mathcal{B}_u]^T[c^E][\mathcal{B}_u]dV\{u_i\} \\
&- \{\delta u_i\}^T \int_V [\mathcal{B}_u]^T[e][\mathcal{B}_\phi]dV\{\phi_i\} &- \{\delta \phi_i\}^T \int_V [\mathcal{B}_\phi]^T[e]^T[\mathcal{B}_u]dV\{u_i\} \\
&+ \{\delta \phi_i\}^T \int_V [\mathcal{B}_\phi]^T[\varepsilon^S][\mathcal{B}_\phi]dV\{\phi_i\} &+ \{\delta u_i\}^T \int_V [\mathcal{N}_u]^T\{F_V\}dV \\
&+ \{\delta u_i\}^T \int_{\Omega_1} [\mathcal{N}_u]^T\{F_\Omega\}d\Omega &+ \{\delta u_i\}^T[\mathcal{N}_u]^T\{F_P\} \\
&- \{\delta \phi_i\}^T \int_{\Omega_2} [\mathcal{N}_\phi]^T\varrho d\Omega &- \{\delta \phi_i\}^T[\mathcal{N}_\phi]^T Q
\end{aligned} \tag{4.21}$$

which must be verified for any arbitrary variation of the displacements $\{\delta u_i\}$ and electrical potentials $\{\delta \phi_i\}$ compatible with the *essential* boundary conditions.

For an element, Equ.(4.21) can be written under the form

$$[\mathcal{M}]\{\ddot{u}_i\} + [K_{uu}]\{u_i\} + [K_{u\phi}]\{\phi_i\} = \{f_i\} \tag{4.22}$$

$$[K_{\phi u}]\{u_i\} + [K_{\phi\phi}]\{\phi_i\} = \{g_i\} \tag{4.23}$$

with

$$[\mathcal{M}] = \int_V \rho[\mathcal{N}_u]^T[\mathcal{N}_u]dV \tag{4.24}$$

$$[K_{uu}] = \int_V [\mathcal{B}_u]^T[c^E][\mathcal{B}_u]dV \tag{4.25}$$

$$[K_{u\phi}] = \int_V [\mathcal{B}_u]^T[e]^T[\mathcal{B}_\phi]dV \tag{4.26}$$

$$[K_{\phi\phi}] = -\int_V [\mathcal{B}_\phi]^T[\varepsilon][\mathcal{B}_\phi]dV \tag{4.27}$$

$$[K_{\phi u}] = [K_{u\phi}]^T \tag{4.28}$$

respectively the element mass, stiffness, piezoelectric coupling and capacitance matrix and

$$\{f_i\} = \int_V [\mathcal{N}_u]^T\{P_b\}dV + \int_{\Omega_1} [\mathcal{N}_u]^T\{P_S\}d\Omega + [\mathcal{N}_u]^T\{P_c\} \tag{4.29}$$

$$\{g_i\} = -\int_{\Omega_2} [\mathcal{N}_\phi]^T\varrho d\Omega - [\mathcal{N}_\phi]^T Q \tag{4.30}$$

the external mechanical force and electric charge.

Each element k of the mesh is connected to its neighbouring elements at the global nodes and the displacement is continuous from one element to the next. The element degrees of freedom (*dof*) ($\{u_i\}^{(k)}$, $\{\phi_i\}^{(k)}$) are related to the global *dof* ($\{U\}$, $\{\Phi\}$) by the mean of the localization matrices $[L_u]^{(k)}$ and $[L_\phi]^{(k)}$:

$$\{u_i\}^{(k)} = [L_u]^{(k)}\{U\} \tag{4.31}$$

$$\{\phi_i\}^{(k)} = [L_\phi]^{(k)}\{\Phi\} \tag{4.32}$$

The element ij of $[L_u]^{(k)}$ is equal to 1 if the i^{th} mechanical *dof* of the finite element k corresponds to the j^{th} global *dof* and is zero otherwise. The element ij of $[L_\phi]^{(k)}$ is equal to 1 if the i^{th} electric *dof* of the finite element k is connected to the j^{th} global electric *dof* and is zero otherwise.

The Hamilton's principle (4.3) must be verified for the whole structure, which results in (by summation of the contribution from each finite element):

$$\begin{aligned} 0 = \quad \{\delta U\}^T \Big[\Big(\sum\nolimits_k [L_u]^{(k)^T} [\mathcal{M}]^{(k)} [L_u]^{(k)} \Big) \{\ddot{U}\} \quad + \Big(\sum\nolimits_k [L_u]^{(k)^T} [K_{uu}]^{(k)} [L_u]^{(k)} \Big) \{U\} \\ + \Big(\sum\nolimits_k [L_u]^{(k)^T} [K_{u\phi}]^{(k)} [L_\phi]^{(k)} \Big) \{\Phi\} - \sum\nolimits_k [L_u]^{(k)^T} [f_k] \Big] \\ + \{\delta\Phi\}^T \Big[\Big(\sum\nolimits_k [L_\phi]^{(k)^T} [K_{\phi u}]^{(k)} [L_u]^{(k)} \Big) \{U\} \quad + \Big(\sum\nolimits_k [L_\phi]^{(k)^T} [K_{\phi\phi}]^{(k)} [L_\phi]^{(k)} \Big) \{\Phi\} \\ - \sum\nolimits_k [L_\phi]^{(k)^T} [g_k] \Big] \end{aligned} \tag{4.33}$$

again for any arbitrary variation of the displacements $\{\delta U\}$ and electrical potentials $\{\delta\Phi\}$ verifying the *essential* boundary conditions.

Equ.(4.33) can be written under the form

$$\boxed{\begin{aligned} [\mathcal{M}]\{\ddot{U}\} + [K_{UU}]\{U\} + [K_{U\Phi}]\{\Phi\} &= \{F\} \\ [K_{\Phi U}]\{U\} + [K_{\Phi\Phi}]\{\Phi\} &= \{G\} \end{aligned}} \begin{matrix} (4.34) \\ (4.35) \end{matrix}$$

where the assembled matrices are given by:

$$[\mathcal{M}] = \sum\nolimits_i [L_{ui}]^T \left[\mathcal{M}^{(i)}\right] [L_{ui}] \tag{4.36}$$

$$[K_{UU}] = \sum\nolimits_i [L_{ui}]^T \left[K_{uu}^{(i)}\right] [L_{ui}] \tag{4.37}$$

$$[K_{U\Phi}] = \sum\nolimits_i [L_{ui}]^T \left[K_{u\phi}^{(i)}\right] [L_{\phi i}] \tag{4.38}$$

$$[K_{\Phi U}] = \sum\nolimits_i [L_{\phi i}]^T \left[K_{\phi u}^{(i)}\right] [L_{ui}] \tag{4.39}$$

$$[K_{\Phi\Phi}] = \sum\nolimits_i [L_{\phi i}]^T \left[K_{\phi\phi}^{(i)}\right] [L_{\phi i}] \tag{4.40}$$

$$\{F\} = \sum\nolimits_i [L_{ui}]^T [f_i] \tag{4.41}$$

$$\{G\} = \sum\nolimits_i [L_{\phi i}]^T [g_i] \tag{4.42}$$

Equ.(4.34) and (4.35) couple the mechanical variables $\{U\}$ and the electrical potentials $\{\Phi\}$; $\{F\}$ represents the external forces applied to the structure and $\{G\}$ the electric charges brought to the electrodes.

4.4 *Kirchhoff* element

It is assumed that the electric field and displacement are uniform across the thickness and aligned with the poling direction on the normal to the mid-plane. The electrical degrees of freedom are

the voltages ϕ_k across the piezoelectric layers; it is assumed that the potential is constant over each element (this implies that the finite element mesh follows the shape of the electrodes). One electrical *dof* per piezoelectric layer is defined.

From these assumptions, it can be concluded that, over an element

$$\{\phi\} = \{\phi_k\} \tag{4.43}$$

$$\{E\} = -\left\{\frac{\phi_k}{h_k}\right\} \tag{4.44}$$

where h_k is the thickness of layer k, involving that $[\mathcal{N}_\phi] = I$ and $[\mathcal{B}_\phi] = \text{diag}(1/h_k)$.

Starting from the constitutive equations for a *Kirchhoff* piezoelectric shell (Equ.(2.73) and (2.74)), the element mass, stiffness, coupling and piezoelectric capacitance matrices as defined by Equ.(4.24) to (4.27) read ($[\mathcal{N}]$ and $[\mathcal{B}]$ are used for $[\mathcal{N}_u]$ and $[\mathcal{B}_u]$ respectively).

$$[\mathcal{M}] = \int_\Omega m[\mathcal{N}]^T[\mathcal{N}]d\Omega \tag{4.45}$$

$$[K_{uu}] = \int_\Omega [\mathcal{B}]^T \begin{bmatrix} A & B \\ B & D \end{bmatrix} [\mathcal{B}]d\Omega \tag{4.46}$$

$$[K_{u\phi}] = \int_\Omega [\mathcal{B}]^T \begin{bmatrix} \cdots & \mathcal{E}_k^T & \cdots \\ \cdots & \mathcal{E}_k^T z_{mk} & \cdots \end{bmatrix} d\Omega \tag{4.47}$$

$$[K_{\phi\phi}] = -\Omega \begin{bmatrix} \ddots & & 0 \\ & \varepsilon_k/h_k & \\ 0 & & \ddots \end{bmatrix} \tag{4.48}$$

$$[K_{\phi u}] = [K_{u\phi}]^T \tag{4.49}$$

with m is the surfacic mass density.

We have introduced

$$\{\mathcal{E}\}_k = \begin{Bmatrix} e_{31} & e_{32} & 0 \end{Bmatrix}_k [R_S]_k \tag{4.50}$$

and we have used the fact that

$$[R_T]_k^{-1} \begin{Bmatrix} e_{31} & e_{32} & 0 \end{Bmatrix}_k^T = \{\mathcal{E}\}_k^T \tag{4.51}$$

The external applied mechanical forces and the electric charges brought to the electrodes of the system read

$$\{f\} = \int_\Omega [\mathcal{N}]^T \{P_S\}d\Omega + \{P_c\} \tag{4.52}$$

$$\{g\} = -\begin{Bmatrix} \cdots & \varrho_k & \cdots \end{Bmatrix}^T \tag{4.53}$$

where $[P_S]$ and $[P_c]$ are respectively the external distributed forces and concentrated forces and ϱ_k the external charges brought to the electrodes.

4.5 *Mindlin* element

The classical *Kirchhoff* theory neglects the transverse shear strains. Alternative theories which accomodate the transverse shear strains have been developed and have been found more accurate for thick shells (Hughes, 1987).

We consider a shell structure with embedded piezoelectric patches covered with electrodes. The poling direction and the electric and displacement fields direction are parallel, normal to the patches. The piezoelectric patches are parallel to the mid-plane and orthotropic in their plane.

The following hypothesis are made (See also Appendix A):

- **One dimension is significantly less than the others**
- **Plane stress hypothesis:** $\sigma_{zz} = 0$, using classical engineering notations
- ***Mindlin* assumption:** a fiber normal to the mid-plane remains straight but no longer orthogonal to the mid-plane; a transverse shear strain $\{\gamma\}$ is introduced, constant through the thickness and equal to the angle difference between the normal to the mi-plane and the material fiber.

$$\{S\} = \{S_0\} + z\,\{\kappa\} \tag{4.54}$$

$$\{\gamma\} = \{\beta\} + \nabla w \tag{4.55}$$

  where $\{S_0\}$ is the mid plane strain, $\{\kappa\}$ the actual curvature (spatial derivatives of the fiber rotation angles $\{\beta\}$), w is the transverse mid-plane displacement and ∇ is the gradient operator (∇w is the mid-plane slope). The *in-plane* strain and stress vectors written in axes (xy) are given in classical engineering notation respectively by $\{S\} = \{\epsilon_x\ \epsilon_y\ \gamma_{xy}\}^T$ and $\{T\} = \{\sigma_x\ \sigma_y\ \tau_{xy}\}^T$ and the transverse shear strain and stress vectors by $\{\gamma\} = \{\gamma_{yz}\ \gamma_{xz}\}^T$ and $\{\tau\} = \{\tau_{yz}\ \tau_{xz}\}^T$.

- **There is no coupling between extension/bending and transverse shear**
- **Uniform electric field and displacement** across the thickness and aligned on the normal to the mid-plane (direction 3).

$$\{E\} = \left\{ \begin{array}{c} 0 \\ 0 \\ E \end{array} \right\},\ \{D\} = \left\{ \begin{array}{c} 0 \\ 0 \\ D \end{array} \right\} \tag{4.56}$$

- **Linear piezoelectricity** for each piezoelectric layer k; it is assumed that the piezoelectric principal axes are parallel the structural orthotropy axes and that the poling direction is direction 3. It is also assumed that no shear strain is induced by a transverse electric field (i.e. $e_{34} = e_{35} = e_{36} = 0$), which is the case for most commonly used piezoelectric materials in laminar design: *PZT* and *PVDF* (see §2.2.2).

The constitutive equations for the k^{th} layer become

$$\{T\} = [c]_k \{S\} - \left\{ \begin{array}{c} e_{31} \\ e_{32} \\ 0 \end{array} \right\}_k E_k \tag{4.57}$$

$$D_k = \left\{ \begin{array}{ccc} e_{31} & e_{32} & 0 \end{array} \right\}_k \{S\} + \varepsilon_k E_k \tag{4.58}$$

$$\{\tau\} = [c_t]_k \{\gamma\} \tag{4.59}$$

where $[c]_k$ and $[c_t]_k$ are the *in-plane* and *transverse shear* elastic coefficients matrix of the k^{th} layer (stiffness matrices in the principal material axes).

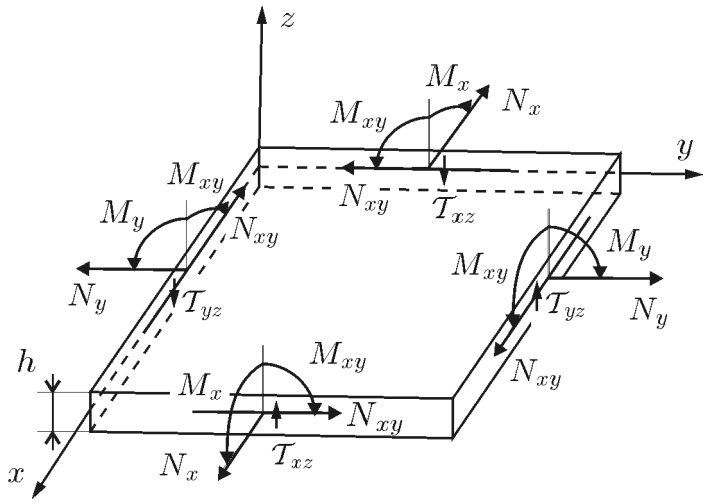

Figure 4.1: Resultant efforts

In-plane efforts $\{N\}$, bending moments $\{M\}$ and transverse shear loads $\{\mathcal{T}\}$ (Fig.4.1) can be determined by integrating the stresses over the thickness of the multilayered material

$$\{N\} = \int_{-\frac{h}{2}}^{+\frac{h}{2}} \{T\}\, dz$$

$$\{M\} = \int_{-\frac{h}{2}}^{+\frac{h}{2}} \{T\} z\, dz$$

$$\{\mathcal{T}\} = \int_{-\frac{h}{2}}^{+\frac{h}{2}} \{\tau\}\, dz$$

Upon introducing the transverse shear strains $\{\gamma\} = \{\gamma_{xz}\ \gamma_{yz}\}^T$ and the transverse shear loads $\{\mathcal{T}\} = \{\mathcal{T}_{xz}\ \mathcal{T}_{yz}\}^T$, the constitutive equations for a *Mindlin* piezoelectric shell can be derived from the ones for a *Kirchhoff* piezoelectric shell (Equ.(2.73) and (2.74)). The global constitutive equations of the piezoelectric *Mindlin* shell finally read

$$\left\{ \begin{array}{c} N \\ M \\ \mathcal{T} \end{array} \right\} = \left[\begin{array}{ccc} A & B & 0 \\ B & D & 0 \\ 0 & 0 & K \end{array} \right] \left\{ \begin{array}{c} \epsilon_0 \\ \kappa \\ \gamma \end{array} \right\} + \sum_{k=1}^{n} \left[\begin{array}{c} I_3 \\ z_{mk}\, I_3 \\ 0 \end{array} \right] [R_T]_k^{-1} \left\{ \begin{array}{c} e_{31} \\ e_{32} \\ 0 \end{array} \right\}_k \phi_k \tag{4.60}$$

$$D_k = \{e_{31}\ e_{32}\ 0\}_k\, [R_S]_k\, [I_3\ z_{mk} I_3\ 0] \left\{ \begin{array}{c} \epsilon_0 \\ \kappa \\ \gamma \end{array} \right\} - \frac{\varepsilon_k}{h_k} \phi_k \tag{4.61}$$

where the load vector now includes the in-plane loads $\{N\}$ and moments $\{M\}$ and the transverse shear loads $\{\mathcal{T}\}$. Similarly, the strain vector includes the mid-plane membrane strains $\{\epsilon_0\}$, the curvatures $\{\kappa\}$ and the transverse shear strains $\{\gamma\}$. In Equ.(4.61), the stiffness matrices A, B and D are given by the classical relationships for a multilayered material (Equ.(2.65) to (2.67)). The transverse shear stiffness matrix K is obtained following a method similar to that described in Appendix A (See also Jetteur, 1991).

It follows that the element mass, stiffness, piezoelectric coupling and capacitance matrices for a piezoelectric *Mindlin* shell element read

$$[\mathcal{M}] = \int_\Omega m [\mathcal{N}]^T [\mathcal{N}] d\omega \tag{4.62}$$

$$[K_{uu}] = \int_\Omega [\mathcal{B}]^T \left[\begin{array}{ccc} A & B & 0 \\ B & D & 0 \\ 0 & 0 & K \end{array} \right] [\mathcal{B}] d\Omega \tag{4.63}$$

$$[K_{u\phi}] = \int_\Omega [\mathcal{B}]^T \left[\begin{array}{ccc} \cdots & \mathcal{E}_k^T & \cdots \\ \cdots & \mathcal{E}_k^T z_{mk} & \cdots \\ \cdots & 0 & \cdots \end{array} \right] d\Omega \tag{4.64}$$

$$[K_{\phi\phi}] = -\Omega \left[\begin{array}{ccc} \ddots & & 0 \\ & \varepsilon_k/h_k & \\ 0 & & \ddots \end{array} \right] \tag{4.65}$$

$$[K_{\phi u}] = [K_{u\phi}]^T \tag{4.66}$$

where we have introduced

$$\{\mathcal{E}\}_k = \left\{ \begin{array}{ccc} e_{31} & e_{32} & 0 \end{array} \right\}_k [R_S]_k \tag{4.67}$$

and we have used the fact that

$$[R_T]_k^{-1} \left\{ \begin{array}{ccc} e_{31} & e_{32} & 0 \end{array} \right\}_k^T = \{\mathcal{E}\}_k^T \tag{4.68}$$

4.6 Implementation

Referring to the electromechanical analogy mentioned in Table 4.1 (§4.2), the electrical charge brought to the system can be considered similarly to the applied forces, and the voltages similarly to the nodal displacements. To implement the piezoelectricity into the commercial finite element package *Samcef*, the strategy adopted was to modify existing elements in the *Samcef* library. More precisely, the piezoelectric coupling has been added at the element level by complementing the integrated stiffness matrix with the piezoelectric coupling and capacitive contributions. The voltages being similar to nodal displacement and the electric charges brought to the system similar to external forces, the assembly and resolution algorithms remain. However, some bad numerical conditioning is likely to appear due to the several order of magnitude difference between the numerical values of the fields involved. If displacements are written in meters (m), forces in Newtons (N), voltages in Volts (V), electrical charges in Coulomb (Cb), then elastic coefficients are written in Pascals (N/m^2 or Pa), capacitances in Farads (Cb/V or F) and piezoelectric coupling coefficients in (Cb/m^2). Taking the example of *PVDF* with typical dimensions ($\sim$ 1 mm thick, with elements of $\sim$ 1 cm^2), the orders of magnitude are: 10^{-3} to 10^4 for mechanical stiffness terms, 10^{-5} to 10^{-2} for the piezoelectric coupling terms and 10^{-9} for the capacitance terms; there are 13 orders of magnitude difference between terms of the complemented stiffness matrix. A suitable choice of units reduces this difference significantly (e.g. voltages in kV and electrical charges in mCb would lead to a 6 orders of magnitude difference).

With the cooperation of *Samtech s.a.*, electrical *dof* were added (1 per piezoelectric layer for the shell elements, 1 per node for the volume elements) and a new material of type *piezoelectric* has been added.

Both rectangular and triangular *Mindlin* shell elements are available, together with several volume elements: prismatic, tetrahedric and parallelipipedic.

4.6.1 Shell implementation

As many electrical *dof* as piezoelectric layers have been added to the *Mindlin* shell elements. The element stiffness matrix is integrated over the surface of the element using a *Gauss* integration, that is, a weighted sum of the values to integrate, taken in g particular points called *Gauss points* (e.g. Hughes, 1987).

As we start from an existing element, the value of the derivatives of the shape function ($[\mathcal{B}]$) taken at the *Gauss points* are already available. The piezoelectric coupling and the capacitance contributions to the element stiffness matrix $[K_{elt}]$ at each *Gauss point* is computed. The generalized stiffness matrix is complemented as well as the matrix of shape function derivatives.

$$[K_{elt}] = \sum_{i=1}^{g} g_i \left(\begin{bmatrix} [\mathcal{B}]_{(i)}^T & 0 \\ 0 & I_n \end{bmatrix} \left[\begin{array}{ccc|ccc} A & B & 0 & & \mathcal{E}_k^T & \\ B & D & 0 & \dots & \mathcal{E}_k^T z_{mk} & \dots \\ 0 & 0 & K & & 0 & \\ \hline & \vdots & & \ddots & & 0 \\ \mathcal{E}_k & \mathcal{E}_k z_{mk} & 0 & & -\varepsilon_k/h_k & \\ & \vdots & & 0 & & \ddots \end{array}\right] \begin{bmatrix} [\mathcal{B}]_{(i)} & 0 \\ 0 & I_n \end{bmatrix} \right) \quad (4.69)$$

Where g is number of *Gauss* points and g_i represent the *Gauss* weights ($i = 1, \dots g$) and n is the number of piezoelectric layers ($k = 1, \dots n$). The assembly takes into account the equipotentiality condition of the electrodes; this reduces the number of electric variables to the number of electrodes.

A voltage is specified across a piezoelectric layer by imposing a *mechanical displacement* to the corresponding node. An electrical charge is brought to a piezoelectric layer by applying a *force* to the corresponding node. A voltage appears as a *mechanical displacement* and an electrical charge as a *reaction force*.

4.6.2 Transverse piezoelectric shear mode in shell elements

Implementing the multi-layered piezoelectric elements, we did not consider the piezoelectric shear mode (dictated by coefficient e_{15} or e_{24}); the electric and displacement fields were assumed to be parallel to the poling direction. However, the use of a *Mindlin* formulation (accounting for the transverse shear) allows us to consider transverse shear piezoelectric coupling and therefore, a poling direction no longer normal to the plate. As the poling direction is not anymore direction 3, the piezoelectric coefficients to be considered are not anymore necessarily e_{31} and e_{32}. The piezoelectric coefficients considered next are $e_{\bullet 1}, e_{\bullet 2}, e_{\bullet 6} = 0, e_{\bullet 4}$ and $e_{\bullet 5}$ where $\bullet$ is put for the material direction aligned with the direction normal to the plate.

As the transverse shear is entirely decoupled, Equ.(4.60) can be decomposed as follow:

$$\begin{Bmatrix} N \\ M \end{Bmatrix} = \begin{bmatrix} A & B \\ B & D \end{bmatrix} \begin{Bmatrix} \epsilon_0 \\ \kappa \end{Bmatrix} + \sum_{k=1}^{n} \begin{bmatrix} I_3 \\ z_{mk}\, I_3 \end{bmatrix} [R_T]_k^{-1} \begin{Bmatrix} e_{\bullet 1} \\ e_{\bullet 2} \\ 0 \end{Bmatrix}_k \phi_k \quad (4.70)$$

$$\{\mathcal{T}\} = [K]\{\gamma\} + \sum_{k=1}^{n} [\mathcal{R}]_k^{-1} \begin{Bmatrix} e_{\bullet 4} \\ e_{\bullet 5} \end{Bmatrix}_k \phi_k \quad (4.71)$$

$$D_k = \{e_{\bullet 1}\ e_{\bullet 2}\ 0\}_k [R_S]_k [I_3\ z_{mk} I_3] \begin{Bmatrix} \epsilon_0 \\ \kappa \end{Bmatrix} + \{e_{\bullet 4}\ e_{\bullet 5}\}_k [\mathcal{R}]_k \{\gamma\} - \frac{\varepsilon_k}{h_k}\phi_k \quad (4.72)$$

The transformation matrix $[\mathcal{R}]_k$ relates the transverse shear stresses and strains written in the material axes (LT) to the transverse shear stresses and strains written in the composite axes (xy). We have

$$\begin{Bmatrix} \tau_{Tz} \\ \tau_{Lz} \end{Bmatrix} = [\mathcal{R}]_k \begin{Bmatrix} \tau_{yz} \\ \tau_{xz} \end{Bmatrix} \quad (4.73)$$

$$\left\{ \begin{array}{c} \gamma_{Tz} \\ \gamma_{Lz} \end{array} \right\} = [\mathcal{R}]_k \left\{ \begin{array}{c} \gamma_{yz} \\ \gamma_{xz} \end{array} \right\} \tag{4.74}$$

The transformation matrix is given by

$$[\mathcal{R}]_k = \left[\begin{array}{cc} \cos\theta_k & -\sin\theta_k \\ \sin\theta_k & \cos\theta_k \end{array} \right] \tag{4.75}$$

If we introduce

$$\{\mathcal{X}\}_k = \{e_{\bullet 4}\ e_{\bullet 5}\}\,[\mathcal{R}]_k \tag{4.76}$$

We have also

$$\{\mathcal{X}\}_k^T = [\mathcal{R}]_k^{-1}\,\{e_{\bullet 4}\ e_{\bullet 5}\}^T \tag{4.77}$$

and the generalized stiffness matrix (4.69) can be complemented to account for the transverse shear piezoelectric coupling contribution

$$[K_{elt}] = \sum\nolimits_{i=1}^{g} g_i \left(\left[\begin{array}{cc} [\mathcal{B}]_{(i)}^T & 0 \\ 0 & I_n \end{array} \right] \left[\begin{array}{ccc|ccc} A & B & 0 & & \mathcal{E}_k^T & \\ B & D & 0 & \dots & \mathcal{E}_k^T z_{mk} & \dots \\ 0 & 0 & K & & \mathcal{X}_k^T & \\ \hline & \vdots & & \ddots & & 0 \\ \mathcal{E}_k & \mathcal{E}_k z_{mk} & \mathcal{X}_k & & -\varepsilon_k/h_k & \\ & \vdots & & 0 & & \ddots \end{array} \right] \left[\begin{array}{cc} [\mathcal{B}]_{(i)} & 0 \\ 0 & I_n \end{array} \right] \right) \tag{4.78}$$

By suitably choosing the coupling coefficients corresponding to the application considered, this implementation allows to consider the piezoelectric shear mode as well as the extension mode.

extension

$e_{\bullet 1} = e_{31}$; $e_{\bullet 2} = e_{32}$
$e_{\bullet 4} = e_{\bullet 5} = 0$

shear

$e_{\bullet 1} = e_{\bullet 2} = 0$
$e_{\bullet 4},\ e_{\bullet 5} = e_{24},\ e_{15}$ depending on the coupling characteristics and the poling direction.

This was also implemented for the sake of completeness. However, the hypothesis of a uniform transverse shear strain distribution through the thickness is not satisfactory (See e.g. the shear bender of Fig.5.8, §5.1.3); a more elaborate shell element would be necessary (higher order transverse shear strain distribution). As the shear actuation requires a relatively important thickness, a volumic approach can also be used (strategy used in §5.1.3).

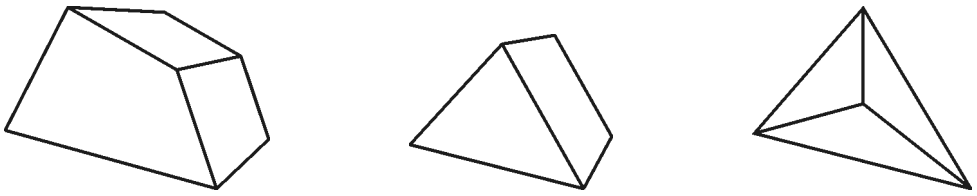

(a) Brick (T008) (b) Prism (T046) (c) Tetrahedron (T047)

Figure 4.2: 3-D volume elements from *Samcef* library

4.6.3 Volume implementation

The variety of 3-D volume elements available in the *Samcef* library (Fig.4.2) permits a good representation of geometrically complex structures.

These elements are available at degree one (linear shape functions), degree two (quadratic shape functions) or mixed. If each element edge is degree one, internal modes improve flexural behaviour. These internal modes are selected by default, but it is possible to remove them. Degree two can be as well explicitely defined by nodes, or implicitely (with automatic creation of interface degrees of freedom on the edges). When one of the dimensions becomes small with respect to the others, the shape of the element tends to be a shell. In this case, a particular constitutive law, uncoupling the stress along the thickness, can be adopted so that the element can better simulate shell behaviours (SAMTECH, 2000).

The idea is again to complement existing elements with electrical degrees of freedom. One electrical degree of freedom per node has been added: the electric potential. The elements *stiffness* matrice is augmented accordingly with the piezoelectric coupling and capacitive terms. The derivatives of the shape functions ($[\mathcal{B}_u]_{(i)}, [\mathcal{B}_\phi]_{(i)}$) taken at the *Gauss point i* are already available. The piezoelectric coupling and the capacitance contributions to the element stiffness matrix $[K_{elt}]$ in each *Gauss point* are computed and left and right multiplied by the shape functions derivatives.

$$[K_{elt}] = \sum_{i=1}^{g} g_i \begin{bmatrix} [\mathcal{B}_u]_{(i)} & 0 \\ 0 & [\mathcal{B}_\phi]_{(i)} \end{bmatrix}^T \begin{bmatrix} [K_{uu}] & [K_{u\phi}] \\ [K_{u\phi}]^T & [K_{\phi\phi}] \end{bmatrix} \begin{bmatrix} [\mathcal{B}_u]_{(i)} & 0 \\ 0 & [\mathcal{B}_\phi]_{(i)} \end{bmatrix} \tag{4.79}$$

Where g is the number of *Gauss* points and g_i represent the *Gauss* weights ($i = 1, \dots g$). We have

$$[K_{elt}] = \sum_{i=1}^{g} g_i \begin{bmatrix} [\mathcal{B}_u]_{(i)}^T [K_{uu}] [\mathcal{B}_u]_{(i)} & [\mathcal{B}_u]_{(i)}^T [K_{u\phi}] [\mathcal{B}_\phi]_{(i)} \\ [\mathcal{B}_\phi]_{(i)}^T [K_{u\phi}]^T [\mathcal{B}_u]_{(i)} & [\mathcal{B}_\phi]_{(i)}^T [K_{\phi\phi}] [\mathcal{B}_\phi]_{(i)} \end{bmatrix} \tag{4.80}$$

4.7 Particular electrical boundary conditions

4.7.1 Voltage driven electrodes

If the electric potential $\{\Phi\}$ is controlled, the governing equations become

$$[\mathcal{M}]\{\ddot{U}\} + [K_{UU}]\{U\} = \{F\} - [K_{U\Phi}]\{\Phi\} \tag{4.81}$$

where the second term in the right hand side represents the equivalent piezoelectric loads. Once the mechanical displacements have been computed, the electric charges appearing on the electrodes can be computed from Equ.(4.35). From Equ.(4.81), we see that the eigenvalues problem of the system with short-circuited electrodes ($\{\Phi\} = 0$) is:

$$\left([K_{UU}] - \omega^2[\mathcal{M}]\right)\{U\} = 0 \tag{4.82}$$

It can be seen from Equ.(4.82) that the natural frequencies and modes shape are the same as if there was no piezoelectric electromechanical coupling.

4.7.2 Charge driven electrodes

Conversely, open electrodes correspond to a charge condition $\{G\} = 0$. In this case, Equ.(4.35) becomes

$$\{\Phi\} = -[K_{\Phi\Phi}]^{-1}[K_{\Phi U}]\{U\} \tag{4.83}$$

and, upon substituting into Equ.(4.34), it becomes

$$[\mathcal{M}]\{\ddot{U}\} + \left([K_{UU}] - [K_{U\Phi}][K_{\Phi\Phi}]^{-1}[K_{\Phi U}]\right)\{U\} = \{F\} \tag{4.84}$$

which shows that the stiffness matrix depends on the electrical boundary conditions. The piezoelectric electromechanical coupling increases the overall stiffness of the system if the electrodes are left open (the terms of $[K_{\Phi\Phi}]$ being negative); the natural frequencies are greater than if the coupling is neglected. (See Appendix B). This phenomenon becomes more and more important as the amount of piezoelectric material embedded increases.

4.7.3 Electrodes connected via a passive network

If the electrodes are connected via a passive electrical network of impedance matrix $[Z]$, Equ.(4.34) and (4.35) must be complemented by the network equation (Fig.4.3). Since the electrical current is given by the time derivative of the electrical charge $\{I\} = \{\dot{G}\}$, the connected electrical network equation reads, in *Laplace* notations:

$$\{\Phi\} = -[Z]\{I\} = -[Z(s)]s\{G\} \tag{4.85}$$

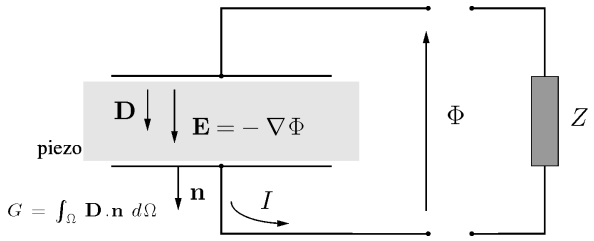

Figure 4.3: Electrodes connected to an external impedance

4.8 From finite element model to state space model

The idea behind modelling structures embedding piezoelectric actuators and sensors using finite elements is indeed to gather the necessary information to design a good control strategy. It is therefore necessary to interface the structural analysis software (finite element package) with a control design software. A method to extract a state space representation of the structure dynamics with its piezoelectric inputs and outputs from a finite element analysis is presented hereafter.

Equ.(4.34) can be complemented with a damping term $[C]\{\dot{U}\}$ to obtain the full equation of dynamics and the sensor equation:

$$\{0\} = [\mathcal{M}]\{\ddot{U}\} + [C]\{\dot{U}\} + [K_{UU}]\{U\} + [K_{U\Phi}]\{\Phi\} \tag{4.86}$$

$$\{G\} = [K_{\Phi U}]\{U\} + [K_{\Phi\Phi}]\{\Phi\} \tag{4.87}$$

where $\{U\}$ represents the mechanical *dof*, $\{\Phi\}$ the electric potential *dof*, $[\mathcal{M}]$ the inertial matrix, $[C]$ the damping matrix, $[K_{UU}]$ the mechanical stiffness matrix, $[K_{U\Phi}] = [K_{\Phi U}]^T$ the electromechanical coupling matrix and $[K_{\Phi\Phi}]$ the electric capacitance matrix.

Voltage actuation and charge sensing are considered. Actuation is done by imposing a voltage $\{\Phi\}$ on the actuators and sensing by imposing a zero voltage ($\{\Phi\} = \{0\}$) and measuring the reaction (electric) charge $\{G\}$ appearing on the sensors.

What do we want to do ?

We want to reduce the electromechanical system to its actuation inputs and sensor outputs, keeping its dynamic behaviour; we want to get a state space model of the system to be used in a control design process.

What is the strategy ?

We have basically three categories of electrodes:

1. unused (for control) electrodes (with various boundary conditions): $\{\Phi^{(u)}\}$
2. actuator electrodes (imposed voltage): $\{\Phi^{(i)}\}$

3. sensor electrodes (zero voltage), the reaction (electric) charge $\{G^{(o)}\}$ is sought

The unused electrodes are considered as part of the *mechanical* system; the related *dof* are *condensed* according to the boundary conditions (See §4.7) and the mass, damping, stiffness, piezoelectric coupling and capacitance matrices are adapted in consequence (the notation remains for the sake of clarity).

$$\{0\} = [\mathcal{M}]\{\ddot{U}\} + [C]\{\dot{U}\} + [K_{UU}]\{U\} + [K_{U\Phi}^{(i)}]\{\Phi^{(i)}\} \tag{4.88}$$

$$\{G^{(o)}\} = [K_{\Phi U}^{(o)}]\{U\} + [K_{\Phi\Phi}^{(oi)}]\{\Phi^{(i)}\} \tag{4.89}$$

The strategy is to use a truncated modal decomposition. A solution of the form $\{U\} = \sum_k \{\mathcal{Z}_k\}\, x_k(t) = [\mathcal{Z}]\{x(t)\}$ is considered, it consists in a linear combination of the mode shapes $\{\mathcal{Z}_k\}$. The mode shapes $\{\mathcal{Z}_k\}$ and the corresponding eigenfrequencies ω_k are solutions of the classical eigenproblem with closed-circuit electrical boundary conditions on both actuator and sensor electrodes.

$$([K_{UU}] - \omega_k[\mathcal{M}])\,\{\mathcal{Z}_k\} = 0 \tag{4.90}$$

and $x_k(t)$ represents the modal amplitude of mode k.

Finite element problems have usually a large number of degrees of freedom, especially if the geometry is complicated, because of the difficulty of accurately representing the stiffness of the structure. This number of degrees of freedom is unnecessarily large to represent the structural response in a limited bandwidth. If a structure is excited by a band-limited excitation, its response is dominated by the n normal modes whose eigenfrequencies belong to the bandwidth of the excitation. The solution of Equ.(4.90) can often be restricted to these n modes. The number of degrees of freedom contributing effectively to the response is therefore reduced drastically in modal coordinates.

Equ.(4.88) and (4.89) become

$$\{0\} = [\mathcal{M}][\mathcal{Z}]\{\ddot{x}\} + [C][\mathcal{Z}]\{\dot{x}\} + [K_{UU}][\mathcal{Z}]\{x\} + [K_{U\Phi}^{(i)}]\{\Phi^{(i)}\} \tag{4.91}$$

$$\{G^{(o)}\} = [K_{\Phi U}^{(o)}][\mathcal{Z}]\{x\} + [K_{\Phi\Phi}^{(oi)}]\{\Phi^{(i)}\} \tag{4.92}$$

and left-multiplying Equ.(4.93) by $[\mathcal{Z}]^T$:

$$\{0\} = [\mathcal{Z}]^T[\mathcal{M}][\mathcal{Z}]\{\ddot{x}\} + [\mathcal{Z}]^T[C][\mathcal{Z}]\{\dot{x}\} + [\mathcal{Z}]^T[K_{UU}][\mathcal{Z}]\{x\} + [\mathcal{Z}]^T[K_{U\Phi}^{(i)}]\{\Phi^{(i)}\} \tag{4.93}$$

$$\{G^{(o)}\} = [K_{\Phi U}^{(o)}][\mathcal{Z}]\{x\} + [K_{\Phi\Phi}^{(oi)}]\{\Phi^{(i)}\} \tag{4.94}$$

Using the orthogonality properties of the mode shapes (e.g. Preumont, 1997, Chap. 2).

$$[\mathcal{Z}]^T\,[\mathcal{M}]\,[\mathcal{Z}] = \mathrm{diag}(\mu_k) \tag{4.95}$$

$$[\mathcal{Z}]^T\,[K]\,[\mathcal{Z}] = \mathrm{diag}(\mu_k\omega_k^2) \tag{4.96}$$

and a classical damping

$$[\mathcal{Z}]^T[C][\mathcal{Z}] = \mathrm{diag}(2\xi_k\mu_k\omega_k) \tag{4.97}$$

the dynamic equations of the system in the state space representation finally read:

$$\left\{ \begin{array}{c} \dot{x} \\ \ddot{x} \end{array} \right\} = \left[\begin{array}{cc} 0 & I \\ -\Omega^2 & -2\xi\Omega \end{array} \right] \left\{ \begin{array}{c} x \\ \dot{x} \end{array} \right\} - \left[\begin{array}{c} 0 \\ \mu^{-1}\mathcal{Z}^T K_{U\Phi}^{(i)} \end{array} \right] \left\{ \Phi^{(i)} \right\} \tag{4.98}$$

$$\left\{ G^{(o)} \right\} = \left[\begin{array}{cc} {K_{U\Phi}^{(o)}}^T \mathcal{Z} & 0 \end{array} \right] \left\{ \begin{array}{c} x \\ \dot{x} \end{array} \right\} + [D_{HF}] \left\{ \Phi^{(i)} \right\} \tag{4.99}$$

where

the modes shape $[\mathcal{Z}]$,

the eigenfrequencies $[\Omega] = \mathrm{diag}(\omega_k)$,

the modal masses $[\mu] = \mathrm{diag}(\mu_k)$,

the modal electric charge on the sensors $[K_{\Phi U}^{(o)}][\mathcal{Z}]$, and

the modal electric charge on the actuators, transposed (by reciprocity) $[\mathcal{Z}]^T[K_{U\Phi}^{(i)}]$, representing the participation factor of the actuators to each mode,

are obtained from a *dynamic* finite element analysis.

$[\xi] = \mathrm{diag}(\xi_k)$ are the modal classical damping ratios of the considered structure

and

$[D_{HF}]$ is the *feedthrough* component of the frequency response function; part of the output is proportional to the input. It is calculated as follow:

As distinct actuator and sensor electrodes are considered, there is no cross-capacitance terms; the capacitance matrix $[K_{\Phi\Phi}^{(oi)}]$ matrix is zero and will be omitted next. If we consider the steady state response to an harmonic input voltage of frequency ω, the response will also be harmonic with the same frequency. Equ.(4.93) and (4.94) are decoupled for each mode and can be written:

$$\mu_k \left(\omega^2 x_k + 2\xi_k\omega_k\omega x_k + \omega_k^2 x_k \right) = [\mathcal{Z}_k]^T [K_{U\Phi}^{(i)}] \{\Phi^{(i)}\} \quad \text{for each mode } k \tag{4.100}$$

$$\{G^{(o)}\} = \sum\nolimits_k [K_{U\Phi}^{(o)}]^T [\mathcal{Z}_k] x_k \tag{4.101}$$

and the frequency response function $[\mathcal{G}(\omega)]$ defined by $\{G^{(o)}\} = [\mathcal{G}(\omega)]\{\Phi^{(i)}\}$ reads

$$[\mathcal{G}(\omega)] = \sum\nolimits_k \frac{\left([K_{U\Phi}^{(o)}]^T [\mathcal{Z}_k] \right) \left([\mathcal{Z}_k]^T [K_{U\Phi}^{(i)}] \right)}{\mu_k \left(\omega^2 + 2\xi_k\omega_k\omega + \omega_k^2 \right)} \tag{4.102}$$

The frequency response function $[\mathcal{G}(\omega)]$ can be written in the sum of the response of the modes inside the bandwidth (that respond dynamically) and outside the bandwidth (that respond statically).

$$[\mathcal{G}(\omega)] = \sum\nolimits_{k=1}^{n} \frac{\left([K_{U\Phi}^{(o)}]^T [\mathcal{Z}_k] \right) \left([\mathcal{Z}_k]^T [K_{U\Phi}^{(i)}] \right)}{\mu_k \left(\omega^2 + 2\xi_k\omega_k\omega + \omega_k^2 \right)} +$$

$$\sum\nolimits_{k=n+1}^{\cdots} \frac{\left([K_{U\Phi}^{(o)}]^T[\mathcal{Z}_k]\right)\left([\mathcal{Z}_k]^T[K_{U\Phi}^{(i)}]\right)}{\mu_k\omega_k^2} \tag{4.103}$$

Considering that the stationary part of frequency response function ($\omega = 0$)

$$[\mathcal{G}(0)] = \sum\nolimits_k \frac{\left([K_{U\Phi}^{(o)}]^T[\mathcal{Z}_k]\right)\left([\mathcal{Z}_k]^T[K_{U\Phi}^{(i)}]\right)}{\mu_k\omega_k^2} \tag{4.104}$$

can also be given by (from Eq.4.88 and Eq.4.89: static response)

$$[\mathcal{G}(0)] = -[K_{U\Phi}^{(o)}]^T[K_{UU}^{-1}][K_{U\Phi}^{(i)}] \tag{4.105}$$

One can write that:

$$\begin{aligned}[\mathcal{G}(\omega)] = &\sum\nolimits_{k=1}^{n} \frac{\left([K_{U\Phi}^{(o)}]^T[\mathcal{Z}_k]\right)\left([\mathcal{Z}_k]^T[K_{U\Phi}^{(i)}]\right)}{\mu_k\left(\omega^2 + 2\xi_k\omega_k\omega + \omega_k^2\right)} + \\ &\left(-[K_{U\Phi}^{(o)}]^T[K_{UU}^{-1}][K_{U\Phi}^{(i)}]\right) - \sum\nolimits_{k=1}^{n} \frac{\left([K_{U\Phi}^{(o)}]^T[\mathcal{Z}_k]\right)\left([\mathcal{Z}_k]^T[K_{U\Phi}^{(i)}]\right)}{\mu_k\omega_k^2}\end{aligned} \tag{4.106}$$

The first term is the dynamic response of the modelled modes, the two last terms form the static contribution $[D_{HF}]$ of the unmodelled modes (outside the bandwidth) to the frequency response function; it is often called the *residual mode* (Preumont, 1997; Loix, 1998; Loix et al., 1998). It is independent of the frequency and introduces an important feedthrough component in the frequency response function. The second term can easily be obtained from a static finite element analysis (Its columns are the charge appearing on the sensors when a unit voltage is applied on each actuator) while the third is the static response of the modelled modes.

$$[D_{HF}] = \left(-[K_{U\Phi}^{(o)}]^T[K_{UU}^{-1}][K_{U\Phi}^{(i)}]\right) - \sum\nolimits_{k=1}^{n} \frac{\left([K_{U\Phi}^{(o)}]^T[\mathcal{Z}_k]\right)\left([\mathcal{Z}_k]^T[K_{U\Phi}^{(i)}]\right)}{\mu_k\omega_k^2} \tag{4.107}$$

Truncating the modal expansion of a frequency response function without introducing a residual mode can lead to substantial errors in the prediction of the open-loop zeros. This will be illustrated in Chapter 5 (See Fig.5.30, §5.3.1).

Such a state space representation is easily implemented in a control oriented software allowing the designer to extract the various frequency response functions and to use the available control design tools.

Chapter 5

Applications

This chapter is devoted to the test cases, benchmarks and experimental validations of the modelling tools presented.

5.1 Examples

5.1.1 Influence of the electromechanical coupling on the natural frequencies

The electromechanical piezoelectric coupling is responsible for an influence of the electrical boundary conditions on the mechanical natural frequencies (See Appendix B).

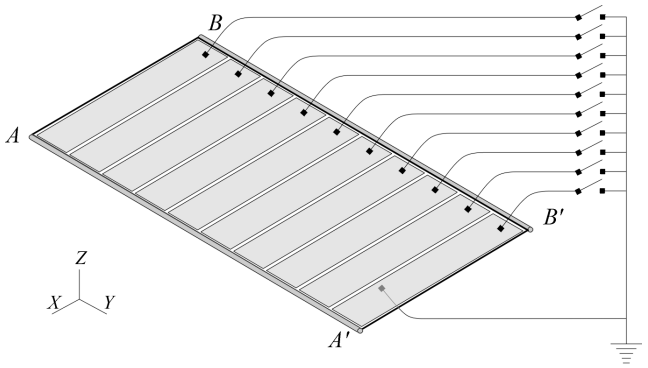

Figure 5.1: Simply supported steel plate

To illustrate this phenomenon, a steel plate (100 cm $\times$ 50 cm, thickness: 0.5 mm) entirely covered with piezoceramics (PZT, thickness: 0.25 mm) as represented on Fig.5.1 is considered. The plate is simply supported on two opposite sides (AA' and BB'). The grounded steel plate acts as an electrode and 10 electrodes are regularly distributed along the length ($AB \rightarrow A'B'$). Initially not connected, they are gradually grounded. A dynamic analysis is done for each additional grounded electrode and a record of the natural frequencies is kept.

The materials characteristics are listed in Table 5.1. The FE mesh used is represented on Fig.5.2.

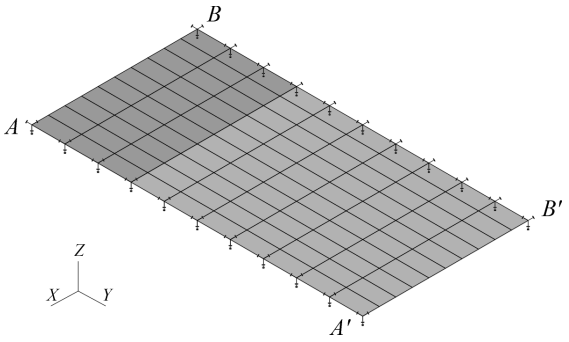

Figure 5.2: *FE* mesh: 30% grounded

The evolution of the natural frequencies with respect to the percentage of grounded electrodes is presented on Fig.5.3. It should be noted that the results obtained with the uncoupled model correspond to 100% of grounded electrodes; a zero voltage imposed on every piezoceramics involves no stiffening of the structure (See §4.7.1): if all the electrodes are short-circuited, the natural frequencies and modes are as if there was no piezoelectric coupling.

Y_{steel}	210	(GPa)
ν_{steel}	0.3	
ρ_{steel}	7800	(kg/m^3)
E_{piezo}	65	(GPa)
ν_{piezo}	0.3	
ρ_{piezo}	7800	(kg/m^3)
ε_r	2600	
$d_{31} = d_{32}$	190.10^{-12}	(m/V)

Table 5.1: Characteristics of the materials

The data file is listed in Appendix C.1 to illustrate the way the piezoelectric characteristics and electrical boundary conditions are specified compared to mechanical ones.

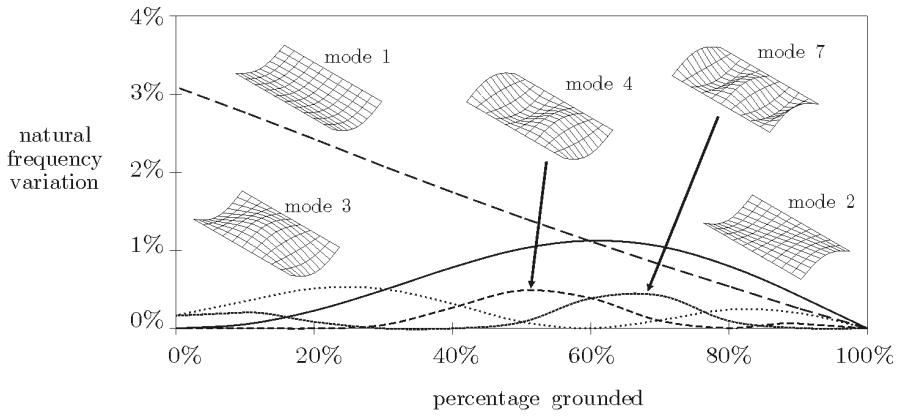

Figure 5.3: Stiffening effect resulting from the piezoelectric coupling

5.1.2 Cantilever piezoelectric plate

A cantilever steel plate 455 mm long and 50 mm wide is considered; the steel plate is 0.5 mm thick and two piezoceramic strips 250 μm thick, 55 mm long and 25 mm wide are bounded symmetrically 15 mm from the clamp. One is used as actuator and the other as sensor. The finite element mesh used and the three first eigenmodes are represented on Fig.5.4.

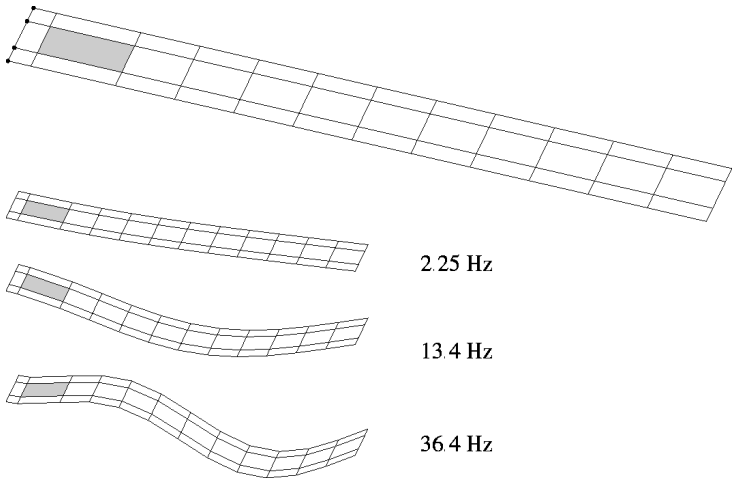

Figure 5.4: *FE* modal analysis

For the description of the files and commands used to generate this example, see Appendix C.2. The state space model generated can be used with all the tools provided with *Matlab-Simulink* and the various toolboxes available. The frequency response function of the system is shown on Fig.5.5. The dedicated *Matlab* macros are succintly described in Appendix D.

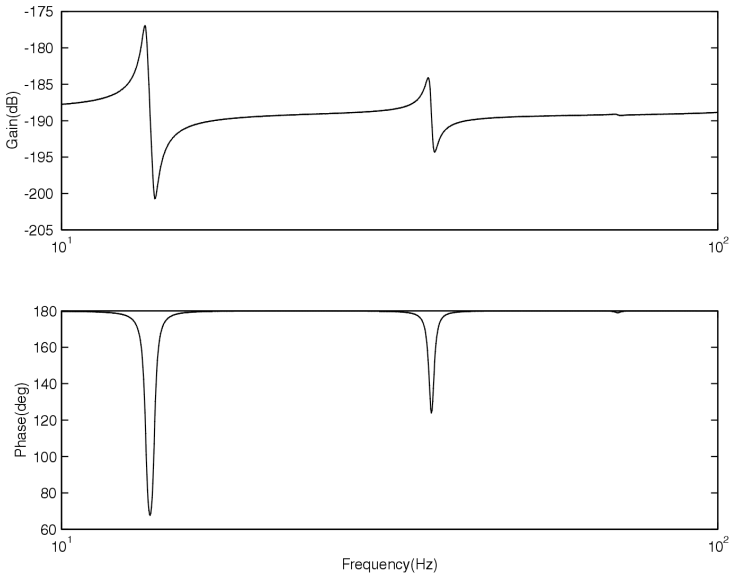

Figure 5.5: Open loop frequency response function

5.1.3 Shear bender

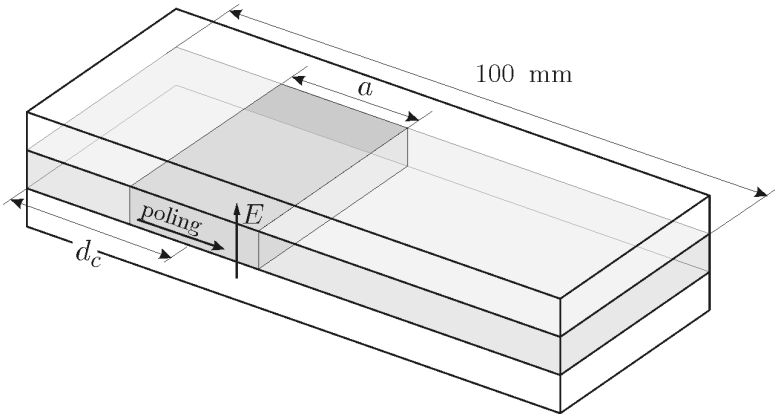

Figure 5.6: Shear bender

This is an example of a static analysis using piezoelectric volume elements. The use of the shear mode of piezoelectric materials has been investigated by Benjeddou et al. (1997, 1998). The proposed architecture consists in a sandwiched beam for which part of the core has been replaced by piezoelectric material. The proposed configuration is such that, this time, the d_{15} coupling coefficient dictates the design (See §3.1). The electric field is applied perpendicularly to the poling direction, inducing a transverse shear strain. A finite element solution using sandwich beam has been proposed by Benjeddou et al. and compared to analytical results.

The bender of Fig.5.6 is considered; it consists in a cantilever beam 100 mm long formed of a 2 mm rigid foam core sandwiched by two 8 mm thick aluminium skins. The core is partially replaced by *PZT* piezoceramics to form an actuator of length a at a distance d_c from the clamp. A 20 V voltage is applied between top and bottom surfaces of the piezoelectric layer. The material properties are summarized in Table 5.2.

As a first test case, the core is totally replaced by the piezoactuator (there is no rigid foam). The mesh is shown on Fig.5.7 and the static deformation on Fig.5.8. The comparison with the FE and analytical results from Benjeddou et al. (1997) shows a good agreement (tip deflection: 1.18 10^{-7} m (This study), 1.19 10^{-7} m (Benjeddou et al., 1997))

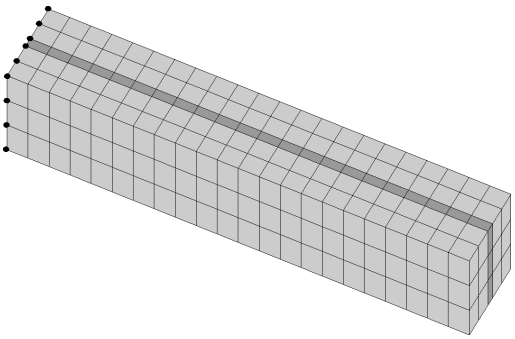

Figure 5.7: *FE* mesh

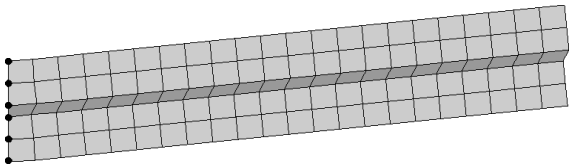

Figure 5.8: Static deformation

Aluminium		
ρ	2690	(kg/m^3)
Y	70.3	(GPa)
ν	0.345	
Foam		
ρ	32	(kg/m^3)
Y	35.3	(MPa)
ν	0.383	
PZT-5H		
ρ	7730	(kg/m^3)
$[c]$	$\begin{bmatrix} 126 & 79.5 & 84.1 & 0 & 0 & 0 \\ 79.5 & 126 & 84.1 & 0 & 0 & 0 \\ 84.1 & 84.1 & 126 & 0 & 0 & 0 \\ 0 & 0 & 0 & 23.3 & 0 & 0 \\ 0 & 0 & 0 & 0 & 23.0 & 0 \\ 0 & 0 & 0 & 0 & 0 & 23.0 \end{bmatrix}$	(GPa)
$[\varepsilon]$	$\begin{bmatrix} 1.503 & 0 & 0 \\ 0 & 1.503 & 0 \\ 0 & 0 & 1.3 \end{bmatrix} 10^{-8}$	(F/m)
$[e]$	$\begin{bmatrix} 0 & 0 & 0 & 0 & 0 & 17 \\ 0 & 0 & 0 & 0 & 17 & 0 \\ -6.5 & -6.5 & 23.3 & 0 & 0 & 0 \end{bmatrix}$	(Cb/m)

Table 5.2: Material properties

As a second case, an actuator of length $a = 10$ mm replace part of the core. Its position is set to vary between 10 mm and 90 mm. The mesh is shown on Fig.5.9 and resulting deformations for different locations of the actuator are shown on Fig.5.10. Tip deflection vs actuator position is compared to results found in (Benjeddou et al., 1997) on Fig.5.11.

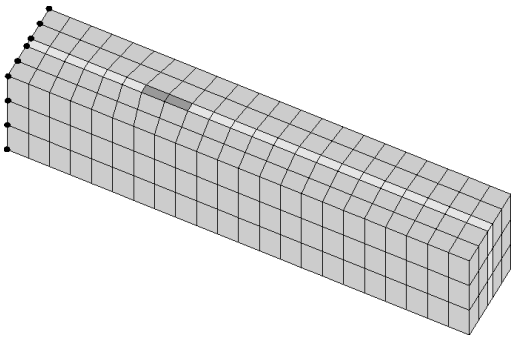

Figure 5.9: *FE* mesh

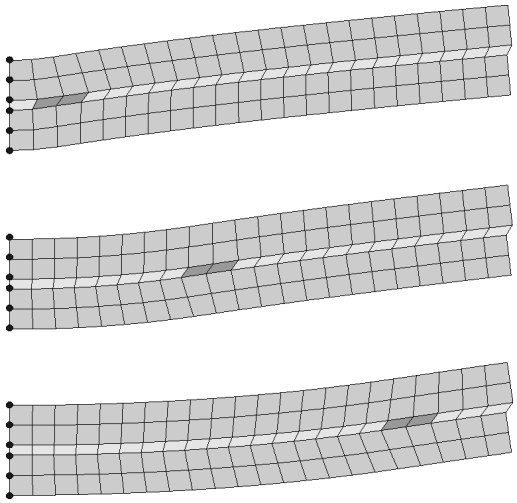

Figure 5.10: Resulting deformation

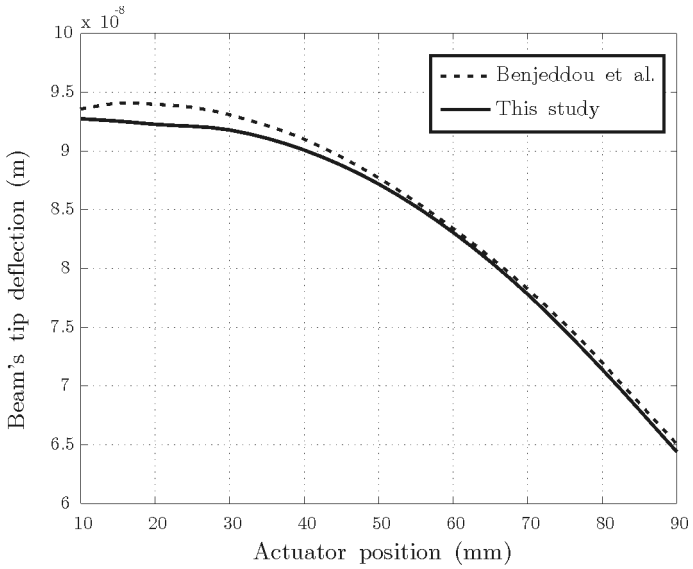

Figure 5.11: Tip deflection vs actuator position

5.2 Actuation and sensing

5.2.1 Bimorph beam

The piezoelectric bimorph pointer (Fig.5.12) is a beam made of two uniaxial piezoelectric layers with opposite polarity stacked together to obtain a bending actuator/sensor. This device can be used for micro-actuation or strain sensing.

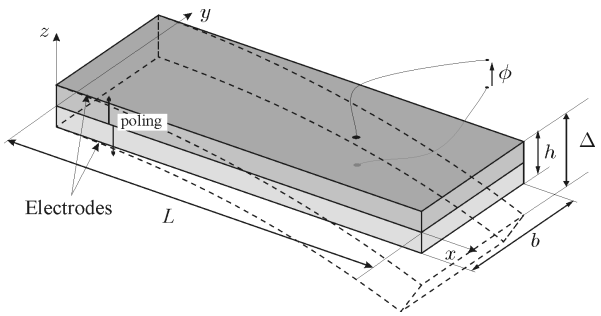

Figure 5.12: Bimorph pointer

When an external voltage is applied across the thickness, the induced strain generates moments that bend the bimorph beam. The calculated static deflection of the beam (Mindlin shell finite element *Samcef*) is compared with the analytical solution described hereafter and with the finite element and experimental solutions found by Hwang & Park (1993) and Tzou & Ye (1996). The bimorph pointer is first considered as an actuator: a unit voltage ($\phi = 1\ V$) is applied across the thickness of a $PVDF$ beam (length $L = 100$ mm, width $b = 5$ mm, thickness $h = 1$ mm). The material properties of the considered mono-oriented $PVDF$ are shown in table 5.3.

ρ	1800	(kg/m^3)
Y_1	2.0	(GPa)
Y_2	2.0	(GPa)
G_{12}	0.775	(GPa)
ν	0.29	
ε	$1.062\ 10^{-10}$	(F/m)
d_{31}	$2.2\ 10^{-11}$	(Cb/N)
d_{32}	0	(Cb/N)

Table 5.3: *PVDF* properties

Actuation: analytical solution

Using the classical theory of beams (*Bernoulli-Euler*) and the linear piezoelectric constitutive equations (Equ.2.34), the bending moment M reads:

$$\begin{aligned} M &= \frac{bh^2}{4} e_{31} E \\ &= \frac{bh^2}{4} \left(Y d_{31}\right) \frac{\phi}{h} \\ &= \frac{bh}{4} d_{31} Y \phi \end{aligned} \tag{5.1}$$

and the deflection:

$$\frac{\partial^2 z}{\partial x^2} = -\frac{M}{YI} \tag{5.2}$$

$$\begin{aligned} z\left(x\right) &= -\frac{M}{YI}\frac{x^2}{2} \\ &= -\frac{3}{2}\frac{d_{31}\phi}{h^2} x^2 \end{aligned} \tag{5.3}$$

Actuation: finite element solution

The bimorph pointer was meshed with 10 identical rectangular shell elements along the length and clamped at one end. One should note that the use of shell elements will induce unwanted stress concentration near the clamping points due to the *Poisson* effect. Figure 5.13 shows the comparison between the analytical, finite element, and experimental results found by Tzou & Ye (1996) and the analytical and finite element results of the present study.

Sensing: finite element solutions

Conversely, the piezoelectric bimorph beam can be used as a sensing device: a 10 mm tip deflection is imposed and the output voltage appearing over the electrodes is calculated (the electrical circuit being left open).

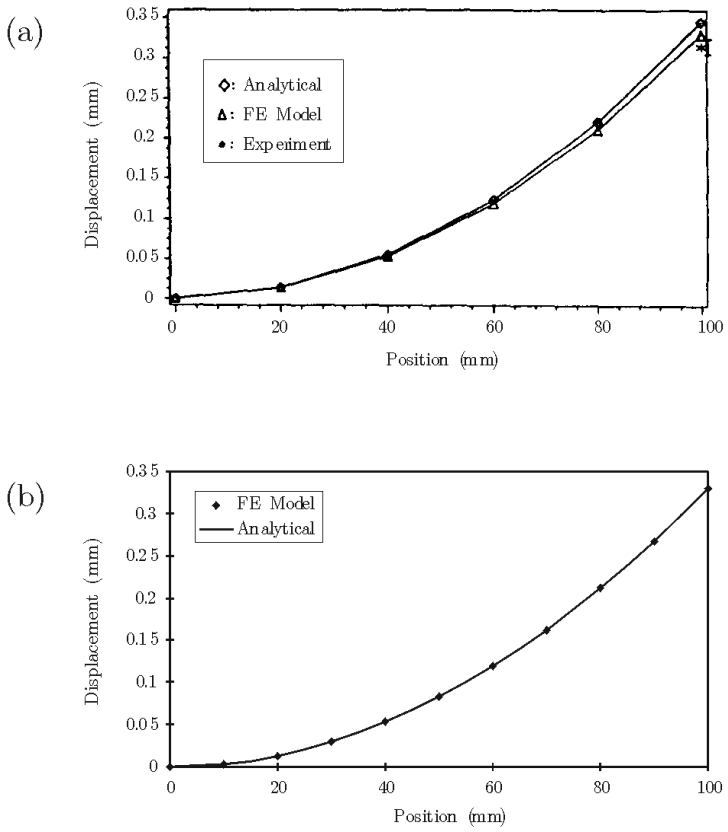

Figure 5.13: Static deflection
a. (Tzou & Ye, 1996)
b. Present study

Two cases for the electrical boundary conditions are considered (two sensor electrodes distributions). The first case consists in two electrodes sandwiching the whole beam resulting in one unique sensor averaging the strain over the length of the beam. The second case consists in five identical pairs of electrodes sandwiching the beam and regularly distributed along the length (Fig.5.14) resulting in five sensors discretizing the beam. The results are compared to those found by Hwang & Park (1993) using a quadrangular pure bending plate element neglecting the transverse shear, in Fig.5.15.

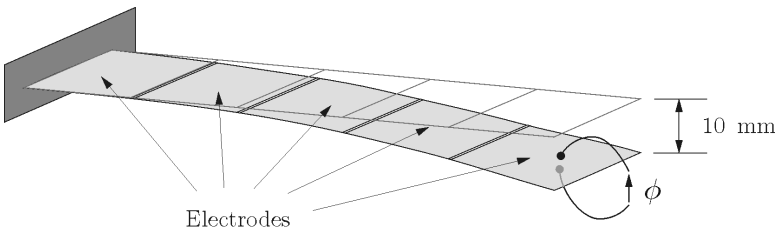

Figure 5.14: Bimorph sensor

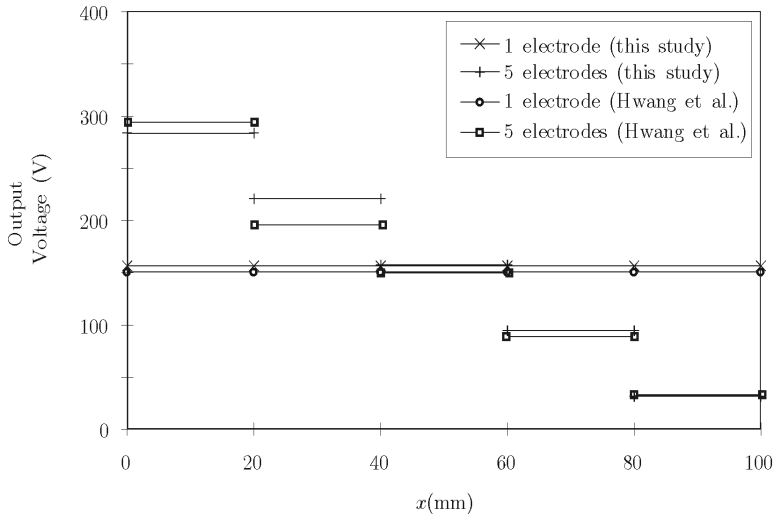

Figure 5.15: Results

This case has also been used to benchmark the volume elements. The result given by a 2×25 volume elements mesh is compared to the 5 shell elements mesh result on Fig.5.16.

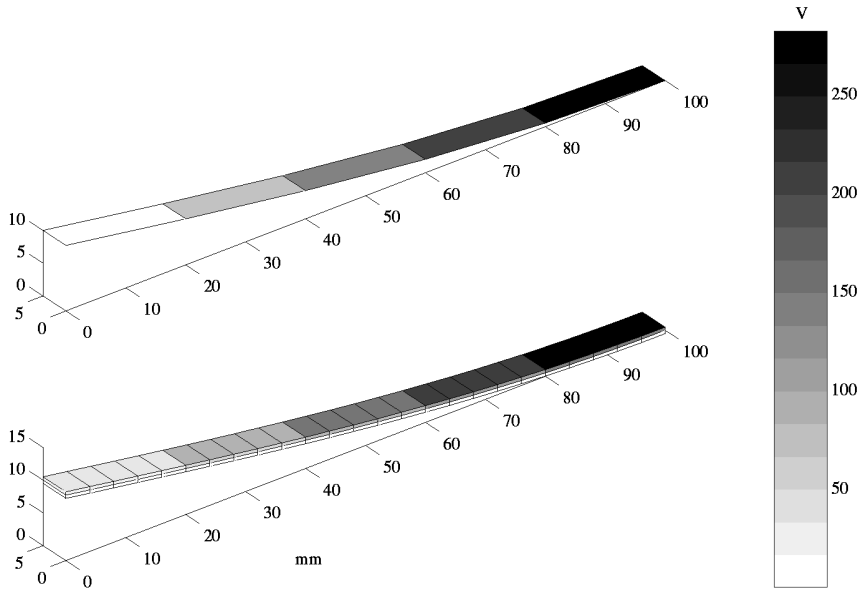

Figure 5.16: Comparison between shell and volume solutions

5.2.2 C-blocks

Commonly used piezoelectric actuators produce either high forces coupled with small deflections (stacks) or large deflections coupled with low forces (bimorph). To fill the gap between these two types of actuators, a curved piezoelectric bender actuator has been recently proposed: the C-block (Moskalik & Brei, 1997). It consists in a semi-circular ring shell clamped at the

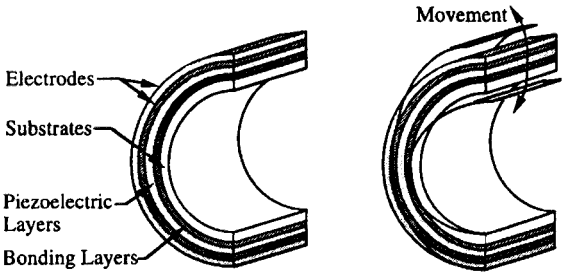

Figure 5.17: C-block actuator

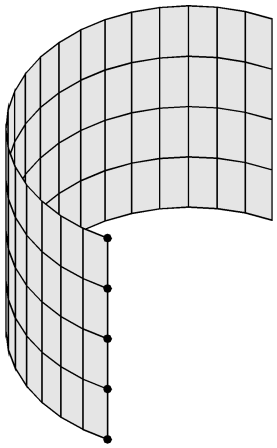

Figure 5.18: *FE* mesh

bottom edge (Fig.5.17). Three configurations are considered: one piezoelectric layer (*PVDF* film, $d_{31} = 2.3\ 10^{11}$ m/V) bonded to a substrate layer, two piezoelectric layers and four piezoelectric layers bonded together. The curved shells are 22 mm wide and have a radius to the neutral axis R_n respectively equal to 14.3 mm, 13.6 mm and 14.9 mm. The properties of the materials are summarized in Table 5.4.

Layers	Width (mm)	Thickness (μm)	Young Modulus (MPa)
PVDF	22	52	2900
Electrode	17.5	6.5	700
Substrate	20	25	6500
Bonding	22	25	1900

Table 5.4: Materials properties

In this study, they are modelled using a 4×20 mesh (Fig.5.18) of quadrangular multilayer piezoelectric elements. The comparison between *FE* prediction results and the analytical and experimental results from Moskalik & Brei for the three configurations is shown on Fig.5.19. The load consists of a static voltage applied across the electrodes of each piezoelectric layer (-400 V to $+400$ V). The tip deflection of the actuator with respect to the applied voltage is considered.

The theoretical model used by Moskalik & Brei is based on a *Bernoulli-Euler* beam formulation and the *Hamilton*'s principle and neglects the membrane load term (small compared to the bending moment term).

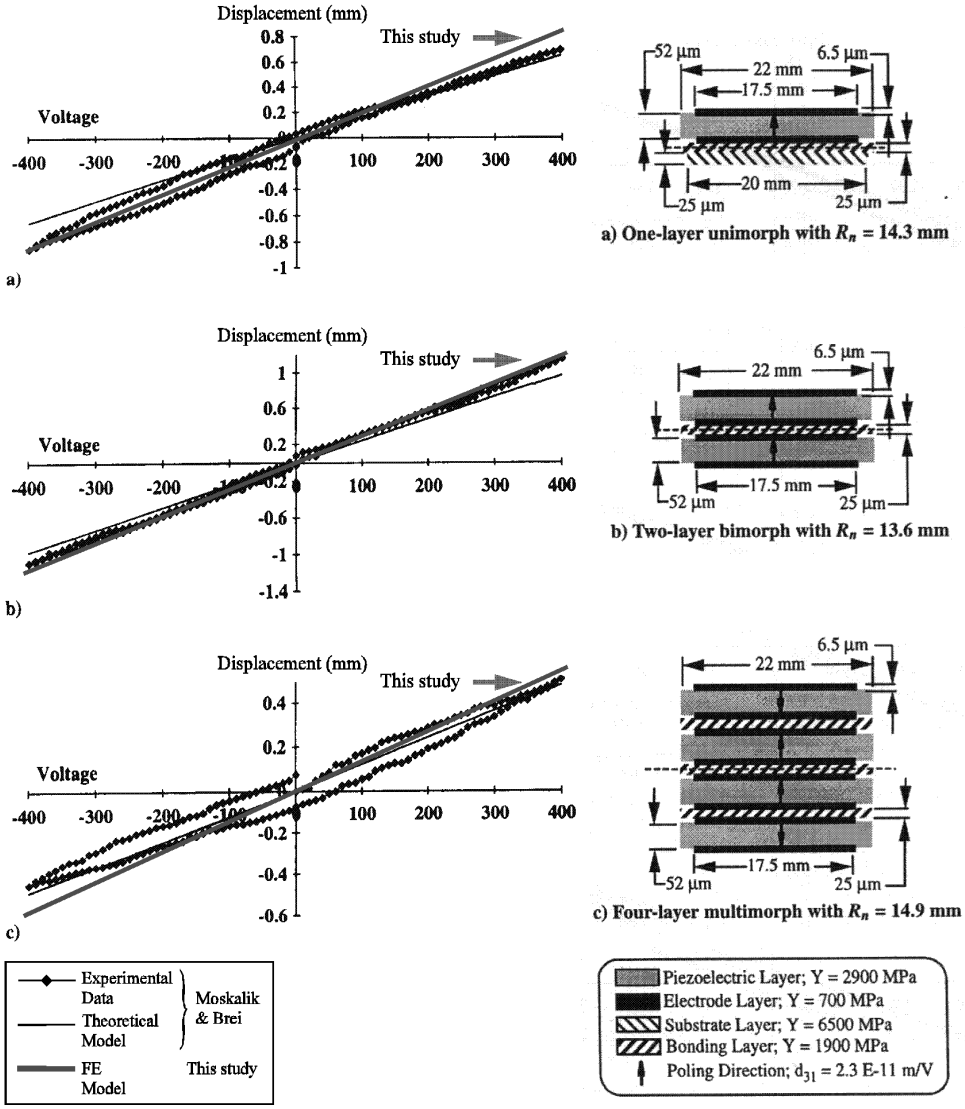

Figure 5.19: C-block results:

5.2.3 Membrane effects on nearly colocated control systems

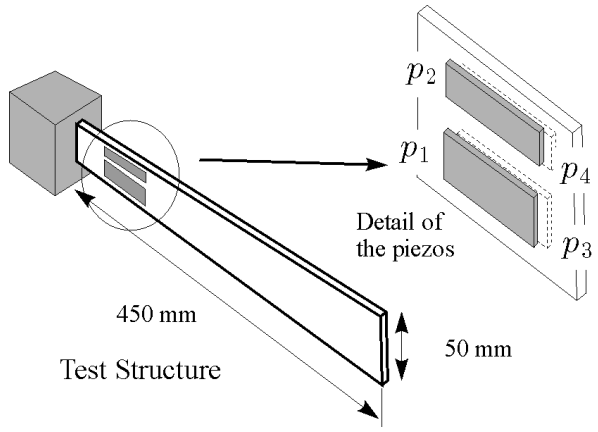

Figure 5.20: Cantilever plate with piezoceramics: experimental setup

In order to resolve the technological issues related to the practical realisation of a nearly colocated actuator/sensor system using bonded piezoceramics, a simple cantilever plate was used. Important differences in the experimental frequency response functions for similar actuator/sensor positions appeared. Consider the cantilever plate represented on Fig.5.20; the steel plate is 0.5 mm thick and four piezoceramic strips of 250 μm thickness are bounded symmetrically as indicated in the figure, 15 mm from the clamp. The material properties are summarized in Table 5.5. The size of the piezos is respectively 55 mm×25 mm for p_1 and p_3, and 55 mm×12.5 mm for p_2 and p_4. p_1 is used as actuator while the sensor is taken successively as p_2, p_3 and p_4. The experimental frequency response functions between a voltage applied to p_1 and the electric charge appearing successively on p_2, p_3 and p_4 when they are connected to a charge amplifier are shown on Fig.5.21.

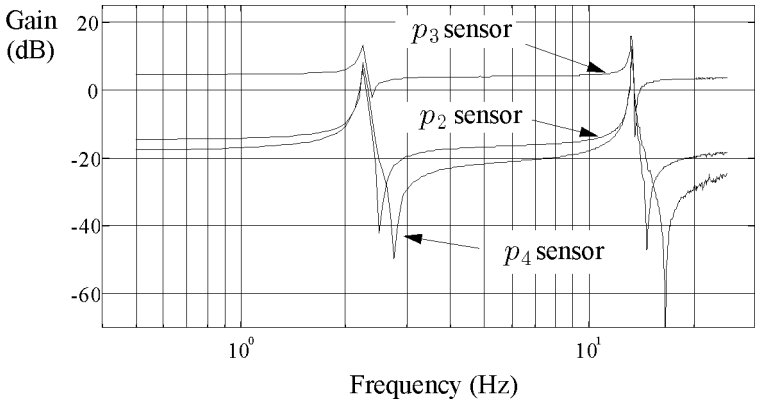

Figure 5.21: Experimental results: frequency response functions between p_1 and p_i

We note that the frequency response functions, particularly the location of the zeros, vary substantially from one configuration to the other. This is because the frequency response functions of nearly colocated control systems are very much dependent on local effects, in particular the

membrane strain in the thin steel plate between the piezo patches. This can only be accounted for by finite elements.

E_{steel}	210	(GPa)
ν_{steel}	0.3	
ρ_{steel}	7800	(kg/m^3)
E_{piezo}	65	(GPa)
ν_{piezo}	0.3	
ρ_{piezo}	7800	(kg/m^3)
ε_r	2600	
ε_0	$8.854.10^{-12}$	(F/m)
$d_{31} = d_{32}$	205.10^{-12}	(m/V)

Table 5.5: Materials properties

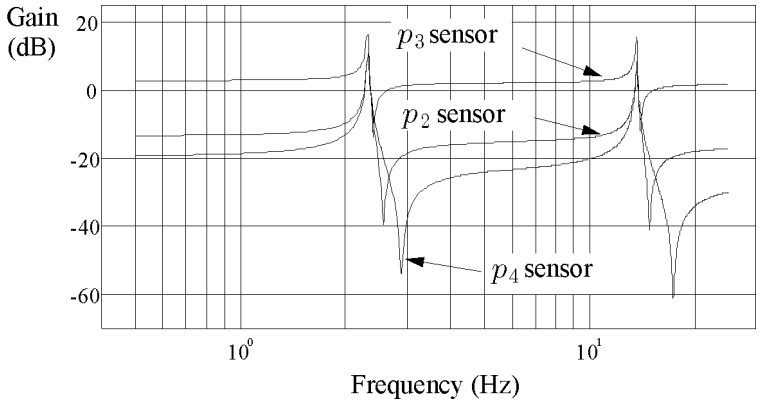

Figure 5.22: Simulation results: frequency response functions between p_1 and p_i

Figure 5.22 shows the numerical results corresponding to the three sensor configurations (a modal damping ratio of $\xi = 0.5\%$ was assumed in the numerical simulations); they agree reasonably well with the experiments, in particular for what concerns the location of the zeros. The study was conducted with the three meshes of Figure 5.23. Surprisingly, no significant difference appears in the frequency response functions which are almost identical; this can be further assessed from Table 5.6 which compares the frequency difference between the poles and zeros of the configuration (p_1/p_3) for the three meshes.

	$\Delta\omega_1/\omega_1$	$\Delta\omega_2/\omega_2$
Mesh 1	0.0340	0.0618
Mesh 2	0.0340	0.0610
Mesh 3	0.0339	0.0614
Experiment	0.0455	0.0674

Table 5.6: Influence of the mesh on the separation between the poles and the zeros for the configuration (p_1/p_3)

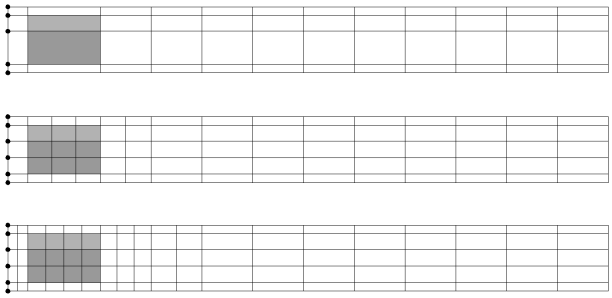

Figure 5.23: *FE* meshes

5.3 Vibroacoustics

This section illustrates the situation of shell structures with embedded piezoelectric actuators and sensors where they are nearly colocated. It, once again, stresses the importance of membrane components on the zeros of the frequency response function and suggests means of improving the performance when anisotropic piezoelectric material is used. The use of array sensors for modal filtering and volume velocity sensing is also considered.

5.3.1 *ASAC* plate

The *ASAC* plate[1](Active Structural Acoustical Control) is a volume velocity control device based on the principle of the *QWSIS* sensor (See §3.3.2) . The QWSIS sensor is based on the discretization of the plate sensor into narrow *strips* of width Δ (Fig.5.24); each strip is considered as a beam covered with piezoelectric material with quadratically shaped electrodes.

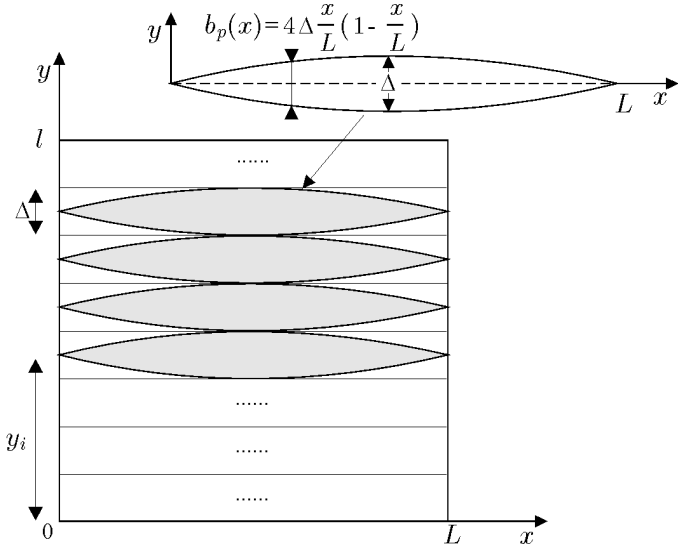

Figure 5.24: Discretisation of the active plate into narrow quadratic devices

[1]The ASAC panel was developed and built under the Research Project *DAFNOR*

The *ASAC* plate is covered on both side with piezoelectric material; the quadratic shaping of the electrodes does not only provide a volume velocity sensor, but also a uniform pressure actuator as a consequence of the duality of actuation and sensing properties of piezoelectric devices.

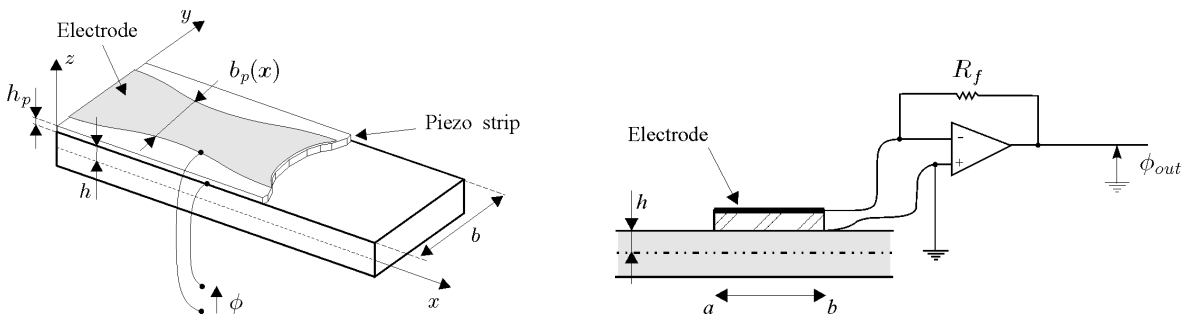

(a) Piezoelectric film on a beam structure

(b) Current amplifier

Figure 5.25: Piezoelectric beam device

For a piezoelectric beam sensor of quadratic shape, the output signal of a current amplifier (Fig.5.25(b)) is proportional to the volume velocity of the beam (Eq.(3.42), §3.3.2):

$$\phi_{out}(t) = -8e_{31}R_f\frac{h}{L^2}\int_0^L \dot{w}(x)\,dx \div V_{vol}$$

Similarly, a beam actuator with an electrode of quadratic shape is equivalent to a uniform distributed load acting along the beam (See Eq.(3.7)).

$$F_0 = e_{31}\phi\, b_p''(x)\, h$$

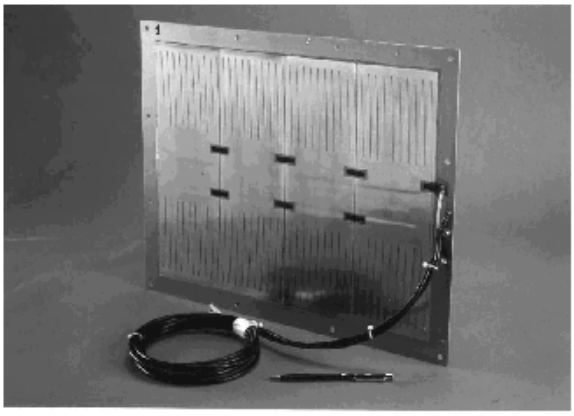

Figure 5.26: *ASAC* experimental setup

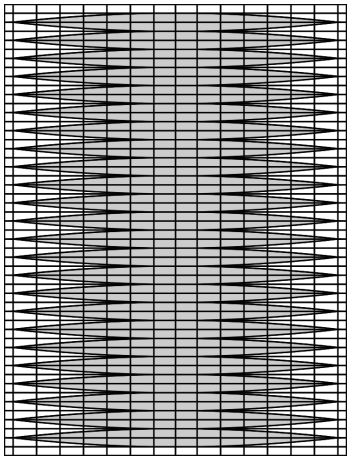

Figure 5.27: *FE* mesh

The main idea behind the *ASAC* panel is to realize a perfectly colocated actuator/sensor pair to control the volume velocity. The control system consists in a clamped 1 mm thick plate of

aluminium (420 mm×320 mm) covered on both sides with 0.5 mm thick piezoelectric *PVDF* films (400 mm×300 mm). For the actual laboratory model (Fig.5.26) the actuation and sensing layer electrodes consist of 24 strips. The material properties are summarized in Table 5.7. The direction of smaller piezoelectric coupling coefficient (e_{32}) is perpendicular to the strips. The finite element mesh is shown on Fig.5.27.

Aluminium		
Y	71	(GPa)
ν	0.3	
ρ	2800	(kg/m^3)
PVDF		
Y	2.7	(GPa)
ν	0.29	
ρ	1800	(kg/m^3)
d_{31}	1.8 10^{-11}	(Cb/N)
d_{32}	0.3 10^{-11}	(Cb/N)
ε_r	2600	

Table 5.7: Material properties

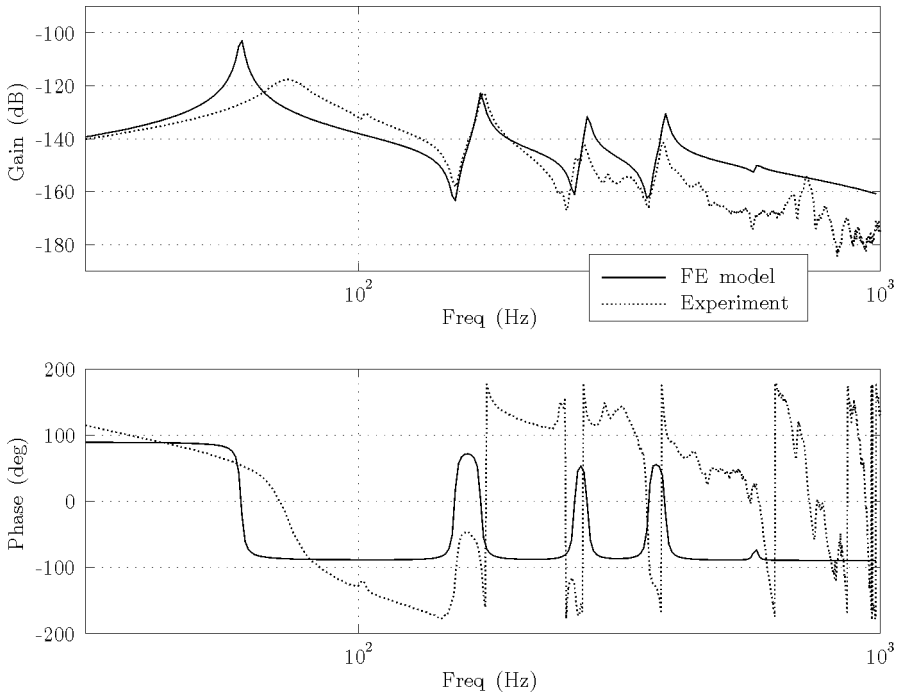

Figure 5.28: *ASAC* plate: Sensing

Figure 5.28 shows the comparison between the experiment[2] and the *FE* analysis for the plate used as a volume velocity sensor; the frequency response function between an incident sound pressure (provided by a loudspeaker in the experiment and assumed to be a uniform pressure in

[2]Experimental datas kindly provided by Kris Henrioulle (KUL-PMA)

the *FE* analysis) and the volume velocity sensor signal is represented.

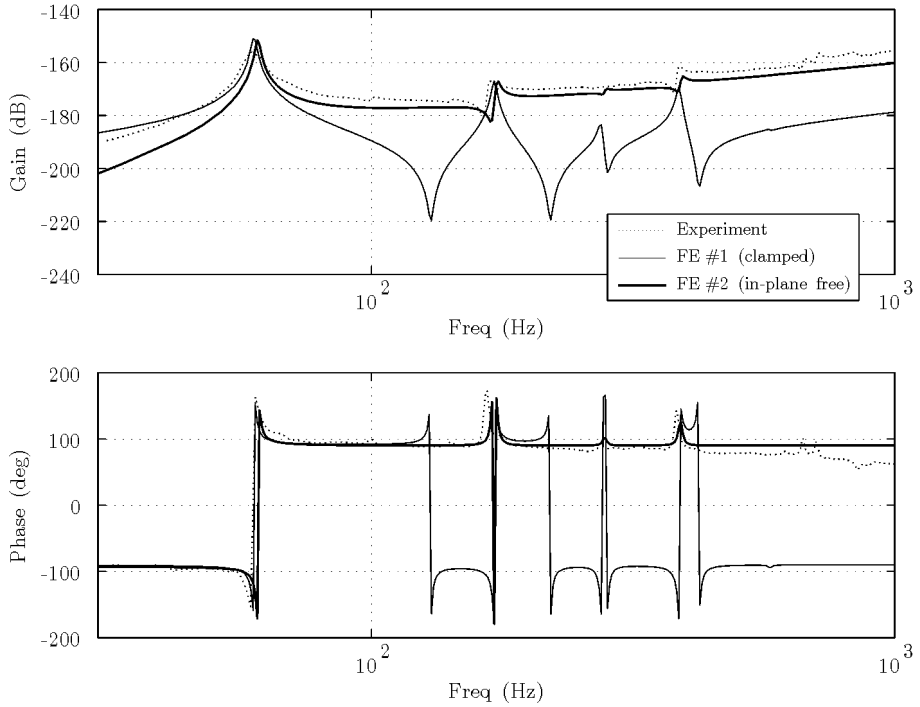

Figure 5.29: Open loop frequency response functions of the *ASAC* plate

The panel was next considered as a control device; the open-loop frequency response function between actuator and sensor was determined experimentally[2] and is shown on Fig.5.29 (dotted lines). Since the performance of the control system is to a large extend related to the distance between the poles and the zeros of the open-loop frequency response function, these results were considered as disappointing, contrary to simplified analytical predictions which indicated far better performances (Gardonio et al., 1999). At first, this lack of performance was attributed to imperfect alignment of top and bottom layers (non colocated actuator/sensor pair) or to an electrical coupling due to the wiring.

In fact, the finite element based simulations have shown that this lack of controllability is actually due to local membrane effects (Piefort & Henrioulle, 2000), neglected in the first analytical models together with the static contribution of the unmodelled high frequency modes (also called *residual mode*) (See §4.8 and Preumont (1997), Chap. 2).

In a first attempt to model the open-loop frequency response function of the *ASAC* panel using finite elements, the agreement of results with the experiment was rather unsatisfactory (Fig.5.29, FE #1). It appeared soon that the boundary conditions were not those of a clamped plate: in the actual experiment, the plate was almost free to move in its plane. The in-plane movement of the plate results in an even stronger influence of the membrane components and, therefore, in a stronger in-plane mechanical coupling between actuator and sensor. This induces an important *feedthrough* term in the frequency response function: a substantial part of the strain induced by the actuator induces directly membrane strain in the sensor, without contributing to the transverse displacement which produces the volume velocity (useful control). The frequency

response function of (Fig.5.29, FE #2) was obtained by freeing the in-plane movement of the plate in the finite element model; it shows a very good agreement with the experimental result.

The influence of the residual mode on the open-loop frequency response function is illustrated on Fig.5.30 for the two considered boundary conditions above (*perfect clamp* and *in-plane free*). The first twenty eigenmodes were extracted from the dynamic analysis and taken into account for the state space representation. The influence of the residual mode is independent of the frequency and introduces an important feedthrough component in the frequency response function. By not taking it into account, the in-plane coupling is almost completely washed out (because in-plane vibration modes are quite higher in frequency, outside the bandwidth, and therefore unmodelled) leading to an incorrect prediction of the control system performances.

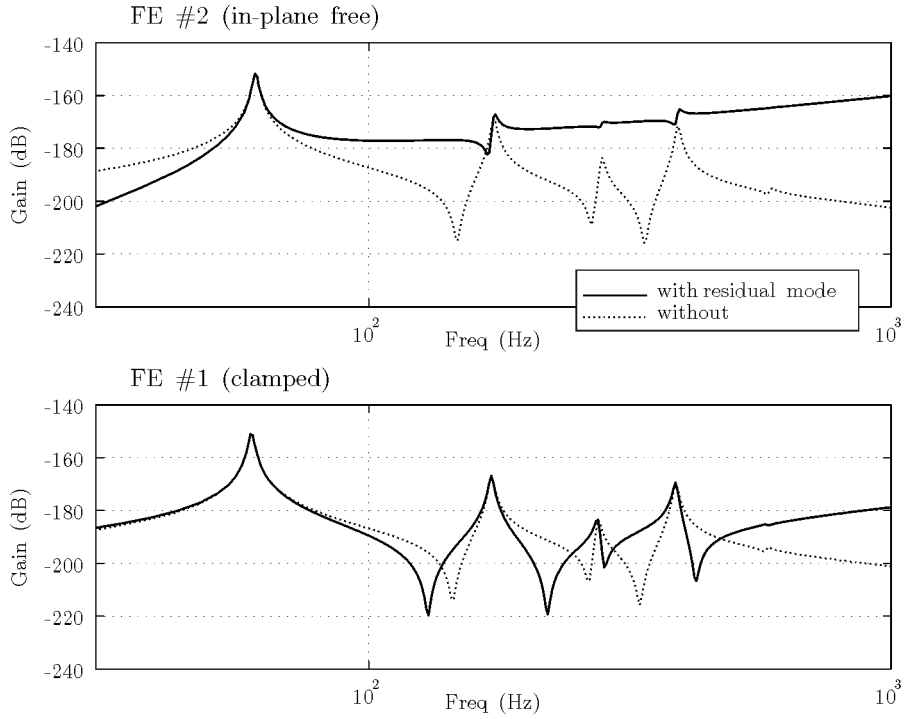

Figure 5.30: Effect of the residual mode (in addition to the 20 modelled modes) on the predicted open-loop frequency response functions

Note that, in the current design, the in-plane coupling is particularly strong because the direction of higher piezoelectric effect ($e_{31} \gg e_{32}$) for the sensor and the actuator are parallel; the most important strain is induced in a direction parallel to the direction of the strips and the sensor has the highest sensitivity to the strain in the direction of the strips. The actuation and sensing strips being layed in the same direction for the *ASAC* plate, it is in the worst possible configuration. However, for the actuator and the sensor taken separately, the direction of the strips has no influence on their characteristics. From this observation, the idea raised that the feedthrough component could be substantially reduced by using sensor and actuator strips perpendicular to each other.

5.3.2 Alternative *cross-ply* design of the *ASAC* plate

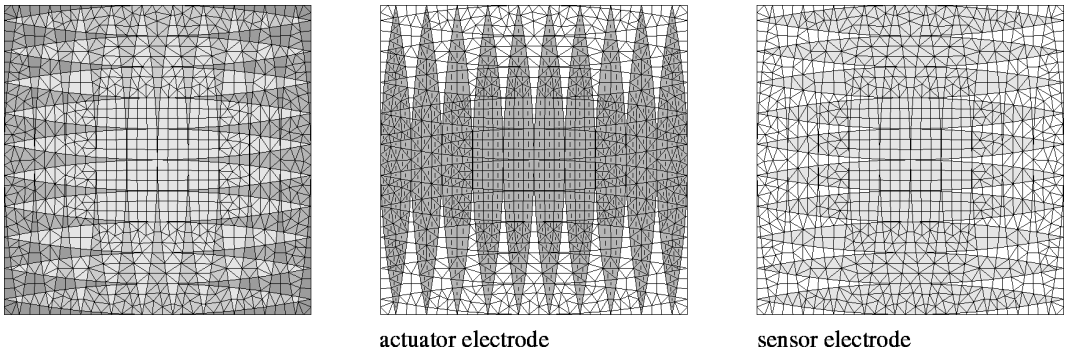

Figure 5.31: *FE* mesh

In the current design, the in-plane strain induced by a voltage ϕ in the direction of the highest sensitivity of the sensor (e_{31}) is directly related to $e_{31}\phi$ while the in-plane strain induced in the direction of the lowest sensitivity of the sensor (e_{32}) is directly related to $e_{32}\phi$; neglecting the *Poisson* effect, we have a feedthrough factor related to $e_{31}^2 + e_{32}^2$. In a *cross-ply* design, this feedthrough factor would be related to $2e_{31}e_{32}$; assuming a piezoelectric anisotropy ratio χ ($e_{32} = \chi e_{31}$), an in-plane feedthrough term reduction of about $2\chi/(1+\chi^2)$ can be expected, which may be substantial for small χ ($\chi = 0.2$ is a common typical value).

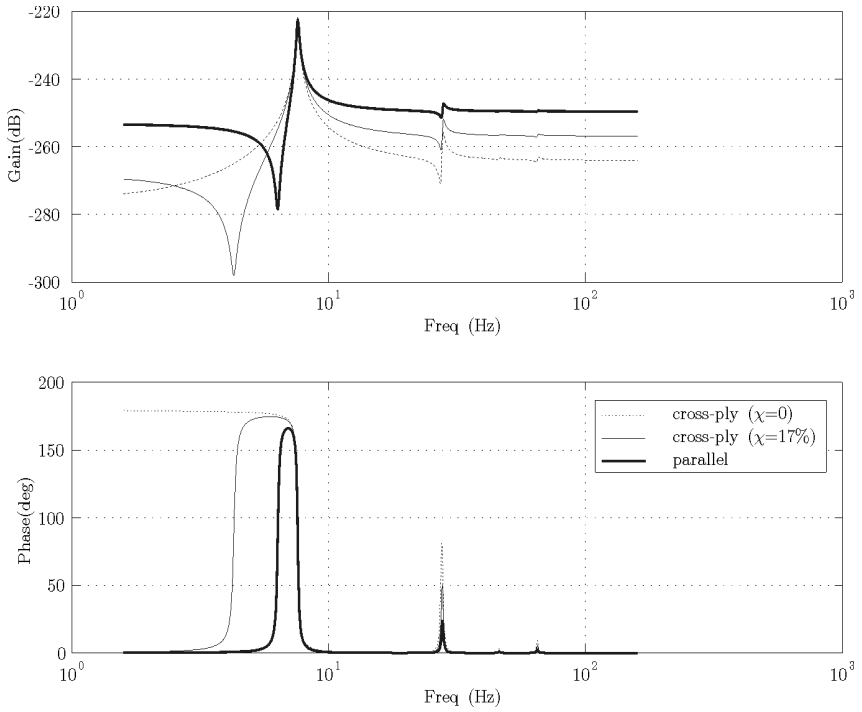

Figure 5.32: Open-loop frequency response functions

By using sensor strips perpendicular to the actuator strips, the control device would then exhibit a *cross-ply* actuator/sensor architecture and the in-plane feedthrough term would be greatly

reduced. The *FE*-based tools allow to modelize such architectures quite easily and to extract the corresponding frequency response functions to verify if this alternative is any better. The mesh used is represented on Fig.5.31; the sensor electrode forms a right angle with the actuator electrode. The comparison of the frequency response functions between the voltage applied to the actuator layer and the charge measured on the sensor layer for the *parallel* and *cross-ply* architectures for two piezoelectric anisotropy ratios are represented on Fig.5.32.

Indeed, the distance between the poles and zeros of the frequency response function is much larger for the cross-ply configuration, as compared to the parallel configuration, and the distance increases when the piezoelectric anisotropy ratio χ of the material decreases. As a result, improved closed-loop performances may be expected from the cross-ply design.

5.3.3 Array sensor

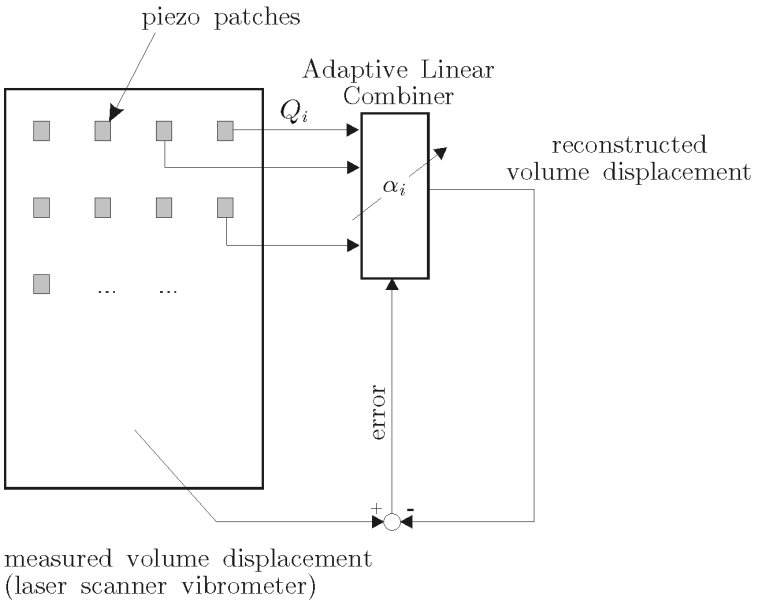

Figure 5.33: Principle of the volume displacement sensor

A noise radiation sensor consisting of an array of independent piezoelectric patches connected to an adaptive linear combiner was proposed (Preumont et al., 1999); the piezoelectric patches are located at the nodes of a rectangular mesh. The electric charges Q_i induced on the various patches by the plate vibration are the independent inputs of a multiple input adaptive linear combiner (Fig.5.33). The coefficients α_i of the linear combiner are adapted in such a way that the mean-square error between the reconstructed volume displacement (or velocity) and either numerical or experimental data is minimized. It must be noted that the same array sensor can also be used as modal filter by suitably adapting the coefficients α_i of the linear combiner.

This strategy can be used for reconstructing the volume displacement of a baffled plate with arbitrary boundary conditions. If the piezoelectric patches are connected to current amplifiers instead of charge amplifiers, the output signal becomes the volume velocity instead of the volume displacement.

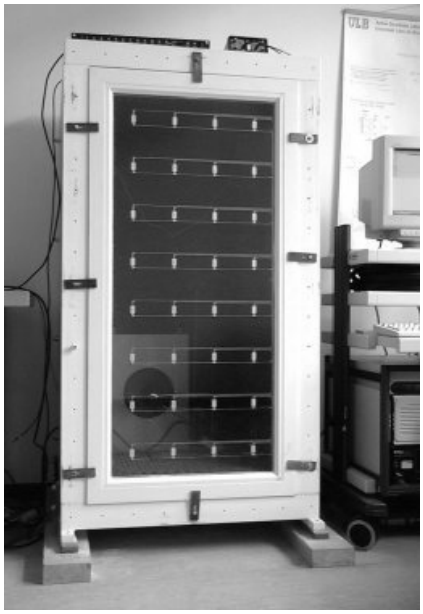

Figure 5.34: Array sensor: experimental setup

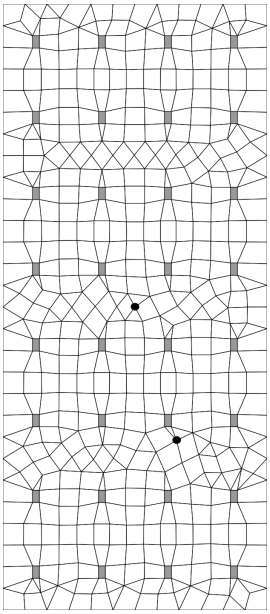

Figure 5.35: *FE* mesh

The laboratory demonstration model (Fig.5.34) consists in a glass plate (54 cm×124 cm, 4 mm thick) mounted in a standard window fitting and covered with an array of 4 by 8 piezoelectric patches (*PZT* piezoceramics - 13.75 mm×25 mm, 0.25 mm thick). The materials properties are summarized in Table 5.8.

Glass plate		
Y	72	(GPa)
ν	0.22	
ρ	2500	(kg/m^3)
PZT		
Y	69	(GPa)
ν	0.3	
ρ	7800	(kg/m^3)
d_{31}	205 10^{-12}	(Cb/N)
d_{32}	205 10^{-12}	(Cb/N)
ε_r	2600	

Table 5.8: Material properties

The finite element mesh used for the numerical analysis is shown on Fig.5.35. The first thirty eigenmodes were extracted from the dynamic analysis and taken into account for the state space representation. We used the opportunity given by the scanner laser vibrometer to measure the velocity of an array of points over the glass plate to deduce the volume velocity. The excitation used was provided by two shakers actuating the plate directly. Figure 5.36 shows the comparison between the frequency response functions between the excitation of Shaker #1 (in the center of the glass plate) and, respectively, sensors #7, #14 and the volume velocity obtained by finite

element analysis and experimentally.

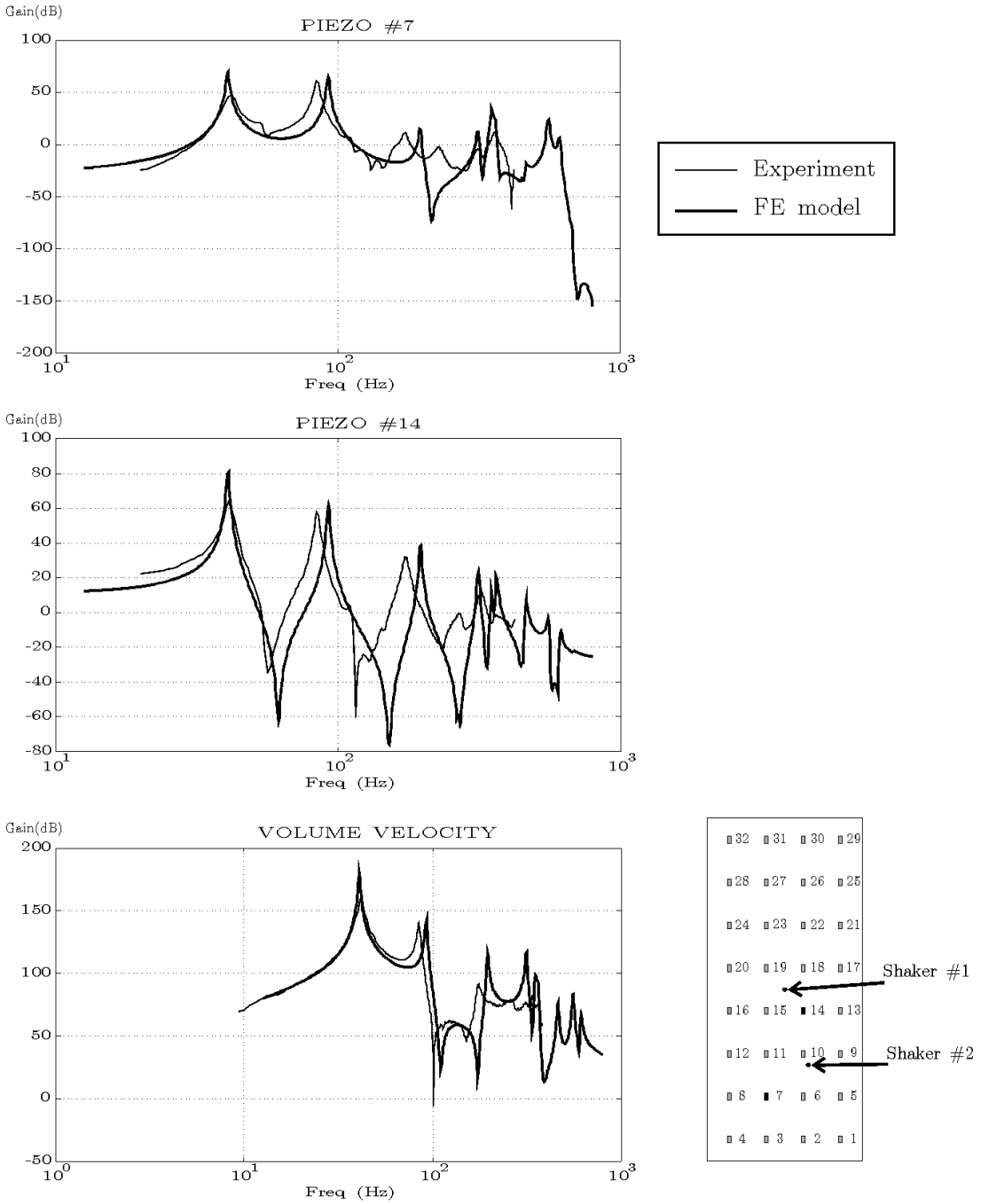

Figure 5.36: Frequency response functions /Shaker #1

5.4 Design against fatigue

Fatigue damage is one of the most frequent form of failure of metallic structures. With the increasing demand for high performance structures, the fatigue damage has become more and more important, in particular for metallic structures subjected to complex multiaxial loads due to random vibrations.

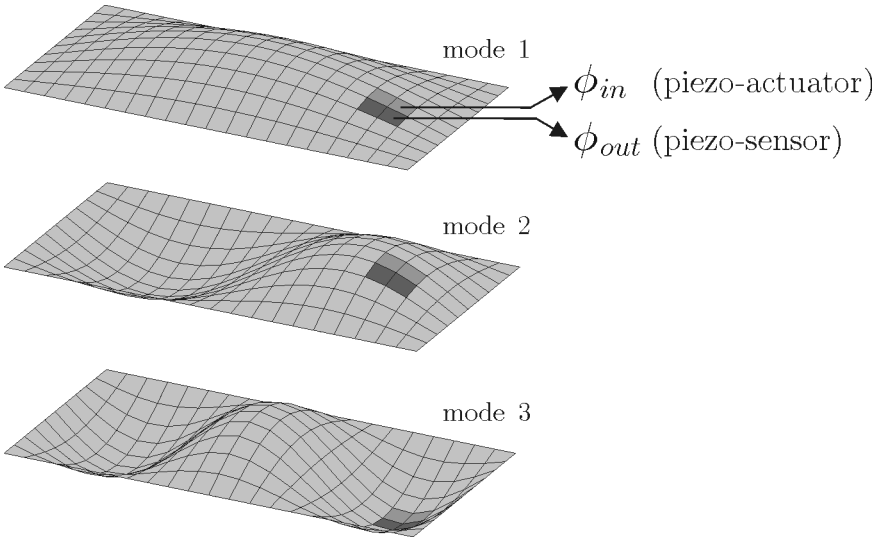

Figure 5.37: Piezoelectric elements location and first vibration modes

The active damping can be considered as a solution to reduce the vibrations level and at the same time, reduce the weight and increase the fatigue lifetime of such structures. Simulation tools allowing the designer to include directly piezoelectric actuators and sensors in a finite-element model have been developed as well as a *multiaxial random fatigue matlab toolbox* (Pitoiset et al., 1998; Pitoiset & Preumont, 2000; Pitoiset, 2001) allowing the direct assessment of the fatigue lifetime of a structure from a spectral analysis.

The quantification of the damage reduction that can be achieved thanks to an active damping can then be performed very easily, directly from a modal and a spectral analysis with finite-elements. This has been done on a simple example: A simply supported rectangular steel plate (15.24 cm×30.48 cm×0.813 mm) is considered. It is subjected to a band limited white noise random pressure field with perfect spatial coherence; Its *PSD* (Power Spectral Density) is $\Psi_{pp}(\omega) = 400$ Pa^2/rad/s between 0 Hz and 1000 Hz. The first three vibration modes are within the bandwidth of excitation. A piezoelectric actuator and a piezoelectric sensor (*PZT* 15.24 cm×30.48 mm×0.2 mm) are bonded to the surface as shown on Fig.5.37.

The *multiaxial random fatigue matlab toolbox* was used after a *FE* spectral analysis to evaluate the fatigue damage ratio (per second) over the plate. The state space form of the system is built under *Matlab* directly from the results of a *FE* modal analysis. A controller is designed using *Matlab* functionalities, in this case: a *PPF* tuned on the first mode (Positive Position Feedback).

The new modal damping ratios and eigen frequencies can be used in the *multiaxial random fatigue matlab toolbox* to evaluate the fatigue damage ratio over the controlled plate. The

comparison between damage maps for the plate without and with active damping is shown on Fig.5.38. The same comparison for the *PSD* of the stress components in an element in the center of the plate are shown on Fig.5.39.

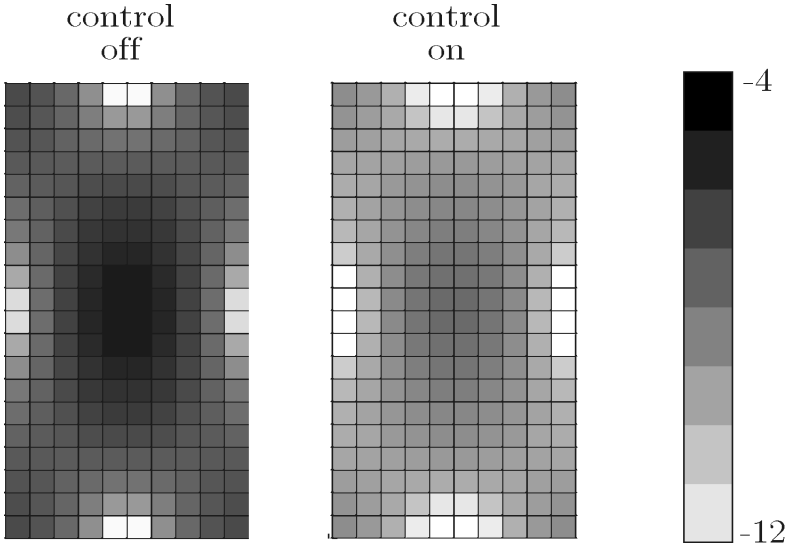

Figure 5.38: Damage map (Von Mises) with and without control (Log Scale)

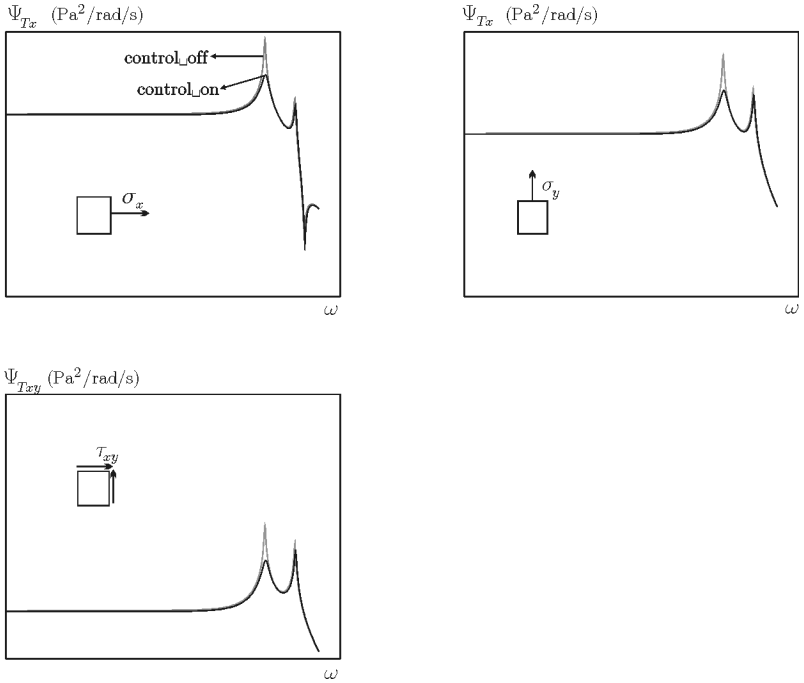

Figure 5.39: *PSD* of the stress components in the center of the plate with and without control

Chapter 6

Conclusions

After an historical overview of piezoelectricity, some general considerations about common piezoelectric materials and other smart materials have been presented in Chapter 1.

In Chapter 2, the piezoelectric constitutive equations were first introduced with a unidimensional example using an electromagnetic approach. The general thermopiezoelectric constitutive equations were then established starting from the thermodynamic principles and simplified for a *Kirchhoff* laminate embedding piezoelectric layers.

Various piezoelectric actuation and sensing mechanisms have been investigated in Chapter 3. The pure bending beam model has been generalized to the piezo-isotropic shell. The reciprocity between actuation and sensing has been stressed.

After a short review of finite element modelling of structures embedding piezoelectric devices, a finite element formulation for an electromechanically coupled piezoelectric structure starting from the constitutive equations has been presented in Chapter 4. The particular case of piezolaminated shells has been adressed. General multilayered piezoelectric shell elements have been succesfully integrated into the finite element package *Samcef* (*Samtech s.a.*). Volume elements have also been implemented. A method to extract a state space model of a piezoelectric input/output system from the modal finite element analysis of the structure has been presented.

Numerous applications of the developed tools in structure embedded actuation and sensing and in vibration and vibroacoustic control have been described in Chapter 5 and shown that good performances are achieved. The importance of the in-plane components in the open-loop frequency response functions has been illustrated. More complex modes of piezoelectric actuation/sensing can be modelled using volume elements; it is illustrated with the modelling of a shear bender.

Original aspects of this study:

- a full implementation of a library of piezoelectric elements (triangular and rectangular shells, brick, prism and tetrahedron volume elements) in a commercial finite element package is now available (*Samcef* V8.1-4, October 2000) and is suitable for industrial problems resolution.
- the equivalent loads approach has been extended to electrodes of arbitrary contour; the

strong duality between actuation and sensing properties of piezoelectric devices has been further assessed.

- the influence of the membrane component on the location of the zeros of the frequency response functions of colocated piezoelectric control systems has been extensively illustrated.
- the tools developed allowed an accurate modelling of the $ASAC$ panel, a better understanding of the different physical phenomenons involved has been gained; this allowed to explain the poor performances of the setup and to propose and test numerically an alternative design.
- the developed software tool has been applied to several ongoing research projects at the Active Structures Laboratory, namely the design and simulation of array vibroacoustics sensors and the reduction of fatigue damage through active damping.

Appendix A

Transverse shear in beams and plates

A.1 Beams

In this section, a theory for plane bending of beams is presented (Batoz & Dhatt, 1990). The influence of transverse shear strain is taken into account. This model, based on the plane sections hypothesis, is often referred to as *Timoshenko*'s model. It is the generalization of more classical models neglecting transverse shear strain and generally referred to as *Bernoulli-Euler* models. It can also be seen as the unidimensional version of the plates and shells model known as *Reissner-Mindlin* model presented in section A.2. It is a first order theory, the displacement being, at most, linear over the thickness.

A.1.1 Geometry and kinematics

A beam is a solid of which two dimensions (directions y, z) are small compared to the other (direction x, taken as reference) and the smallest curvature radius (see Fig.A.1). In this section, the following hypothesis are made:

Reference axis x is straight

the beam deforms in the xz plane (membrane, bending and shear)

Plane stress state ($\sigma_{zz} = 0$)

Efforts transmitted: normal force $N_x(x)$, shear force $\mathcal{T}_z(x)$ and bending moment $M_y(x)$. They will be referred to as N, $\mathcal{T}$ and M.

A.1.2 Constitutive equations

The stress-strain relationships are

$$\sigma(x,z) = Y\epsilon(x,z) \quad (A.1)$$

$$\tau(x,z) = G\gamma(x,z) \quad (A.2)$$

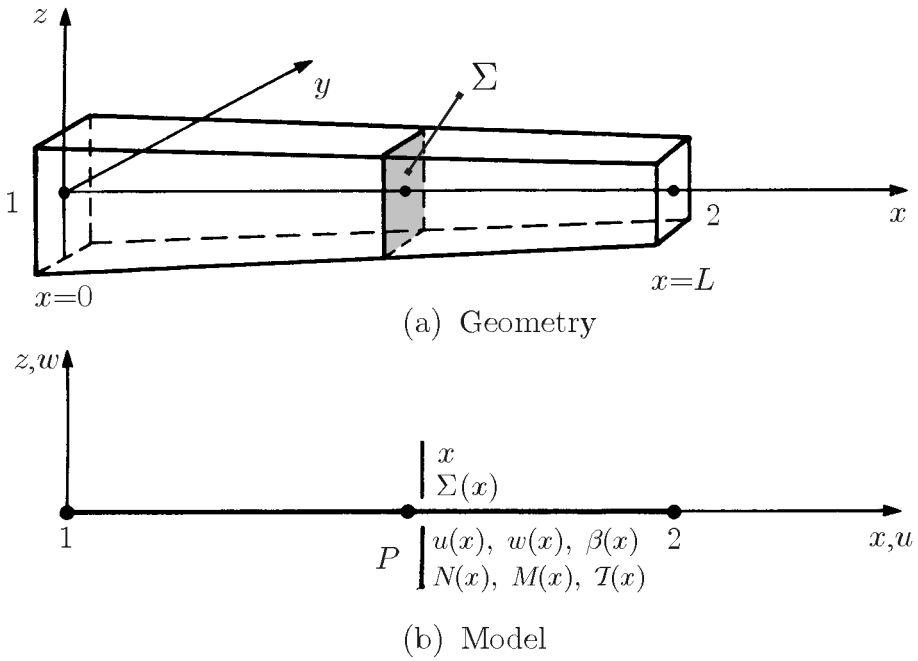

Figure A.1: Beam geometry

where Y and G are respectively the Young's modulus and the shear modulus and ϵ and γ are the axial and shear strain given respectively by

$$\epsilon = \frac{\partial u(x,z)}{\partial x} = u_{,x} \tag{A.3}$$

$$\gamma = \frac{\partial u(x,z)}{\partial z} + \frac{\partial w(x,z)}{\partial x} = u_{,z} + w_{,x} \tag{A.4}$$

Considering the plane section hypothesis (a plane section remains plane after deformation) also known as *Timoshenko* hypothesis, one gets the displacement field

$$u(x,z) = u(x) + z\beta(x) \tag{A.5}$$

$$w(x,z) = w(x) \tag{A.6}$$

where u, w, β are the small displacements between the initial and deformed configurations. Combining equations (A.3) to (A.6), one gets

$$\epsilon = \epsilon_0 + z\kappa \tag{A.7}$$

$$\gamma = \beta + w_{,x} \tag{A.8}$$

where

$\epsilon_0 = u_{,x}$ is the membrane strain,

γ the transverse shear strain,

$\kappa = \beta_{,x}$ the curvature,

$\beta(x)$ can be seen as the rotation of section pq (figure A.2), $z\kappa$ represents the bending strain, and $w_{,x}$ the rotation of the reference surface ($z = 0$)

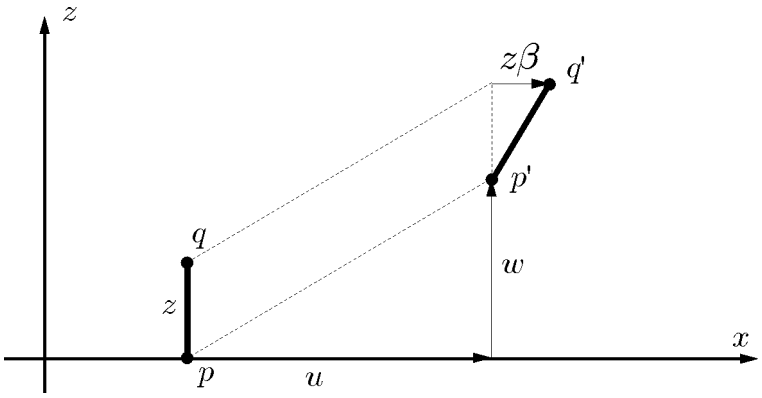

Figure A.2: Displacement of two points p and q

Upon integrating equations (A.1) and (A.2) over the cross-section, the resultant efforts N, M, and $\mathcal{T}$ read

$$N = \int_\Sigma \sigma \, d\Sigma = \int_\Sigma (Y\epsilon_0 + zY\kappa) \, d\Sigma = A\epsilon_0 + B\kappa \tag{A.9}$$

$$M = \int_\Sigma z\sigma \, d\Sigma = \int_\Sigma \left(zY\epsilon_0 + z^2 Y\kappa\right) \, d\Sigma = B\epsilon_0 + D\kappa \tag{A.10}$$

$$\mathcal{T} = \int_\Sigma \tau \, d\Sigma = K\gamma \tag{A.11}$$

where A, B and D, respectively the membrane, coupling and bending stiffnesses, are given by

$$A = \int_\Sigma Y(x,z) d\Sigma \tag{A.12}$$

$$B = \int_\Sigma zY(x,z) d\Sigma \tag{A.13}$$

$$D = \int_\Sigma z^2 Y(x,z) d\Sigma \tag{A.14}$$

and K is the transverse shear stiffness

$$K = \int_\Sigma G(x,z) d\Sigma \tag{A.15}$$

The transverse shear strain defined by (A.8) is constant over the thickness. Therefore, the transverse shear stress defined by (A.2) will not verify the boundary conditions on lower and upper skins (transverse shear stress must be zero on the external surfaces) and the local equilibrium

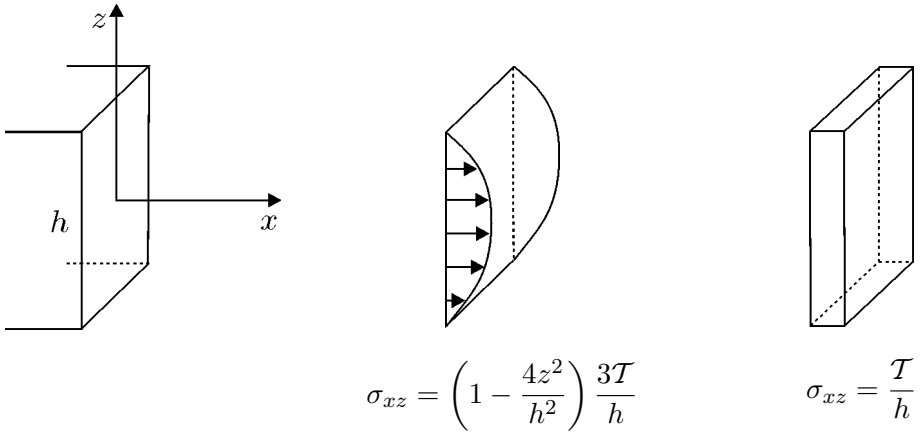

Figure A.3: Transverse shear stress distribution

relations in x. To illustrate this, a shear stress distribution in an isotropic rectangular section is represented on Fig.A.3.

Several propositions were made to determine a *shear stiffness* correction factor k such that

$$K = k\overline{K} \tag{A.16}$$

where $\overline{K}$ is the shear stiffness defined by equation (A.15).

Timoshenko proposed a correction factor based on the assumption that the value in the middle of a rectangular section should be correct $k = 2/3$

Reissner proposed a correction factor based on the equality of the strain energy $k = 5/6$

Mindlin, using a dynamic approach based on the natural frequencies equality, proposed $k = \pi^2/12$

A method to approximate the transverse shear stiffness for multilayered materials will be presented in §A.2.2.

A.2 Plates

In this section, the main concepts of a first order plate theory are presented (Hughes, 1987; Batoz & Dhatt, 1990). This theory, usually referred to as *Reissner-Mindlin* theory, is based on the plane section hypothesis and accounts for the transverse shear strain. It can be seen as a generalization of the more classical model neglecting the transverse shear strain based on the normal conservation hypothesis generally referred to as the *Kirchhoff* model of plates. The plane anisotropy is assumed: there is no coupling between membrane/bending deformations and transverse shear deformation.

A plate is a solid defined by a plane reference (xy) and a thickness $h(x, y)$, small compared to the other dimensions. The following hypothesis will be considered:

plane sections remain plane after deformation

plane stress state ($\sigma_{zz} = 0$)

there is no coupling between membrane/bending deformations and transverse shear deformation

the efforts transmitted are (figure A.4) the normal effort $\{N\} = \{N_x \ N_y \ N_{xy}\}^T$, the transverse shear $\{\mathcal{T}\} = \{\mathcal{T}_{xz} \ \mathcal{T}_{yz}\}^T$, the bending moment $\{M\} = \{M_x \ M_y \ M_{xy}\}^T$

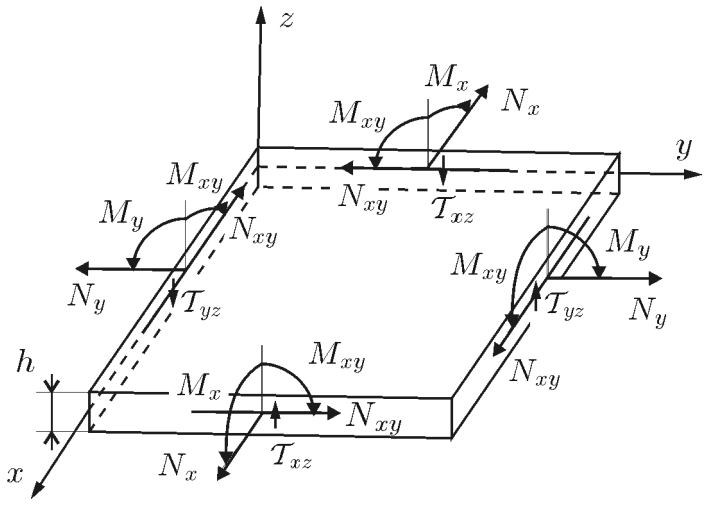

Figure A.4: Resultant efforts

A.2.1 Constitutive equations

Using standard engineering notations, the constitutive equations read

$$\left\{ \begin{array}{c} \sigma \\ \tau \end{array} \right\} = \left[\begin{array}{cc} [H_m] & 0 \\ 0 & [H_t] \end{array} \right] \left\{ \begin{array}{c} \epsilon \\ \gamma \end{array} \right\} \tag{A.17}$$

where

$[H_m]$ and $[H_t]$ are respectively the membrane/bending modulus matrix and the transverse shear modulus matrix

$$\{\sigma\} = \left\{ \begin{array}{c} \sigma_{xx} \\ \sigma_{yy} \\ \sigma_{xy} \end{array} \right\} \quad , \quad \{\tau\} = \left\{ \begin{array}{c} \sigma_{xz} \\ \sigma_{yz} \end{array} \right\} \tag{A.18}$$

$$\{\epsilon\} = \left\{ \begin{array}{c} \epsilon_{xx} \\ \epsilon_{yy} \\ 2\epsilon_{xy} \end{array} \right\} \quad , \quad \{\gamma\} = \left\{ \begin{array}{c} 2\epsilon_{xz} \\ 2\epsilon_{yz} \end{array} \right\} \tag{A.19}$$

$$\epsilon_{xx} = \frac{\partial u(x,y,z)}{\partial x} = u_{,x} \tag{A.20}$$

$$\epsilon_{yy} = \frac{\partial v(x,y,z)}{\partial y} = u_{,y} \tag{A.21}$$

$$2\epsilon_{xy} = \gamma_{xy} = \frac{\partial u(x,y,z)}{\partial y} + \frac{\partial v(x,y,z)}{\partial x} = u_{,y} + v_{,x} \tag{A.22}$$

$$2\epsilon_{xz} = \gamma_{xz} = \frac{\partial u(x,y,z)}{\partial z} + \frac{\partial w(x,y,z)}{\partial x} = u_{,z} + w_{,x} \tag{A.23}$$

$$2\epsilon_{yz} = \gamma_{yz} = \frac{\partial v(x,y,z)}{\partial z} + \frac{\partial w(x,y,z)}{\partial y} = v_{,z} + w_{,y} \tag{A.24}$$

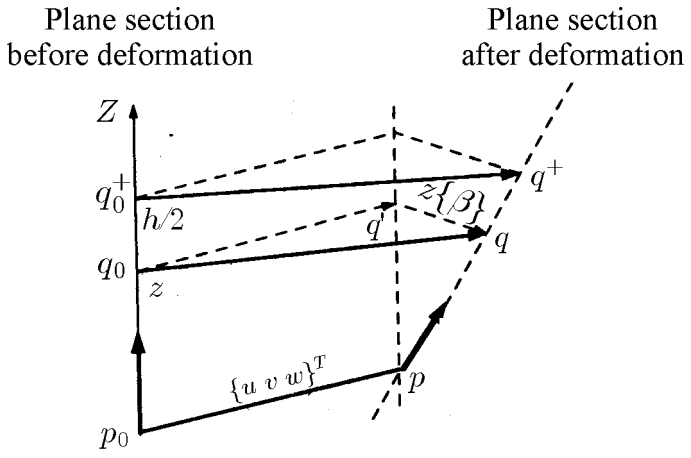

Figure A.5: Displacement of two points p and q

Considering the plane section hypothesis (*Mindlin*), the displacement field is given by

$$u(x,y,z) = u(x,y) + z\beta_x(x,y) \tag{A.25}$$

$$v(x,y,z) = v(x,y) + z\beta_y(x,y) \tag{A.26}$$

$$w(x,y,z) = w(x,y) \tag{A.27}$$

where u, v, w, β_x, β_y are the small displacements between the initial and deformed configurations. Linear strains read

$$\{\epsilon\} = \{\epsilon_0\} + z\{\kappa\} \tag{A.28}$$

$$\{\gamma\} = \left\{ \begin{array}{c} \gamma_{xz} \\ \gamma_{yz} \end{array} \right\} = \left\{ \begin{array}{c} \beta_x \\ \beta_y \end{array} \right\} + \left\{ \begin{array}{c} w_{,x} \\ w_{,y} \end{array} \right\} \tag{A.29}$$

where

$$\{\epsilon_0\} = \left\{ \begin{array}{c} u_{,x} \\ v_{,y} \\ u_{,y} + v_{,x} \end{array} \right\} \tag{A.30}$$

is the mid-plane membrane strain,

$$\{\kappa\} = \left\{ \begin{array}{c} \beta_{x,x} \\ \beta_{y,y} \\ \beta_{x,y} + \beta_{y,x} \end{array} \right\} \tag{A.31}$$

is the actual curvature, $z\{\kappa\}$ represents the bending strain and $w_{,x}$, $w_{,y}$ the rotations of the reference surface (mid-plane $z = 0$).

Developping the resultant efforts $\{N\}$ and $\{M\}$, and $\{\mathcal{T}\}$ one gets

$$\{N\} = \int_{-h/2}^{+h/2} \{\sigma\}\, dz = [A]\,\{\epsilon_0\} + [B]\,\{\kappa\} \tag{A.32}$$

$$\{M\} = \int_{-h/2}^{+h/2} \{\sigma\} z\, dz = [B]\,\{\epsilon_0\} + [D]\,\{\kappa\} \tag{A.33}$$

$$\{\mathcal{T}\} = \int_{-h/2}^{+h/2} \{\tau\}\, dz = [K]\,\{\gamma\} \tag{A.34}$$

where $[A]$, $[B]$ and $[D]$, respectively, the membrane, coupling and bending stiffness matrix are given by

$$[A] = \int_{-h/2}^{h/2} [H_m(x,z)]\, dz \tag{A.35}$$

$$[B] = \int_{-h/2}^{h/2} z\,[H_m(x,z)]\, dz \tag{A.36}$$

$$[D] = \int_{-h/2}^{h/2} z^2\,[H_m(x,z)]\, dz \tag{A.37}$$

and $[K]$ is the transverse shear stiffness matrix, which is discussed below

A.2.2 Transverse shear stiffness approximation

This method (Lardeur, 1990; Batoz & Dhatt, 1990; Jetteur, 1991), based on strain energy equivalence, matches the *Reissner* theory for homogeneous plates (shear stiffness correction factor $k = 5/6$). In the present theory, the following hypothesis are made:

there is no membrane/bending coupling: $[B] = 0$ (as encountered in a symmetric multi-layered material for example)

the transverse shear stiffness matrix $[K]$ will be defined in such a way that the strain energy density U_1 obtained with an *exact* distribution of shear stresses (according to the tridimensional equilibrium equations) is equivalent to the the strain energy density U_2 based on the *Reissner-Mindlin* hypothesis.

a) Strain energy U_1

$$U_1 = \frac{1}{2}\int_{-h/2}^{h/2} \{\tau\}^T [H_t]^{-1} \{\tau\} dz \tag{A.38}$$

b) Strain energy U_2

$$U_2 = \frac{1}{2}\{\mathcal{T}\}^T [K]^{-1} \{\mathcal{T}\} = \frac{1}{2}\{\gamma\}^T [K] \{\gamma\} \tag{A.39}$$

using Equ.(A.34).

To establish the expression for U_1, the distribution of the transverse shear stresses $\{\tau\}$ is required. This will be obtained by integrating the following tridimensional equilibrium equations (A.40) and (A.41) over the thickness of the plate.

$$\sigma_{xx,x} + \sigma_{xy,y} + \sigma_{xz,z} = 0 \tag{A.40}$$
$$\sigma_{xy,x} + \sigma_{yy,y} + \sigma_{yz,z} = 0 \tag{A.41}$$

One gets

$$\sigma_{xz} = -\int_{-h/2}^{z} (\sigma_{xx,x} + \sigma_{xy,y})\, dz \tag{A.42}$$
$$\sigma_{yz} = -\int_{-h/2}^{z} (\sigma_{xy,x} + \sigma_{yy,y})\, dz \tag{A.43}$$

with $\sigma_{xz} = \sigma_{yz} = 0$ in $z = \pm h/2$ (free surface boundary conditions).

In-plane stresses are written in relation to resultant efforts (equations (A.32) to (A.34)) assuming pure shear/bending deformation and no coupling between membrane deformation and bending ($[B] = 0$). The displacement field reads

$$u(x, y, z) = z\beta_x(x, y) \tag{A.44}$$
$$v(x, y, z) = z\beta_y(x, y) \tag{A.45}$$
$$w(x, y, z) = w(x, y) \tag{A.46}$$

so that in-plane strain and stresses become

$$\{\epsilon\} = z\{\kappa\} \tag{A.47}$$
$$\{\sigma\} = z[H_m]\{\kappa\} = z[H_m][D]^{-1}\{M\} \tag{A.48}$$
$$\Leftrightarrow \tag{A.49}$$
$$\{\sigma\} = z[\mathcal{A}]\{M\} \tag{A.50}$$

where

$$[\mathcal{A}] = [H_m][D]^{-1} \tag{A.51}$$

Using the tridimensional equilibrium equations (A.40) and (A.41), the equilibrium of in-plane moments can be written:

$$\int_{-h/2}^{h/2} z\left(\sigma_{xx,x} + \sigma_{xy,y} + \sigma_{xz,z}\right)\, dz = 0 \tag{A.52}$$
$$\int_{-h/2}^{h/2} z\left(\sigma_{xy,x} + \sigma_{yy,y} + \sigma_{yz,z}\right)\, dz = 0 \tag{A.53}$$
$$\Leftrightarrow$$
$$-\int_{-h/2}^{h/2} z\sigma_{xz,z}\, dz = M_{xx,x} + M_{xy,y} \tag{A.54}$$
$$-\int_{-h/2}^{h/2} z\sigma_{yz,z}\, dz = M_{xy,x} + M_{yy,y} \tag{A.55}$$

Integrating the first member of equations (A.54) and (A.55) by parts and assuming that $\sigma_{xz} = \sigma_{yz} = 0$ in $z = \pm h/2$ (free surface boundary conditions), one gets the global equilibrium relations for a plate:

$$\{\mathcal{T}\} = \left\{ \begin{array}{c} \mathcal{T}_{xz} \\ \mathcal{T}_{yz} \end{array} \right\} = \left\{ \begin{array}{c} M_{xx,x} + M_{xy,y} \\ M_{xy,x} + M_{yy,y} \end{array} \right\} \tag{A.56}$$

Using relation (A.50) in equations (A.42) and (A.43), the transverse shear stresses read

$$\begin{aligned} \sigma_{xz} = & -\int_{-h/2}^{z} z\left(\mathcal{A}_{11}M_{xx,x} + \mathcal{A}_{12}M_{yy,x} + \mathcal{A}_{13}M_{xy,x}\right. \\ & \left. + \mathcal{A}_{31}M_{xx,y} + \mathcal{A}_{32}M_{yy,y} + \mathcal{A}_{33}M_{xy,y}\right) dz \end{aligned} \tag{A.57}$$
$$\begin{aligned} \sigma_{yz} = & -\int_{-h/2}^{z} z\left(\mathcal{A}_{31}M_{xx,x} + \mathcal{A}_{32}M_{yy,x} + \mathcal{A}_{33}M_{xy,x}\right. \\ & \left. + \mathcal{A}_{11}M_{xx,y} + \mathcal{A}_{12}M_{yy,y} + \mathcal{A}_{13}M_{xy,y}\right) dz \end{aligned} \tag{A.58}$$

which can be rewritten in matrix form and using relation (A.56):

$$\{\tau\} = [\mathcal{D}_1]\{\mathcal{T}\} + [\mathcal{D}_2]\{\Lambda\} \tag{A.59}$$

where

$$\{\Lambda\} = \left\{ \begin{array}{cccc} M_{xx,x} - M_{xy,y} & M_{xy,x} - M_{yy,y} & M_{yy,x} & M_{xx,y} \end{array} \right\}^T \tag{A.60}$$

$$[\mathcal{D}_1] = -\int_{-h/2}^{z} \frac{z}{2} \left[\begin{array}{cc} \mathcal{A}_{11} + \mathcal{A}_{33} & \mathcal{A}_{13} + \mathcal{A}_{32} \\ \mathcal{A}_{31} + \mathcal{A}_{23} & \mathcal{A}_{22} + \mathcal{A}_{33} \end{array} \right] dz \tag{A.61}$$

$$[\mathcal{D}_2] = -\int_{-h/2}^{z} \frac{z}{2} \left[\begin{array}{cccc} \mathcal{A}_{11} - \mathcal{A}_{33} & \mathcal{A}_{13} - \mathcal{A}_{32} & 2\mathcal{A}_{12} & 2\mathcal{A}_{31} \\ \mathcal{A}_{31} - \mathcal{A}_{23} & \mathcal{A}_{22} - \mathcal{A}_{33} & 2\mathcal{A}_{32} & 2\mathcal{A}_{21} \end{array} \right] dz \tag{A.62}$$

Using equation (A.59) into expression (A.38), the strain energy U_1 can be written

$$U_1 = \frac{1}{2} \left\{ \begin{array}{c} \mathcal{T} \\ \Lambda \end{array} \right\}^T \left[\begin{array}{cc} [\mathcal{C}_{11}] & [\mathcal{C}_{12}] \\ [\mathcal{C}_{12}]^T & [\mathcal{C}_{22}] \end{array} \right] \left\{ \begin{array}{c} \mathcal{T} \\ \Lambda \end{array} \right\} \tag{A.63}$$

where

$$[\mathcal{C}_{11}] = -\int_{-h/2}^{h/2} [\mathcal{D}_1]^T [H_t]^{-1} [\mathcal{D}_1] \tag{A.64}$$

$$[\mathcal{C}_{22}] = -\int_{-h/2}^{h/2} [\mathcal{D}_2]^T [H_t]^{-1} [\mathcal{D}_2] \tag{A.65}$$

$$[\mathcal{C}_{12}] = -\int_{-h/2}^{h/2} [\mathcal{D}_1]^T [H_t]^{-1} [\mathcal{D}_2] \tag{A.66}$$

The equivalence between the two expressions of the transverse shear strain energy can be written

$$\frac{1}{2} \{\mathcal{T}\}^T [K]^{-1} \{\mathcal{T}\} = \frac{1}{2} \left\{ \begin{array}{c} \mathcal{T} \\ \Lambda \end{array} \right\}^T \left[\begin{array}{cc} [\mathcal{C}_{11}] & [\mathcal{C}_{12}] \\ [\mathcal{C}_{12}]^T & [\mathcal{C}_{22}] \end{array} \right] \left\{ \begin{array}{c} \mathcal{T} \\ \Lambda \end{array} \right\} \tag{A.67}$$

which leads to use

$$[K] = [\mathcal{C}_{11}]^{-1} \tag{A.68}$$

as an approximation of the transverse shear stiffness matrix

Appendix B

Longitudinal vibration of a piezoelectric bar

In order to emphasize the electromechanical coupling phenomenon, the natural frequencies (mechanical characteristics) of a unidirectional piezoelectric bar with different electrical boundary conditions is considered

Resonance frequency, $\phi = 0$ (closed circuit)

Antiresonance frequency, $I = 0$ (open circuit)

The equivalent form (2.37) of the constitutive equations (2.11) and (2.12) is

$$T = cS - h\,D \tag{B.1}$$
$$E = -hS + \beta\,D \tag{B.2}$$

Using the notations of Fig.B.1, and considering an harmonic displacement in the z direction $W(z)e^{i\omega t}$, the stress reads $T = \sigma$ and the strain $S = \partial W/\partial z$.

The system of equations to be solved is formed by

the constitutive equations (B.1) and (B.2)

$$\sigma = c\frac{\partial W}{\partial z} - hD \tag{B.3}$$

$$E = -h\frac{\partial W}{\partial z} + \beta D \tag{B.4}$$

the equation of motion (axial equilibrium of the bar)

$$\frac{\partial \sigma}{\partial z} = \rho\frac{\mathrm{d}^2 W}{\mathrm{d}t^2} = -\rho\omega^2 W \tag{B.5}$$

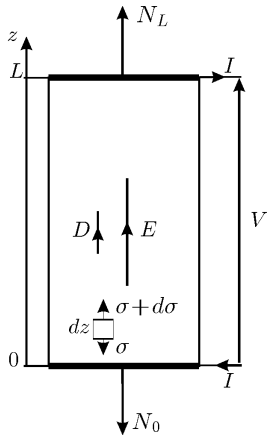

Figure B.1: Piezoelectric unidimensional bar (cross section: Ω)

the *Poisson* equation

$$\frac{\partial D}{\partial z} = 0 \tag{B.6}$$

and the electrostatic equations

$$I = \dot{Q} = i\omega(\Omega D) \tag{B.7}$$

$$\phi = \int_0^L E\, dz \tag{B.8}$$

With the following mechanical boundary conditions

$$\dot{W}_0 = i\omega W(0) \tag{B.9}$$

$$\dot{W}_L = i\omega W(L) \tag{B.10}$$

$$N_0 = \Omega\sigma(0) \tag{B.11}$$

$$N_L = \Omega\sigma(L) \tag{B.12}$$

Upon differentiating (B.3) with respect to the spatial coordinate z, one gets the expression

$$\frac{\partial \sigma}{\partial z} = c\frac{\partial^2 W}{\partial z^2} - h\frac{\partial D}{\partial z} \tag{B.13}$$

Replacing (B.13) in (B.5) and taking into account equation (B.6), one gets the equation of vibration in extension of the bar

$$\rho\omega^2 W + c\frac{\partial^2 W}{\partial z^2} = 0 \tag{B.14}$$

of which the solution can be written

$$W = \zeta_1 \cos(\lambda z) + \zeta_2 \sin(\lambda z) \tag{B.15}$$

with

$$\lambda^2 = \frac{\rho\omega^2}{c} \tag{B.16}$$

The constants ζ_1 and ζ_2 can be determined from the boundary conditions

$$\zeta_1 = \frac{\dot{W}_0}{i\omega} \tag{B.17}$$

$$\zeta_2 = \frac{\dot{W}_L - \dot{W}_0 \cos(\lambda L)}{i\omega \sin(\lambda L)} \tag{B.18}$$

Developing (B.3) and (B.4) with (B.15), one gets

$$\sigma = -\frac{c\lambda}{i\omega \sin(\lambda L)} \left(\dot{W}_0 \cos\left(\lambda(L-z)\right) - \dot{W}_L \cos(\lambda z) \right) - hD \tag{B.19}$$

$$E = \frac{h}{i\omega} \left(\dot{W}_0 \cos\left(\lambda(L-z)\right) - \dot{W}_L \cos(\lambda z) \right) + \beta D \tag{B.20}$$

To write the influence of the electrical boundary conditions on the natural frequencies, a method based on the electromechanical impedance will be used. The equations relating explicitely all the boundary conditions can be found developing (B.11), (B.12) and (B.8). We obtain

$$\begin{Bmatrix} N_0 \\ N_L \\ \phi \end{Bmatrix} = Z(\omega) \begin{Bmatrix} \dot{W}_0 \\ \dot{W}_L \\ I \end{Bmatrix} \tag{B.21}$$

Where Z is the electromechanical impedance matrix

$$Z(\omega) = \begin{bmatrix} & Z^*(\omega) & & -\frac{h}{i\omega} \\ & & & -\frac{h}{i\omega} \\ \frac{h}{i\omega} & -\frac{h}{i\omega} & & \frac{1}{i\omega C} \end{bmatrix} \tag{B.22}$$

where $C = \frac{\Omega}{L\beta}$ is the electrical capacitance under constant strain and Z^*, the mechanical impedance matrix, given by

$$Z^*(\omega) = \frac{\Omega c\lambda}{i\omega} \begin{bmatrix} -\tan(\lambda L)^{-1} & \sin(\lambda L)^{-1} \\ -\sin(\lambda L)^{-1} & \tan(\lambda L)^{-1} \end{bmatrix} \tag{B.23}$$

Z depends only of the vibration frequency (pulsation ω). The non-triviality condition for equation (B.21) under particular boundary conditions will result in an eigenvalue equation for the frequency.

In the particular case of a *free-free* bar ($N_0 = N_L = 0$), the characteristic equation becomes

$$\left\{ \begin{array}{c} 0 \\ 0 \\ \phi \end{array} \right\} = Z(\omega) \left\{ \begin{array}{c} * \\ * \\ I \end{array} \right\} \tag{B.24}$$

resonance (f_r)	$\phi = 0$ (closed circuit)	$\rightarrow$	$det(Z) = 0$
antiresonance (f_a)	$I = 0$ (open circuit)	$\rightarrow$	$det(Z^*) = 0$

If the impedance matrix Z is written

$$Z(\omega) = \left[\begin{array}{ccc} -\alpha & \beta & -\gamma \\ -\beta & \alpha & -\gamma \\ \gamma & -\gamma & \delta \end{array} \right] \tag{B.25}$$

Antiresonance and resonance conditions are given by

$$det(Z^*) = (\alpha - \beta)(\alpha + \beta) = 0 \tag{B.26}$$

$$det(Z) = (\alpha - \beta)(2\gamma^2 - \delta(\alpha + \beta)) = 0 \tag{B.27}$$

- $\alpha - \beta = 0 \Leftrightarrow \cos(\lambda L) = 1 \Leftrightarrow \lambda L = 2n\pi$
  These conditions on λ results in the frequencies

  $$f_a^{2n} = f_r^{2n} = n\sqrt{\frac{c}{\rho L^2}} \tag{B.28}$$

  It can be shown that this condition is equivalent to impose simultaneously $\phi = 0$ and $I = 0$. The displacement is of the form $W_{ar}^{2n} = W\cos(2n\pi z/L)$; The speed of the extemities are equal in amplitude and phase.

- $\alpha + \beta = 0 \Leftrightarrow \cos(\lambda L) = -1 \Leftrightarrow \lambda L = (2n+1)\pi$.
  These conditions on λ results in the antiresonance frequencies

  $$f_a^{2n+1} = \frac{2n+1}{2}\sqrt{\frac{c}{\rho L^2}} \tag{B.29}$$

  The speed of the extemities are equal in amplitude and in opposition of phase.

- $2\gamma^2 - \delta(\alpha + \beta) = 0$, which results in

  $$k^2 - \frac{\lambda L}{2}\text{cotan}\left(\frac{\lambda L}{2}\right) = 0 \tag{B.30}$$

  with the coupling factor $k^2 = \frac{h^2}{\beta c}$ (See e.g. IEEE std; Rogacheva, 1999).

this condition gives the resonance frequencies. If we assume that the piezoelectric effect brings only small changes to the natural frequencies, we can use a perturbation method, allowing us to write $\lambda L = (2n+1)\pi + \epsilon$; upon developing (B.30) to the first order, we find

$$\epsilon \approx -\frac{4k^2}{(2n+1)\pi} \tag{B.31}$$

and the frequencies

$$f_r^{2n+1} = \frac{2n+1}{2}\left(1 - \frac{4k^2}{[(2n+1)\pi]^2}\right)\sqrt{\frac{c}{\rho L^2}} \tag{B.32}$$

In summary

$$f_a^{2n} = f_r^{2n} = n\sqrt{\frac{c}{\rho L^2}} \tag{B.33}$$

$$f_a^{2n+1} = \frac{2n+1}{2}\sqrt{\frac{c}{\rho L^2}} \tag{B.34}$$

$$f_r^{2n+1} = \frac{2n+1}{2}\left(1 - \frac{4k^2}{[(2n+1)\pi]^2}\right)\sqrt{\frac{c}{\rho L^2}} \tag{B.35}$$

Which denotes the influence of the electromechanical coupling induced by the piezoelectricity. Comparing equations (B.33) to (B.35), we see that the ratio between the resonance and the antiresonance frequencies depends only on the coupling factor k^2. This constitutes a practical way of determining k^2 experimentally.

Appendix C

Some data files

C.1 Example of a dynamic analysis using shell elements: Influence of the electromechanical coupling on the natural frequencies

The *Samcef* data file (input for preprocessor *BACON*) used to generate the finite element model of example in §5.1.1 is listed below.

```
! abbreviations
!===============
abre '/h' '2.5e-4'   ! thickness
abre '/Lo' '1.'      ! length
abre '/La' '0.5'     ! width
abre '/NEl' '10'     ! total number of electrodes
abre '/Ncov' '3'     ! number of grounded electrodes
!
! topology
!==========
! 1. nodes
!
.noe i 1
     i 1 x (/La:/NEl) r /NEl
     i (/NEl+1) y (/Lo:/NEl) q /NEl a (/NEl+1)
!
! 2. elements
!
.mai i 1 n 1 2 (/Nel+3) (/Nel+2) at 1
     i 1 m 1 r (/NEl-1)
     i /NEl m (/NEl+1) q (/Ncov-1) a /NEl
     i (/NEl*/Ncov+1) n ((/NEl+1)*/Ncov+1) ((/NEl+1)*/Ncov+2) $
          ((/NEl+1)*/Ncov+/NEl+3) ((/NEl+1)*/Ncov+/NEl+2) at 2
```

```
     i 1 m 1 r (/NEl-1)
     i /NEl m (/NEl+1) q (/NEl-/Ncov-1) a /NEl
.sel groupe 1 maille attr 1
     groupe 1 maille attr 2
!
! 3. electrical nodes
!
.noe i 1001 z .0001
     i 1002 z .0002
!
! electrodes
!
.ael attr 1 en 1001
     attr 2 en 1002
!
! mechanical boundary conditions
!================================
!
.fix i 1        j ((/NEl+1)*(/NEl)+1) k (/NEl+1) c 1 2 3 6
     i (/NEl+1) j ((/NEl+1)*(/NEl+1)) k (/NEl+1) c 1 2 3 6
!
! electrical boundary conditions
!================================
!
.fix i 1002 c 1
!
! Physical properties
!====================
! 1. materials definition
!
.mat i 1 YT 0.65e11 G 0.25e11      $   ! piezo
         NT 0.3 M 7800 a 0 0 0     $
         PZEE (8.854e-12*2600)     $   !   * permittivity
         PZUE 190e-12  190e-12         !   * coupling (d31, d32)
     i 2 YT 2.1e11  G 0.8e11       $   ! steel
         NT 0.3 M 7800 a 0 0 0
     I 3 YT 1.00e00 G 1.00e00      $   ! none
         NT 0.3 M 0000 a 0 0 0
!
! 2. laminate
!
.pli mat 1 t (/h) an (0)      pli 1
     mat 2 t (2*/h) an (0)    pli 2
     mat 3 t (/h) an (0)      pli 3
.lam lam 1 pli  1 2 3
.eta gr 1 lam 1 maille 1 dir 1 2 angle (0)
```

```
gen
!
! resolution parameters
!======================
!
.hyp mindlin
.sam nop5 -1 nop6 -1 nalg 4 nval 10
```

C.2 Cantilever piezoelectric plate

Four files are generated from the finite element modal analysis. lame.inp and lame.out contain the modal electric charge, respectivey for the piezoactuator and the piezosensor. lame.mui and lame.wi contain the modal masses and the eigenfrequecies. lame.fth comes from a static analysis and contains the static response of the piezosensor for a unit voltage applied to the piezoactuator.

The *Matlab* commands listed below generate the state space model corresponding to the input/output system defined above and plot the corresponding frequency response function shown on Fig.5.4. This state space model can be used with all the tools provided with *Matlab-Simulink* and the various toolboxes available.

```
clear all;
Name='lame'
kk=1e-2;%modal damping

%dynamic properties actuator - sensor
in=readmat([Name '.inp']);
out=readmat([Name '.out']);
mui=readmat([Name '.mui']);
wi=readmat([Name '.wi']);

% static response sensor/actuator
fth=readmat([Name '.fth']);

% extraction of the state space system
[ap,bp,cp,dp]=sys(mui,wi,in,out,fth,kk);

% plot of the transfer function
F=logspace(1,3,1000)/2/pi;
[Gp,Pp,Fp]=ptft(ap,bp,cp,dp,1,F);
```

Appendix D

Matlab toolbox

This appendix contains a succint description of the Matlab scripts (organized as a toolbox) used to generate the various examples of Chap.5.

D.1 From finite element to state space

```
* sys.m

 function [a1,b1,c1,d1]=sys(mui,wi,in,out,fth,kk);
   build the system piezo-piezo with a modal damping of kk using
   mass matrix: mui
   frequencies: wi
   input matrix: in
   output matrix: out
   static response: fth
```

D.2 Visualization tools

```
* ptft.m

 function [G,P,F]=ptft(a1,b1,c1,d1,IU,FF);
   plots the transfer functions of the system defined by the state
   space matrices a1, b1, c1, d1 for the input specified by IU and using
   the frequency vector FF
   outputs the  corresponding gain, phase and frequency vectors

* plotmesh.m

 function [MX,MY,MZ,CZ]=plotmesh(elt,nod,C);
  plot the mesh defined by elt (containing the number, type and the list of
```

```
  nodes for each element) and nod (node coordinates vector) and C
  defining the coloration
```

D.3 Other tools

```
* readmat.m

 function [V]=readmat(Name);
   reads the files generated by the finite element analysis

* syst_pr.m

 function [a1,b1,c1,d1]=syst_pr(out,mui,wi,phi,nco,cha,pfth,nele,kk);
   builds the system pressure-pressure (direction (3)) with a modal
     damping of kk using
   modal mass matrix: mui
   frequencies: wi
   input matrices: cha, nco
   output matrix: out
   static response: pfth

* vol_vel.m

 function vvol=vol_vel(elt,nod,phi,noun,nco,nele);
   compute the volume velocity in the direction (3) from the
   topology (elt,nod), the modal shape (phi,      noun, nco)
                                       amplitude       dof nr
                                                 node
   assuming the (nele) electrical dof are at the end !
```

Bibliography

Agarwal, B. D. & Broutman, L. J., 1990, *Analysis and Performance of Fiber Composites*, John Wiley, 2nd edn.

Allik, H. & Hughes, T. J. R., 1970, 'Finite element method for piezoelectric vibration', *International Journal for Numerical Methods in Engineering*, 2:151–157.

Anderson, E. H., Moore, D. M., Fanson, J. L. & Ealey, M. A., 1990, 'Development of an active member using piezoelectric and electrostrictive actuation for control of precision structures', AIAA-90-1085-CP.

Batoz, J.-L. & Dhatt, G., 1990, *Modélisation des structures par éléments finis, Volume 2: poutres et plaques*, Hermès, Paris, France.

Benjeddou, A., Trindade, M. A. & Ohayon, R., 1997, 'A unified beam finite element model for extension and shear piezoelectric actuation mechanisms', *Journal of Intelligent Material Systems and Structures*, 8.

Benjeddou, A., Trindade, M. A. & Ohayon, R., 1998, 'A new shear actuated smart structure beam element', AIAA 98-1922.

Brissaud, M., 1986, *Caractérisation Tensorielle et Modélisation des Céramiques Piézoélectriques Utilisées en Imagerie Ultrasonore*, Ph.D. thesis, INSA-Lyon and Université Claude Bernard - Lyon I, Lyon, France.

Burke, S. E. & Hubbard Jr, J. E., 1987, 'Active vibration control of a simply supported beam using a spatially distributed actuator', *IEEE Control Systems Magazine*, pp. 25–30.

Cady, W. G., 1946, *Piezoelectricity; an Introduction to the Theory and Applications of Electromechanical Phenomena in Crystals*, Mc Graw-Hill, New York, London.

Callahan, J. & Baruh, H., 1996, 'Active control of flexible structures by use of segmented piezoelectric elements', *Journal of Guidance, Control and Dynamics*, 19(4):808–815.

Carlson, J. D., Catanzarite, D. M. & St Clair, K. A., 1995, 'Commercial magneto-rheological fluids devices', 5th International Conference on Electro-Rheological , Magneto-Rheological Suspensions and Associated Technology, Sheffield.

Carlson, J. D. & Sproston, J. L., 2000, 'Controllable fluids in 2000 - status of ER and MR fluid technology', 7th International Conference on New Actuators, Bremen, Germany.

Chattopadhyay, A., Li, J. & Haozhong, G., 1999, 'Coupled thermo-piezoelectric-mechanical model for smart composite laminate', *AIAA Journal*, 37(12).

Chen, S.-H., Wang, Z.-D. & Liu, X.-H., 1997, 'Active vibration control and suppression for intelligent structures', *Journal of Sound and Vibration*, 200(2):167–177.

Clark, A. E., 1980, 'Magnetostrictive rare earth-Fe_2 compounds', in *Ferromagnetic Materials* (Wolfhart, E. P., editor), vol. 1, chap. 7, pp. 531–589, North-Holland, Amsterdam.

Crawley, E. F. & Anderson, E. H., 1989, 'Detailed models of piezoceramic actuation of beams', AIAA 89-1388-CP.

Crawley, E. F. & de Luis, J., 1987, 'Use of piezoelectric actuators as elements of intelligent structures', *AIAA Journal*, 25(10):1373–1385.

Crawley, E. F. & Lazarus, K. B., 1991, 'Induced strain actuation of isotropic and anisotropic plates', *AIAA Journal*, 29(6):944–951.

Dimitriadis, E. K., Fuller, C. R. & Rogers, C. A., 1991, 'Piezoelectric actuators for distributed vibration excitation of thin plates', *Transactions of the ASME, Journal of Vibrations and Acoustics*, 113:100–107.

Eer Nisse, E. P., 1967, 'Variational method for electroelastic vibration analysis', *IEEE Transactions On Sonics And Ultrasonics*, 14(4):153–160.

Forward, R., 1981, 'Electronic damping of orthogonal bending modes in a cylindrical mast experiment', *AIAA Journal of Spacecraft*, 18(1):11–17.

Gardonio, P., Lee, Y., Elliott, S. & Debost, S., 1999, 'Active control of sound transmission through a panel with a matched PVDF sensor and actuator pair', Active 99, Fort Lauderdale, Florida, USA.

Ha, S. K., Keilers, C. & Chang, F. K., 1992, 'Finite element analysis of composite structures containing distributed piezoceramic sensors and actuators', *AIAA Journal*, 30(3):772–780.

Heyliger, P., Pei, K. C. & Saravanos, D., 1996, 'Layerwise mechanics and finite element model for laminated piezoelectric shells', *AIAA Journal*, 34(11):2353–2360.

Hong, C.-H. & Chopra, I., 1999, 'Modeling and validation of induced strain actuation of composite coupled plates', *AIAA Journal*, 37(3).

Hughes, T. J. R., 1987, *The Finite Element Method*, Prentice-Hall International Editions.

Hwang, W. S. & Park, H. C., 1993, 'Finite element modeling of piezoelectric sensors and actuators', *AIAA Journal*, 31(5):930–937.

IEEE std, 1988, 'IEEE standard on piezoelectricity', ANSI/IEEE Std 176-1987.

Jetteur, P., 1991, 'Validation des éléments 28 et 29', Tech. Rep. 39, Samtech s.a., Liège, Belgium.

Köppe, H., Gabbert, U. & Tzou, H. S., 1998, 'On three-dimensional layered shell elements for the simulation of adaptive structures', in *Proceedings of the Euromech 373 Colloquium: Modeling and Control of Adaptive Mechanical Structures - Preprint*, ADAMES, University of Magdeburg.

Lardeur, P., 1990, *Développement et Evaluation de deux Nouveaux Eléments Finis de Plaques et Coques Composites avec Influence du Cisaillement Transversal*, Ph.D. thesis, Université de Compiègne, Compiègne, France.

Lee, C.-K., 1990, 'Theory of laminated piezoelectric plates for the design of distributed sensors/actuators. Part I: Governing equations and reciprocal relationships', *Journal of the Acoustical Society of America*, 87(3):1144–1158.

Lee, C.-K., Chiang, W.-W. & O'Sullivan, T. C., 1989, 'Piezoelectric modal sensors and actuators achieving critical active damping on a cantilever plate', AIAA 89-1390-CP.

Lee, C.-K., Chiang, W.-W. & O'Sullivan, T. C., 1991, 'Piezoelectric modal sensor/actuator pairs for critical active damping vibration control', *Journal of Acoustical Society of America*, 90(1):374–384.

Lee, C.-K. & Moon, F. C., 1990, 'Modal sensors/actuators', *Journal of Applied Mechanics*, 57:434–441.

Lee, H.-J. & Saravanos, D. A., 1996, 'Coupled layerwise analysis of thermopiezoelectric composite beams', *AIAA Journal*, 34(6):1231–1237.

Lerch, R., 1990, 'Simulation of piezoelectric devices by two- and three-dimensional finite elements', *IEEE Transactions on Ultrasonics, Ferroelectrics, and Frequency Control*, 37(3):233–247.

Liang, C., 1990, *The Constitutive Modeling of Shape Memory Alloys*, Ph.D. thesis, Virginia Polytechnic Institute and State University, Blacksburg, Virginia.

Loix, N., 1998, *Amortissement Actif de Structures Flexibles*, Ph.D. thesis, Université Libre de Bruxelles, Brussels, Belgium.

Loix, N., Piefort, V. & Preumont, A., 1998, 'Modeling aspects of active structures with collocated piezoelectric actuators and sensors', *Benelux Quarterly Journal on Automatic Control (Journal a)*, 39(1).

Loix, N. & Preumont, A., 1995, 'Remarks on the modelling of active structures with colocated piezoelectric actuators and sensors', in *ASME Design Engineering Technical Conference: Vibration Control, Analysis, and Identification*, vol. 3, pp. 335–339, Boston.

Miller, S. E., Abramovich, H. & Oshman, Y., 1997, 'Selective modal transducers for anisotropic rectangular plates: Experimental validation', *AIAA Journal*, 35(10):1621–1629.

Miller, S. E., Oshman, Y. & Abramovich, H., 1996a, 'Modal control of piezolaminated anisotropic rectangular plates - Part I: Modal transducer theory', *AIAA Journal*, 34(9):1868–1875.

Miller, S. E., Oshman, Y. & Abramovich, H., 1996b, 'Modal control of piezolaminated anisotropic rectangular plates - Part II: Control theory', *AIAA Journal*, 34(9):1876–1884.

Miller, S. E., Oshman, Y. & Abramovich, H., 1998, 'Modal transducers for piezolaminated anisotropic zero-gaussian curvature shell systems', AIAA 98-1953.

Mindlin, R. D., 1974, 'Equations of high frequency vibrations of thermopiezoelectric crystal plates', *International Journal of Solids Structure*, 10:625–637.

Moetakef, M. A., Joshi, S. P. & Lawrence, K. L., 1996, 'Elastic wave generation by piezoceramic patches', *AIAA Journal*, 34(10):2110–2117.

Moetakef, M. A., Lawrence, K. L., Joshi, S. P. & Shiakolas, P. S., 1995, 'Closed-form expressions for higher order electroelastic tetrahedral elements', *AIAA Journal*, 33(1):136–142.

Moffett, M. B., Clark, A. E., Wun Fogle, M., Linberg, J., Teter, J. P. & Mc Laughlin, E. A., 1991, 'Characterization of Terfenol-D for magnetostrictive transducers', *Journal of the Acoustical Society of America*, 89(3):1448–1455.

Moskalik, A. J. & Brei, D., 1997, 'Deflection-voltage model and experimental results for polymeric piezoelectric c-block actuators', *AIAA Journal*, 35(9):1556–1558.

Nye, J. F., 1957, *Physical Properties of Crystals: Their Representation by Tensors and Matrices*, Clarendon Press, Oxford.

Park, C. & Chopra, I., 1996, 'Modeling piezoceramic actuation of beams in torsion', *AIAA Journal*, 34(12):2582–2589.

Perkins, J., editor, 1975, *Shape Memory Effects in Alloys*, Plenum Press, New-York.

Piefort, V., 1991, *Applications des Alliages à Mémoire de Forme*, Master's thesis, Université Libre de Bruxelles, Brussels, Belgium.

Piefort, V., 1997, 'Finite element modeling of piezoelectric structures - Final report', ULB - Active Structures Laboratory; Convention 95/2792 - Région Wallonne.

Piefort, V., 2000, 'Modeling of the piezoelectric coupling in active structures - Final report', ULB - Active Structures Laboratory; Convention 9713549 - Région Wallonne.

Piefort, V. & Henrioulle, K., 2000, 'Modelling of smart structures with colocated piezoelectric Actuator/Sensor pairs: Influence of the in-plane components', 5th International Conference on Computational Structures Technology, Leuven, Belgium.

Piefort, V., Loix, N. & Preumont, A., 1998, 'Modeling of piezolaminated composite shells for vibration control', European Conference on Spacecraft Structures, Materials and Mechanical Testing, Braunschweig.

Piefort, V. & Preumont, A., 1998, 'Finite element modeling of piezolaminated composite shells', Samtech User's Conference, Liège, Belgium.

Piefort, V. & Preumont, A., 2000a, 'Finite element modelling of smart piezoelectric shell structures', 5th National Congress on Theoretical and Applied Mechanics, Louvain-La-Neuve, Belgium.

Piefort, V. & Preumont, A., 2000b, 'Modeling of active shell structures with embedded piezoelectric actuators and sensors', Materials Week, International Congress on Advanced Materials, their Processes and Applications, München, Germany.

Piefort, V. & Preumont, A., 2000c, 'Modeling of smart piezoelectric structures with finite elements', ISMA25, 25th International Conference on Noise and Vibration Engineering, Leuven, Belgium.

Piefort, V. & Preumont, A., 2001, 'Finite element modeling of piezoelectric structures', Samtech User's Conference, Paris, France.

Piezotech Documentation, 1997, 'Films piézo- et pyro-électriques', Document DT-96/a.

Pitoiset, X., 2001, *Méthodes Spectrales pour une Analyse en Fatigue des Structures Métalliques sous Chargements Aléatoires Multiaxiaux*, Ph.D. thesis, Université Libre de Bruxelles, Brussels, Belgium.

Pitoiset, X. & Preumont, A., 2000, 'Spectral methods for multiaxial random fatigue analysis of metallic structures', *International Journal of Fatigue*, 22(7):541–550.

Pitoiset, X., Preumont, A. & Kernilis, A., 1998, 'Tools for a multiaxial fatigue analysis of structures submitted to random vibration', European Conference on Spacecraft Structures, Materials and Mechanical Testing, Braunschweig.

Preumont, A., 1997, *Vibration Control of Active Structures - An Introduction*, Kluwer Academic Publishers, Dordrecht, The Netherlands.

Preumont, A., François, A. & Dubru, S., 1999, 'Piezoelectric array sensing for real-time, broadband sound radiation measurement', *Journal of Vibration and Acoustics*, 121.

Rao, S. S. & Sunar, M., 1993, 'Analysis of distributed thermopiezoelectric sensors and actuators in advanced intelligent structures', *AIAA Journal*, 31(7):1280–1286.

Reddy, J. N., 1984, *Energy and Variational Methods in Applied Mechanics*, John Wiley & sons.

Rex, J. & Elliott, S. J., 1992, 'The QWSIS - a new sensor for structural radiation control', MOVIC-1, Yokohama.

Rogacheva, N. N., 1999, 'Analysis and optimization of energy conversion efficiency for piezoelectric transducers', in *Smart Structures - Requirements and Potential Applications in Mechanical and Civil Engineering* (Holnicki-Szulc, J. & Rodellar, J., editors), pp. 295–302, NATO Sciences Series, Kluwer Academic Press, Dordrecht, The Netherlands.

Ryou, J.-K., Park, K.-Y. & Kim, S.-J., 1998, 'Electrode pattern design of piezoelectric sensors and actuators using genetic algorithms', *AIAA Journal*, 36(2):227–233.

Samanta, B., Ray, M. C. & Bhattacharyya, R., 1996, 'Finite element model for active control of intelligent structures', *AIAA Journal*, 34(9):1885–1893.

SAMTECH, 2000, *SAMCEF User's Manual V8.1, Vol.3: Elements*.

Saravanos, D. A., 1997, 'Mixed laminate theory and finite element for smart piezoelectric shell structure', *AIAA Journal*, 35(8):1327–1333.

Saravanos, D. A., 2000, 'Passively damped laminated piezoelectric shell structures with integrated electric networks', *AIAA Journal*, 38(7).

Suleman, A. & Gonçalvès, M. A., 1995, 'Optimization issues in application of piezoelectric actuators in panel flutter control', IDMEC-Instituto Superior Tecnico, Departamento de Engenharia Mecanica, 1096 Codex, Portugal.

Suleman, A. & Venkayya, V. B., 1995a, 'Flutter control of an adaptive laminated composite panel with piezoelectric layers', IDMEC-Instituto Superior Tecnico, Departamento de Engenharia Mecanica, 1096 Codex, Portugal.

Suleman, A. & Venkayya, V. B., 1995b, 'A simple finite element formulation for a laminated composite plate with piezoelectric layers', *Journal of Intelligent Material Systems and Structures*, 6:776–782.

Sunar, M. & Rao, S. S., 1996, 'Distributed modeling and actuator location for piezoelectric control systems', *AIAA Journal*, 34(10):2209–2211.

Sunar, M. & Rao, S. S., 1997, 'Thermopiezoelectric control design and actuator placement', *AIAA Journal*, 35(3):534–539.

Tiersten, H. F., 1967, 'Hamilton's principle for linear piezoelectric media', in *Proceedings of the IEEE*, pp. 1523–1524.

Tzou, H. S. & Tseng, C. I., 1990, 'Distributed piezoelectric sensor/actuator design for dynamic measurement/control of distributed parameter systems: a piezoelectric finite element approach', *Journal of Sound and Vibration*, 138(1):17–34.

Tzou, H. S. & Tseng, C. I., 1991, 'Distributed modal identification and vibration control of continua: Piezoelectric finite element formulation and analysis', *Transactions of the ASME, Journal of Dynamic Systems, Measurement and Control*, 113:500–505.

Tzou, H. S. & Ye, R., 1996, 'Analysis of piezoelastic structures with laminated piezoelectric triangle shell elements', *AIAA Journal*, 34(1):110–115.

Uchino, K., 2000, *Ferroelectric Devices*, Marcel Dekker inc., New-York.

van Randeraat, J. & Setterington, R., editors, 1974, *Piezoelectric Ceramics*, Mullard Ltd, London, UK, 2nd edn.

Zhou, X., Chattopadhyay, A. & Haozhong, G., 2000, 'Dynamic responses of smart composites using a coupled thermo-piezoelectric-mechanical model', *AIAA Journal*, 38(10).

Zienkiewicz, O. C., 1971, *The Finite Element Method in Engineering Science*, Mc Graw-Hill, Maidenhead.